Bangor University

DOCTOR OF PHILOSOPHY

Spatially resolved characterisation of CdTe photovoltaic solar cells

Brooks, William

Award date:
2012

Awarding institution:
Bangor University

Spatially Resolved Characterisation of CdTe Photovoltaic Solar Cells

A thesis presented in candidature

for the

Degree of

Doctor of Philosophy

in the

School of Electronic Engineering

by

William Brooks

Acknowledgements

I would like to take this opportunity to thank the EPSRC for funding the SUPERGEN PV21 project, from which the funding for my Ph.D originated.

I would also like to thank my supervisor Stuart Irvine for his support and patience throughout the duration of the Ph.D. My sincere thanks also go to all at the Centre for Solar Energy Research (CSER), Glyndwr University, in particular Vincent Barrioz, Dan Lamb and Andy Clayton whose continued technical support and guidance have proved invaluable.

Thanks also to Martin Taylor for welcoming me into the School of Electronic Engineering at Bangor University, and to John Cambridge and Yanhua Hong for their expert assistance in the operation of the SPM.

Further thanks go to the SUPERGEN project collaborators, many of whom I have worked closely with: Ken Durose and Jon Major at Liverpool University, Jeremy Ball at London Southbank University, Lefteris Danos at Southampton University and Ian Forbes at Northumbria University.

Thanks also to Ffion and all my family and friends who have been so supportive throughout this Ph.D, and especially through a particular tumultuous time in 2009 where I must also thank a lot of people to whom I literally owe my life: those from the RAF Valley Search and Rescue, Ysbyty Gwynedd and Liverpool Broadgreen hospital and many others. Thank you!!

Abstract

Spatially resolved measurements of CdTe thin film photovoltaic solar cells were performed using both laser beam induced current (LBIC) and scanning probe microscopy (SPM) techniques.

The triple wavelength LBIC system was used to assess the thickness uniformity of $Cd_{1-x}Zn_xS$ window layers incorporated into CdTe solar cells. A blue laser was used to reveal window layer absorption and transmission characteristics. This was observed to influence photoresponse at longer wavelengths where lateral variations in minority carrier lifetime were leading to variable carrier collection. This was found to be caused by localised regions of ~ 50 nm thin $Cd_{1-x}Zn_xS$ forming a defective depletion region. The moderate to high clustering of pin-holes in both thick and thin regions of $Cd_{1-x}Zn_xS$ and CdTe layers was found to contribute to shunt resistance losses independently of the $Cd_{1-x}Zn_xS$ thickness distribution. Quantum dot (QD) luminescent down shifting layers incorporated into $Cd_{1-x}Zn_xS$/CdTe devices were studied using the LBIC technique where, using a 405 nm excitation wavelength, QD isotropic emission was observed to increase the overall lateral carrier collection area of the cell.

Scanning Kelvin probe microscopy (SKPM) was used to study the Fermi level shift in Arsenic doped CdTe devices where the contact potential difference (CPD) between probe tip and sample surface revealed that increasing As concentrations in CdTe led to a decrease in CPD. This highlighted a downward shift in the CdTe Fermi level and an increase in CdTe work function. Absolute CdTe work function values between 3.88 and 4.09 eV were calculated using a highly oriented pyrolytic graphite reference sample. A localised shift in CPD at grains boundaries with increased As doping was observed. This was proposed to reduce carrier recombination by channelling minority carriers away from the grain boundary.

Conductive atomic force microscopy revealed differences in bulk grain and grain boundary conductivity. The localised CdTe E_f and the barrier formed at the tip/surface interface was observed to determine the measured current.

Contents

List of Figures and Tables

List of Definitions

AFM – Atomic Force Microscopy

AM – Air Mass

AP – Atmospheric Pressure

BSE – Back Scattered Electron

CAFM – Conductive Atomic Force Microscopy

CB – Conduction band

CBD – Chemical Bath Deposition

CCD – Charge Coupled Device

$Cd_{1-x}Zn_xS$ – Cadmium Zinc Sulphide

$CdCl_2$ – Cadmium Chloride

CdS – Cadmium Sulphide

CdTe – Cadmium Telluride

CPD – Contact Potential Difference

CPV – Concentrated Photovoltaics

CSS – Close Spaced Sublimation

CVD – Chemical Vapour Deposition

DI - Deionised

DSSC – Dye Sensitized Solar Cell

EBIC – Electron Beam Induced Current

EBSD – Electron Back Scatter Diffraction

ED - Electrodeposition

EDX – Energy Dispersive X-ray analysis

E_f - Fermi level

E_g – Band Gap

EPSRC – Engineering and Physical Sciences Research Council

EQE – External Quantum Efficiency

eV – Electron Volt

FF – Fill Factor

FTO – Fluorine doped Tin Oxide

GB – Grain Boundary

HCPV – Heliostat Concentrated Photovoltaics

HOMO – Highest Occupied Molecular Orbital

HOPG – Highly Oriented Pyrolytic Graphite

IB – Intermediate Band

I_{sc} – Short Circuit Current

ITO – Indium doped Tin Oxide

I-V – Current - Voltage

J_{sc} – Short Circuit Current Density

LBIC – Laser Beam Induced Current

LDS – Luminescent Down Shifting

LUMO Lowest Unoccupied Molecular Orbital

MFC – Mass Flow Controller

MOCVD – Metal Organic Chemical Vapour Deposition

NREL – National Renewable Energy Laboratories (USA)

NSOM – Near-field Scanning Optical Microscopy

OBIC – Optical Beam Induced Current

OPVC – Organic Photovoltaic Cell

pCAFM – Photo Conductive Atomic Force Microscopy

PECVD – Plasma Enhanced Chemical Vapour Deposition

PL - Photoluminescence

PMMA - Polymethylmethacrylate

PSPD – Position Sensitive Photodetector

PTB - Physikalisch-Technische Bundesanstalt

PTI – Power Technologies Inc.

PV – Photovoltaic

PVD – Physical Vapour Deposition

QD – Quantum Dot

R_{sheet} – Sheet Resistance

SCM – Scanning Capacitance Microscopy

SEM – Scanning Electron Microscope

SIMS – Secondary Ion Mass Spectroscopy

SKPM – Scanning Kelvin Probe Microscopy

SP – Surface Potential

SPM – Scanning Probe Microscopy

SRH – Shockley-Read-Hall

STC – Standard Test Conditions

SUPERGEN – Sustainable Power Generation and Supply

TCO – Transparent Conducting Oxide

TEM – Transmission Electron Microscope

UHV –Ultra High Vacuum

VB – Valance Band

V_{oc} – Open Circuit Voltage

W_p - Watt Peak

XRD – X-ray Diffraction

α – Absorption Coefficient

η – Photovoltaic Conversion Efficiency

Φ – Work Function

1 Introduction

Sustainability is the key to energy generation. This unavoidable realization has been catalysed in the first years of the 21st century by rapidly increasing energy costs as record breaking oil prices impact an array of macroeconomic variables [1]. This impacts our society on many levels as the cheap energy we have come to depend on is no longer so abundant [2]. A variety of approaches are required so that adjustment to this new energy climate can be made. Key to these are the inter-related areas of (a) energy conservation, the net reduction in global energy consumption per capita, (b) energy efficiency, where energy is used sparingly and innovatively and (c) the manufacture and large-scale adoption of renewable energy on the multi-gigawatt level [3, 4].

In order to approach this challenge, government and industry need to collaborate and develop innovative technologies and incentives to place renewable energy centre-stage. This diverse classification includes wind, hydro, geothermal and solar photovoltaic (PV) energy.

The potential for solar PV energy is enormous. Enough light falls on the earth every 40 minutes to satisfy global energy demands for an entire year. Therefore the issues that arise are not in the abundance of this energy source, but in the successful capture and utilization or storage of this energy in a form that can begin to take over from existing energy generation processes, primarily the combustion of fossil fuels.

Technological development and innovation since the industrial revolution have provided a natural progression away from high carbon content fuels. A historical trend can be seen; where the exploitation of coal gave way to crude oil, followed by natural gas and nuclear energy in the second half of the twentieth century. The next step would therefore move us into a virtually carbon-free energy future. The benefits of which are far-reaching and will lie beyond resolving the issues of continuing fossil fuel depletion, and the potentially lethal effects of anthropogenic climate change. An economy based on renewable energy could strengthen global and local economies by creating new jobs [5] in the diverse renewable energy sectors as well as reducing reliance on energy imports from politically unstable regions of the world.

As Turner [4] outlines, PV energy production has the potential to meet substantial energy demands, but if we are to achieve such ambitions PV cell production costs need to be significantly reduced while efficiencies and reliability improve.

1.1 The PV effect – the early days

The term ‘photovoltaic’ is derived from the greek ‘phos’ meaning light, and volt, from the early Italian pioneer in the field of electricity, Alessandro Volta (1745-1827). This describes the process whereby light is converted into electricity, and was first reported by French physicist Edmond Becquerel in 1839, who using an electrolytic cell, noted that a current was generated when the cell was exposed to light [6]. It wasn’t until 1876 when the PV effect was observed in selenium (Se) by William Grylls Adams and Richard Day [7] that its true potential began to be realised, with the eminent German inventor and industrialist Werner von Siemens stating it was “scientifically of the most far-reaching importance”. This statement is as true today as it was in these pioneering years. This technology has the potential to truly revolutionise our energy requirements.

This discovery led on to further Se-based PV research, where in 1883 Charles Fritts built what is considered by many to be the first PV cell. Though operating at only 1-2% conversion efficiency this provided a basis for further work in the early twentieth century, including the discovery of the PV effect in cadmium selenide (CdSe) though it wasn’t until the 1950’s that PV devices began to resemble what we recognise today.

1.2 Development of modern solar cells

The modern homojunction silicon, (Si) solar cell was developed in 1954 by Chapin et al [8]. A 6% conversion efficiency was achieved using arsenic (As) and boron (B) dopants to form a p-n junction in a single crystal Si wafer. This was a huge leap from the Se based solar cells, which operated at only 0.5% conversion efficiency [9]. This improved solar technology found the majority of its applications in space, while it wasn’t until the 1970’s, as the Si feedstock industries matured and the Arab oil embargos of 1973 that the technology became economically attractive for terrestrial applications.

Si still dominates the PV solar market today in a variety of forms, from the bulk crystalline cell developed in the 1950's, to polycrystalline (μc-Si) and hydrogenated amorphous (a-Si:H) thin films developed more recently. The requirement for high feedstock quality and intensive device processing demanded by crystalline Si PV cells places thin film Si technologies in a commercially favourable position. Crystalline Si wafer thicknesses are typically between 180 and 350 μm; these are cut by wire-sawing block-cast single crystal or polycrystalline Si ingots. Conversely, thin films can be produced relatively cheaply using a variety of processes including chemical vapour deposition (CVD) and physical vapour deposition (PVD). These techniques consume < 1% of the feedstock material required for analogous bulk Si materials, so the reduction in device efficiency observed in these materials is more than compensated for, leading to a significantly lower unit cost per W_P.

Now considered a mature technology, Si has been extensively studied and developed. Conversion efficiencies, η now approach theoretical limits, with a maximum cell efficiency of 25 % reported for crystalline Si, this figure increasing to 27.6 % for Si under 92 sun concentration. Crystalline Si module efficiencies of 22.9 % over 778 cm^2 have also been reported [10].

1.3 Solar Irradiance

Figure 1.1 shows (a) the solar spectrum outside the Earth's atmosphere; known as AM0, (b) a black body at a temperature of 5250°C and (c) the solar spectrum as considered for Standard Test Conditions (STC), known as AM1.5. The impact the Earth's atmosphere has on incident sunlight is characterised by air mass (AM), this refers to the optical path length through the atmosphere to the Earth's surface, as illustrated in Figure 1.2. AM accounts for light attenuation caused by scattering, reflection and absorption (NB. atmospheric gas absorption labelled in Figure 1.1). AM0 refers to light unaffected by the Earth's atmosphere, and is used to calibrate and characterise solar irradiance for space applications. AM0 resembles a black body at 5250 °C and has a wavelength integrated value of approximately 1366 W m^{-2}. AM1 refers to light incident on the Earth's surface at the solar zenith, at an angle normal to the surface of the Earth.

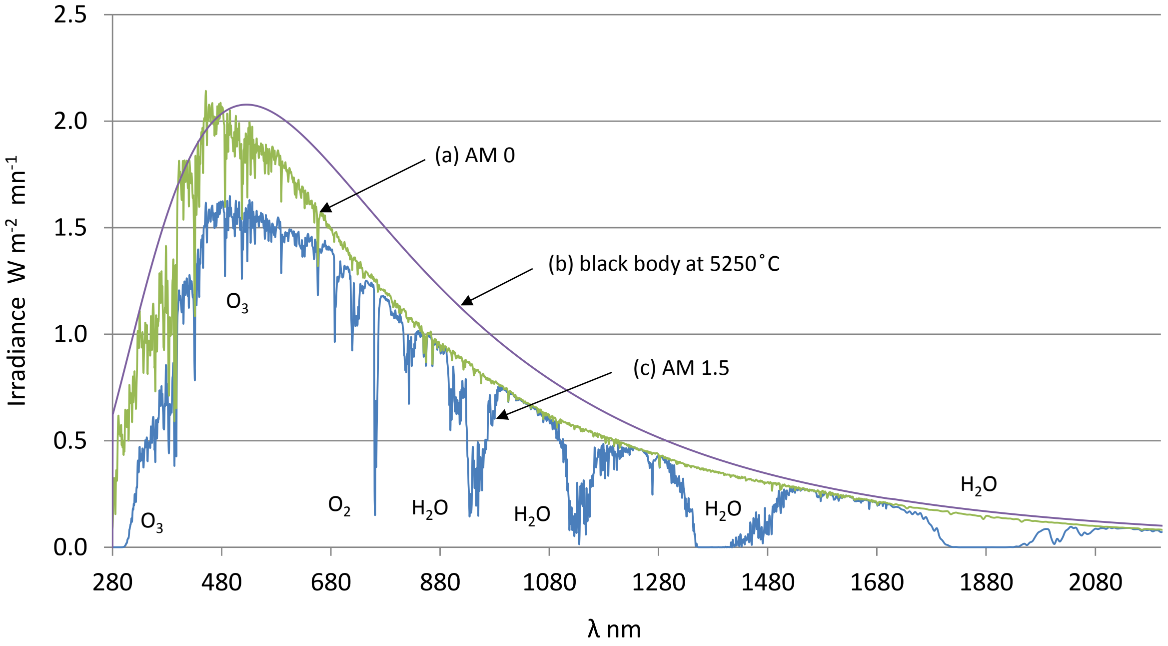

Figure 1.1. Solar irradiance spectrum at sea level and above the Earth's atmosphere

AM1.5 accounts for atmospheric effects on incident light at a tilt angle of 48.2 °; the average latitude of the contiguous USA, the home of AM1.5. Scattering and absorption effects are seen to increase at AM1.5 compared to AM1 due to an increased optical path length, as shown in Figure 1.2. AM1.5 provides an international insolation standard by which PV devices can be calibrated and comparisons made.

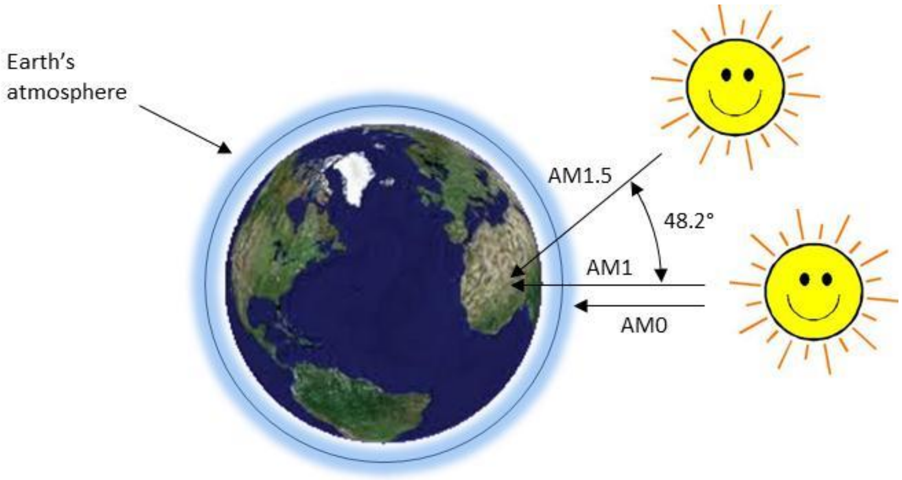

Figure 1.2. Solar irradiance at zenith and AM1.5 tilt angle

1.4 Semiconductors – An Introduction

A semiconductor [11] can be considered as a material whose properties lie between that of a metal and an insulator, where the bandgap, E_g will be larger than a metal but smaller than an insulator. Therefore, under certain conditions a semiconductor will be a conductor and in others it will be an insulator.

Semiconductors can be either (a) intrinsic, where properties like crystal defects create shallow acceptor or donor states and thermal excitation results in conductivity, or (b) extrinsic, where dopants are added to change the properties of a material. Dopants act to increase either the hole or electron charge carrier concentrations. Doping can produce either n-type or p-type extrinsic semiconductors.

If we consider the quantum mechanical concept, the Fermi level, E_f; this refers to the highest occupied energy level at absolute zero. In an n-type semiconductor E_f will increase as donor impurity atoms are introduced, this correlates to an increase in the negative charge carrier concentration in the conduction band, CB. Therefore, the majority carriers in an n-type semiconductor are electrons. The opposite is the case for p-type material, where the introduction of acceptor dopant atoms increases the hole charge carrier concentration in the valance band, VB. This leads to a decrease in E_f. In p-type semiconductors the majority carriers are holes.

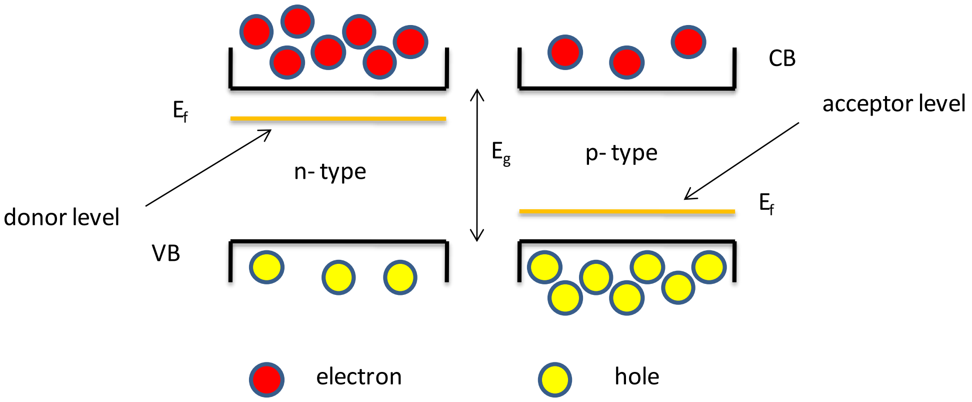

Figure 1.3. Fermi levels of p- and n-type extrinsic semiconductors

Figure 1.3 illustrates the effect that dopants have on charge carrier concentrations. E_f provides a useful means of understanding the interaction of n- and p-type materials when they are brought together to form a rectifying junction; the basis of the charge separation mechanism in thin film PV materials.

1.5 Thin film semiconductors in PV

When n-type and p-type semiconductors are brought together, the respective Fermi levels align, resulting in the bending of the VB and CB’s as shown in Figure 1.4. Carrier diffusion across the interface continues until an equilibrium condition is achieved. This process requires electrons to diffuse across the junction into the p-type material leaving behind fixed ions with positive charge in the n-type material. Similarly, holes diffuse into the n-type material leaving behind fixed ions with negative charge, this diffusion continues until the concentration of the diffusing charge carriers begins to repel any further charge flux.

The equilibrium condition leads to the formation of fixed ions at, or close to the pn interface, giving rise to a space charge, or depletion region as illustrated for a CdTe solar cell in Figure 1.4.

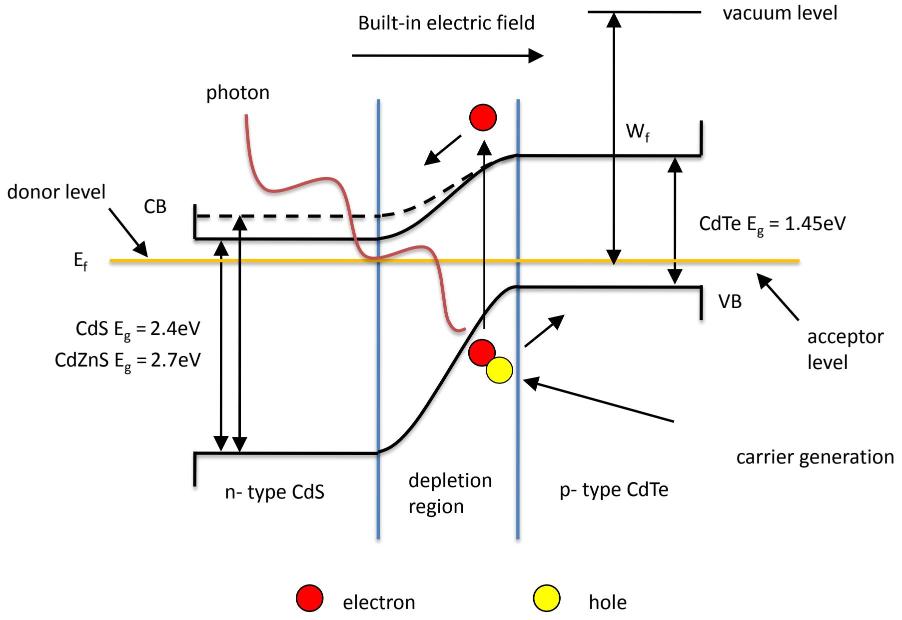

Figure 1.4. Band alignment and charge separation mechanism in CdS/CdTe solar cell

Incident photons on the PV device provide the excitation energy to promote an electron from the VB across the E_g into the CB. Figure 1.4 illustrates that for a CdS/ CdTe cell photons with energy < 2.4 eV and > 1.45 eV will be transmitted through the CdS window layer and be absorbed in the CdTe absorber layer. This corresponds to a wavelength range between 517 and 855 nm. For a PV cell incorporating a $Cd_{1-x}Zn_xS$ window layer, with E_g = 2.7 eV this wavelength range can be increased from 459 to 855 nm, accounting for increased window layer transmission in the blue region of the spectrum.

Figure 1.4 also illustrates the excitation process at the core of a solar cells operation. When a photon with energy, $E \geq E_g$ is absorbed, the promoted electron and newly formed hole rely on the electric field to become spatially separated. This carrier separation mechanism refers to carrier drift and is in contrast to carrier diffusion, where charges are separated by random thermal motion. Carrier drift refers to charge separation driven by an electric field.

Figure 1.5 below illustrates the position of the absorption edges of these materials, highlighting how they correspond favourably to the solar spectrum. These materials absorb in the visible and near – IR regions of the solar spectrum where a large proportion of solar irradiance is concentrated. For a CdS/ CdTe cell, the absorption edges allow for ~ 43 % of the incident solar spectrum to be absorbed, whereas the wider bandgap $Cd_{1-x}Zn_xS$/ CdTe cell increases this figure to ~ 52 % with optical gains made in higher energy blue region of the spectrum.

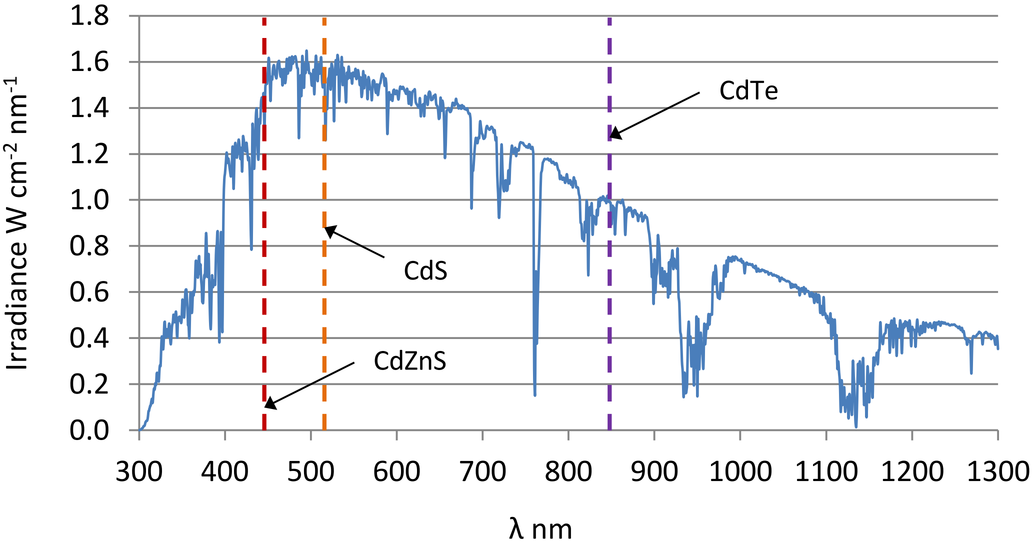

Figure 1.5. CdZnS, CdS and CdTe band edges against visible / near IR solar spectrum

Further to optical and absorption considerations, single pn junction solar cells have further constraints on their performance. These electrical limitations have been detailed by Shockley and Queisser [12] and include thermal losses related to blackbody emission and recombination mechanisms whereby carriers recombine prior to successful charge separation. Considering (a) spectral losses (b) thermal losses and (c) recombination it was calculated that the maximum efficiency for a single pn junction solar cell was ~ 30 % (based on E_g = 1.1 eV).

1.6 *Thin film PV devices*

Thin film PV devices differ from traditional wafer, or bulk Si devices by using individual layers to form either single or multi junction cells. Typical examples of single junction thin film solar cells include, hydrogenated amorphous Si (a-Si:H), microcrystalline Si (μc-Si), copper indium gallium diselenide ($CuInGaSe_2$) and cadmium telluride (CdTe). Multi-junction cells integrate multiple thin films to form to number of pn junctions in series to capture a larger section of the solar spectrum. Indium gallium phosphide ((In,Ga)P), (indium) gallium arsenide ((In,Ga)As) and germanium, (Ge) are common materials found in triple junction solar cells providing good optical absorption over a broad spectral range and relatively good separation of generated electron hole pairs.

Thin film PV cells are typically found in one of two configurations: substrate or superstrate. CdTe cells are commonly produced in superstrate configuration, whereas $CuInGaSe_2$ cells are produced in substrate configuration. Figure 1.6 shows a CdTe cell, in superstrate configuration, where the glass substrate performs a number of functions: 1. providing the supporting structure for the cell; 2. as the window for the incident light to pass through and 3. a component of the cells encapsulation.

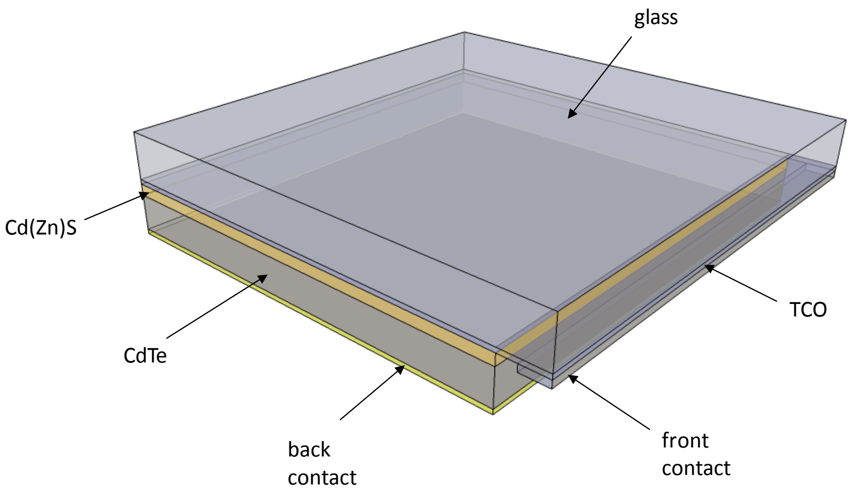

Figure 1.6. Cd(Zn)S/ CdTe solar cell in superstrate configuration

In a superstrate solar cell the transparent conducting oxide (TCO) is deposited first, followed by the window layer and absorber material; these are shown as $Cd_{1-x}Zn_xS$ and CdTe respectively in Figure 1.6. A high work function, Φ metal is deposited on the CdTe back surface to form an ohmic back contact and complete the cell structure. In substrate configuration solar cells, the sequence of deposited layers is in reverse to the superstrate cells described above. A glass, steel or plastic, molybdenum, Mo coated substrate is typically used; this conductive layer acts as the device back contact. First the $CuInGaSe_2$ absorber material is deposited, followed by a CdS window layer and TCO.

$CuInGaSe_2$ solar cells are composed of a solid solution of $CuInSe_2$ and $CuGaSe_2$. The E_g of this highly absorbing semiconductor can be tuned from 1.0 eV for $CuInSe_2$ to 1.7 eV for $CuGaSe_2$ depending on the stoichiometry of the compounds. The electrically benign nature of the structural defects native in this polycrystalline material result in a favourable comparison with its single crystal counterpart, where impurities and crystalline defects have a more detrimental effect compared with those found in other polycrystalline semiconductors [13]. Maximum efficiencies of 20.3 % have been achieved for this absorber material [14]. $CuInGaSe_2$ has been grown in both superstrate as is typical for CdTe and more successfully in substrate configuration as shown in Figure 1.7.

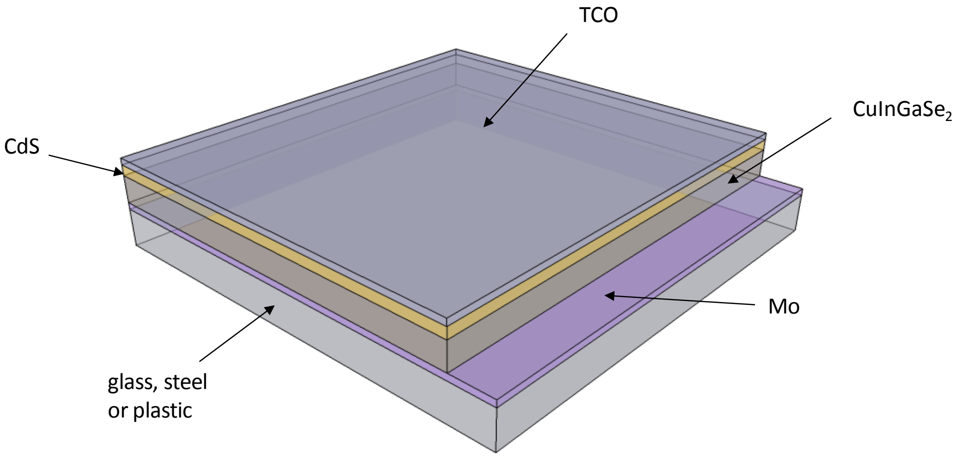

Figure 1.7. CdS/ $CuInGaSe_2$ solar cell in substrate configuration

Si thin films are typically deposited using silane, SiH_4 and hydrogen, H_2 by physical vapour deposition (commonly plasma-enhanced (PE-CVD)) where the deposition parameters can be varied to yield either hydrogenated amorphous Si (a-Si:H) or microcrystalline Si (μc-Si), or indeed a combination of both materials [15] to produce an all Si tandem cell. a-Si:H with E_g = 1.7 eV absorbs strongly in the visible part of the spectrum contrasting with μc-Si with E_g = 1.1 eV which absorbs strongly in the near –IR. The presence of deep level defects in Si thin films caused by dangling and twisted bonds make for an unfavourable comparison in terms of device conversion efficiency, η to their crystalline analogues, though significant cost saving potential make these materials economically very attractive. Thin film Si technologies use considerably less feedstock material and for a-Si:H can be deposited at relatively low temperatures allowing for a greater flexibility of applications, including large area roll-to-roll deposition onto flexible substrates. Thin film Si can be found in both substrate and superstrate configuration [16] where a p-i-n structure is usually adopted to compensate for carrier mobility discrepancies.

1.7 CdTe in thin film PV

The modern p-CdTe-n-CdS heterojunction solar cell was first developed in 1968 by Bonnet et al [17], with efficiencies of 10% achieved by 1972 [18]. CdTe, a direct band-gap II-VI compound semiconductor, was identified as being particularly suited to PV applications with a near optimum bandgap of 1.45 eV and a high absorption coefficient, $\alpha \sim 5 \times 10^5$ cm^{-1} with ~ 99% of incident photons with energy greater than the band gap absorbed within a 2μm layer thickness [19]. Figure 1.6 illustrates a typical CdS/CdTe solar cell in superstrate configuration, where initially a TCO layer is deposited onto an optically transparent substrate. Two primary duties are required of this front contact layer;

1. High conductivity (R_{sheet} = 5 to 15 $\Omega\,\square^{-1}$)
2. High visible and near- IR transmission – wavelengths which are highly absorbing in the CdTe absorber layer.

Following the TCO front contact layer, an n-type window layer is deposited. Cadmium sulphide, CdS is commonly used as the window layer material forming the n-type component of the pn structure, in CdTe solar cells [20]. CdS exhibits both good visible and near - IR transmission, with a direct bandgap of 2.42 eV, and good photoconductivity. Deposition of the CdTe absorber layer completes the pn structure, forming the depletion region where generated charge carriers are separated, as detailed in section 1.5 above.

As a direct band gap semiconductor, electronic transitions in CdTe from the valence band into the conduction band requires only photon absorption. This is in contrast to indirect band gap semiconductors such as Si, which in addition to photon absorption requires simultaneous absorption (or emission in the case of radiative recombination) of a lattice phonon to overcome the difference in electron and hole momentum, as shown in Figure 1.8. Due to this, photons can penetrate much further into an indirect-gap material than a direct-gap material. For PV applications this means that direct-gap materials are favourable compared to indirect-gap materials as much less material is required to absorb incident photons.

A maximum conversion efficiency of 17.3 % has been reported by First Solar Inc [21] for research scale device. This falls considerably short of the Shockley – Queisser limit for a single junction solar cell and has been attributed to slow research and development progress in activation treatments and difficulties forming an ohmic back contact with the CdTe absorber without degrading the full device [19]. Practical limits based on cell construction reduce the estimated maximum conversion efficiency to 17.6% [22], where practically achievable carrier mobility and carrier lifetimes can only lead to small gains in open-circuit voltage, V_{oc} and fill factor, FF.

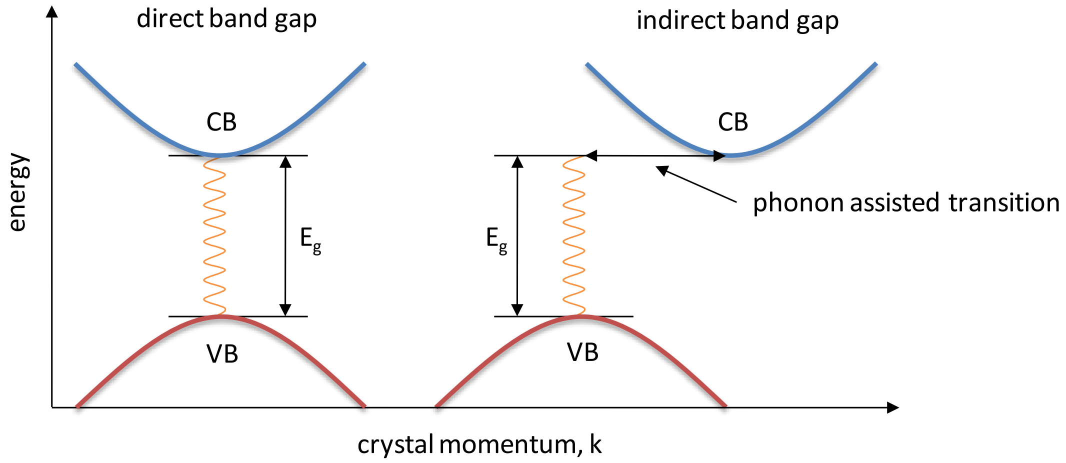

Figure 1.8. direct band gap vs. indirect band gap semiconductors

1.8 Alternative and emerging PV technologies

Where established Si technology is generally considered as first generation solar, and thin film technology as second generation, the third generation ambiguously encompasses several emerging technologies which are currently the focus of significant academic and industrial research. These include dye-sensitized solar cells (DSSC's) [23, 24], organic polymer solar cells [25], multi-junction [26] (as discussed in section 1.6), quantum dot [27] and intermediate band [28] solar cells. These novel third generation approaches to PV conversion often include ‘photon management’ techniques such as up and down conversion and thermal technologies, such as thermophotonics [29].

Dye-sensitized solar cells (DSSC) were first proposed and developed by Gretzel et al [23]. This design, illustrated in Figure 1.9 below uses porous TiO_2 nanoparticles coated in ruthenium-polypyridine dye to absorb incident photons, allowing for the ‘injection’ of electrons into the TiO_2 CB followed by diffusion to the SnO_2:F TCO anode. A I^-/I_3^- redox couple reaction completes the circuit. Peak DSSC conversion efficiencies of 11.2 % have been reported [10]. DSSC design is technically very appealing due to its relative simplicity and use of low-cost feedstock materials leading to economically attractive manufacturing opportunities.

.

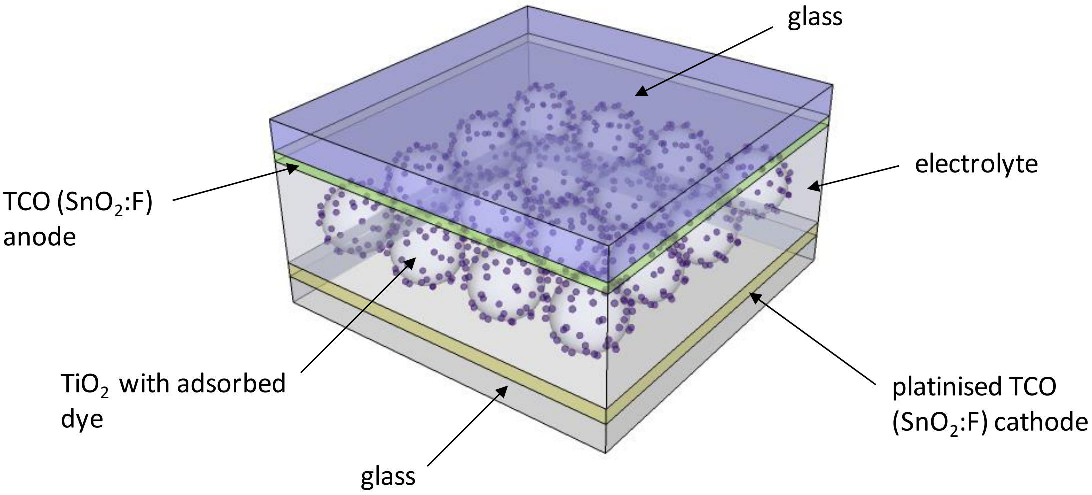

Figure 1.9. Schematic diagram of a dye-sensitized solar cell (DSSC)

Organic photovoltaic cells (OPVC) use organic molecules and polymers such as phthalocyanine to form conjugated systems where the separation of bonding π orbitals (the highest occupied molecular orbital (HOMO)) and anti-bonding π^* orbitals (the lowest unoccupied molecular orbital (LUMO)) create the materials’ band-gap. Exciton separation is achieved by the introduction of effective fields, this can be between the organic absorbing material and an electrode in the case of a single layer OPVC, or between two organic materials with different electron affinities and ionization energies (electron donor and acceptor materials) in the case of bilayer and bulk heterojunction OPVC’s. Konarka®, a company capitalizing on the low-cost and flexible potential of OPVC claim the highest efficiency to date of 8.3 % [10]

Quantum dot ‘QD’ solar cells use nano-sized particles called quantum dots, where quantum confinement effects allow for highly tunable bang gap engineering. This is an attractive physical property in PV research which provides the opportunity to tailor the E_g to specific spectral requirements. QD’s are typically contained within a colloidal suspension in a conductive polymer and examples using CdTe, PbS, GaAs and Si QD’s have been successfully demonstrated, though conversion efficiency remains relatively low (< 6%). QD’s have been used to produce intermediate band (IB) solar cells which work on the principle of impurity introduction to form intermediate E_g states. This allows for absorption of photons with $E < E_g$ where two sub-E_g photons are absorbed to produce one electron-hole pair. This approach provides the opportunity to broaden spectral absorption, but is not without its challenges; such as the inherent recombination mechanisms IB’s create. These examples highlight the potential synergy between developing third generation technologies.

Photon management techniques encompass several approaches where the characteristics of incident photons are artificially altered. These technologies include luminescent solar concentrators where luminophores are used to collect incident photons. Once trapped by total internal reflection, photons are guided to the edges of the collector and absorbed by very small area solar cells. Other approaches include luminescent down shifting (LDS) [30], where high energy photons, that are typically beyond the spectral response of many solar cells are absorbed and re-emitted at longer wavelengths, where the solar cell is strongly absorbing. Conversely, photon up-shifting operates via the absorption of two (or more) low energy photons, followed by photon emission at a shorter wavelength where device absorption is high, this leads to increased device short-circuit current, I_{sc} by artificially extending a device’ spectral response beyond the lower band edge.

Concentrator photovoltaics (CPV), is a technology which concentrates sunlight onto relatively small area solar cells, leading to significantly increased power output. A sensitive balance of several considerations including; PV device and concentrator equipment costs, cooling requirements, geographical location and local insolation promise significant economic advantage over conventional PV technology.

For low concentration systems, of between 2 to 100 suns, the heat flux remains low enough to negate active cooling requirement. These systems also have a high acceptance angle therefore don’t generally require active solar tracking. For concentrations between 100 and 300 suns, either passive or active cooling and solar tracking systems are generally required, increasing system costs, though in balance with increased power output. For systems concentrating sunlight to over 300 suns, concentrating optics, such as heliostats or Fresnel lenses are used. These systems create much higher levels of heat flux, necessitating high-capacity heat sinks to prevent thermal damage and control temperature related cell performance losses. Triple junction solar cells are commonly used in high concentration PV systems, proving economically attractive due to their high conversion efficiencies.

The increased costs of high concentration systems are compensated for by significant increases in power generation. For example, IBM have developed a 2300 sun concentrator system, where incident sunlight is concentrated to 230 W cm^{-2} onto a multi-junction solar cell which at a 30% conversion efficiency is capable of generating 70 W cm^{-2} [31]. This is a massive improvement on existing CPV systems which typically operate at concentrations of around 200 suns; this leap forward is made possible via the application of microchip cooling technology to photovoltaics. This type of industry synergy and technology hybridisation is beginning to be found commonplace in PV, and appears to provide firm foundations on which the third generation technology can expand and increasingly find commercial applications without the necessity for significant government subsidies.

The Mildura Solar Concentrator Power Station scheduled for completion in 2013 in northern Victoria, Australia, will be the largest facility of its kind. This system uses heliostat concentrator photovoltaics (HCPV), [32] a branch of CPV technology which use angled mirror collectors to concentrate sunlight on to high-efficiency multijunction PV solar cells. The solar power station will have a generating capacity of 154 MW, equating to 270,000 MWh/year, enough to satisfy the electrical demands of 45,000 homes over a year.

1.9 Electrical Characterisation of Solar Cells

PV solar cell performance is commonly described by its current-voltage (I-V) characteristic; where the cell is biased over a predetermined range and the current is measured under AM1.5 illuminated conditions at 25 °C. Figure 1.10 illustrates such a setup. Cell contacting methodology will vary depending on contact architecture; Figure 1.10 shows a typical test setup for a superstrate PV device, where both front and back contacts are approached from the rear of the cell.

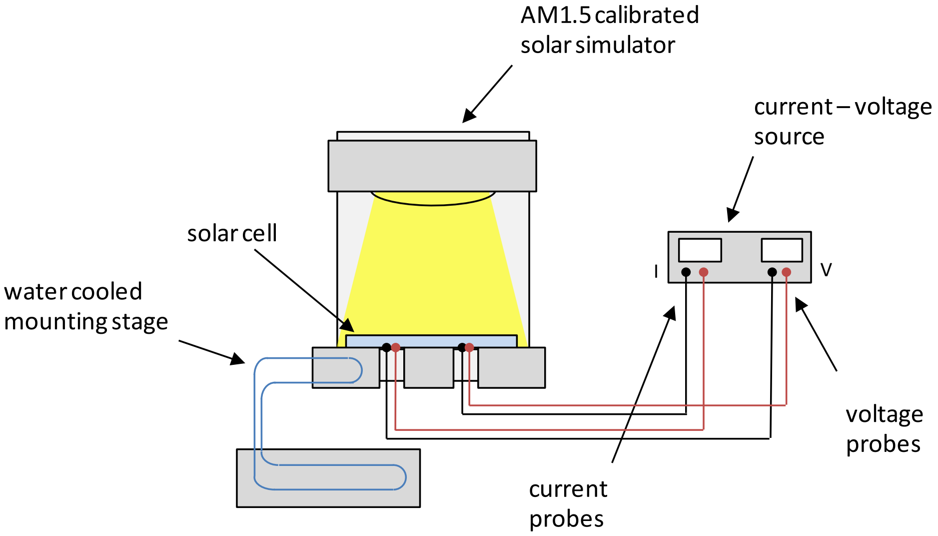

Figure 1.10. current -voltage setup for solar cell characterisation

The diversity of solar cell dimensions found in the PV research and manufacturing community leads to a wide distribution of photocurrent generation, so as to effectively normalize these I-V measurements, a spatially defined cross-sectional current density (J), is calculated and units of mA cm^{-2} are adopted. The measurement of a J-V plot as shown in Figure 1.11 ensures that like-for-like comparisons can be drawn between different sized cells.

A J-V plot provides the key parameters used to describe solar cell performance; short-circuit current density, J_{sc}; measured at V = 0, open-circuit voltage, V_{oc}; measured at J = 0, fill factor, FF; cell conversion efficiency, η; series resistance, R_s and shunt resistance, R_{sh}.

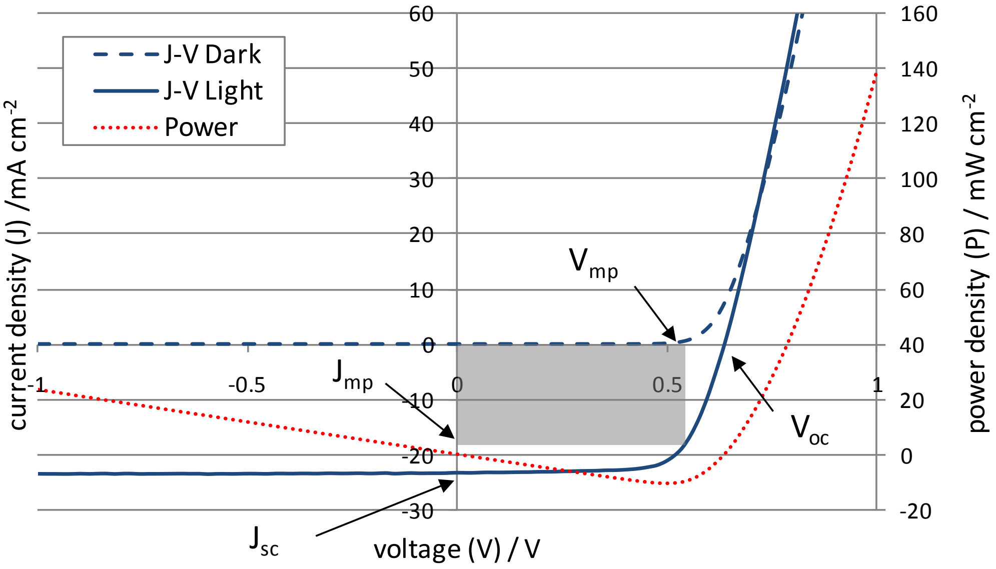

Figure 1.11. Example of J-V plot including power curve

The equivalent circuit of a solar cell, as shown in Figure 1.12 shows that total cell current; I, can be defined by the light generated current; I_L, the diode current; I_D, and the shunt current; I_{sh}. In short-circuit conditions I = I_{sc}.

$$I = I_L - I_D - I_{sh} \tag{1.1}$$

I_D is described by the Shockley diode equation by the reverse saturation current; I_s, the elementary charge; e, the voltage across the diode; V + IR_s, the diode ideality factor; n, Boltzmann's constant, k and temperature; T:

$$I_D = I_S \left\{ \exp\left[\frac{e(V + IR_s)}{nkT}\right] - 1 \right\} \tag{1.2}$$

I_{sh} is defined by the voltage across the diode, V + IR_s and the shunt resistance; R_{sh} as shown in Equation [1.3]:

$$I_{sh} = \frac{V + IR_s}{R_{sh}} \tag{1.3}$$

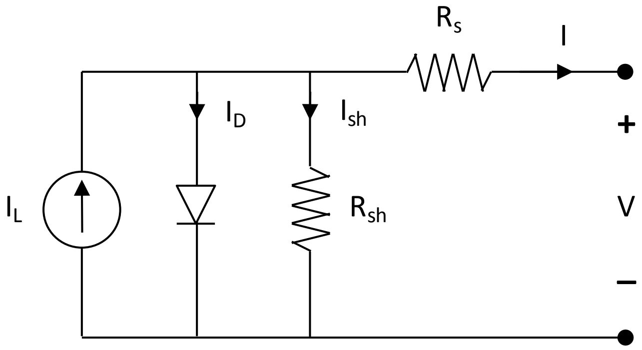

Figure 1.12. Solar cell equivalent circuit

The substitution of Equations [1.2] and [1.3] into Equation [1.1] provides the characteristic PV solar cell equation, including R_s and R_{sh} contributions:

$$I = I_L - I_S\left\{\exp\left[\frac{e(V + IR_s)}{nkT}\right] - 1\right\} - \frac{V + IR_s}{R_{sh}} \qquad [1.4]$$

Open-circuit voltage; V_{oc} is described by Equation [1.5] and is shown to be dependent on the reverse saturation current; I_s a parameter relating to the CdTe acceptor level, as well as the carrier concentration, lifetime and diffusion coefficient.

$$V_{oc} = \frac{nkT}{e}\ln\left(\frac{I_L}{I_s}\right) \qquad [1.5]$$

Fill factor; FF, as shown in Equation [1.6] shows the ratio of maximum achievable power versus the maximum theoretical power and refers to the ‘squareness’ of the light diode curve, illustrated as the shaded region in Figure 1.11.

$$FF = \frac{V_{mp}\,J_{mp}}{V_{oc}\,J_{sc}} \qquad [1.6]$$

Equation [1.7] describes the cell conversion efficiency; η, as derived from parameters extracted from the J-V curve as shown in Figure 1.11.

$$\eta = \frac{V_{mp}\,J_{mp}}{P_{in}} = \frac{FF\,V_{oc}\,J_{sc}}{P_{in}} \qquad [1.7]$$

η expands on the information provided by the fill factor to supply the ratio of generated power to incident power; 100 mW cm^{-2} or 1 sun for STC.

1.10 Ph.D project focus

This chapter has so far introduced, in historical context, some of the various types of solar cell technology at the centre of current PV research and development, and also mature technologies that have seen significant commercial successes in recent years. As presented in section 1.9 a comprehensive understanding of the electrical characteristics of the materials used for PV is crucial in optimizing the physical structure of a solar cell, therefore the metrology and characterisation of solar cells is a key part of solar cell research and development. Typically, characterisation techniques, such as J-V measurements (presented in section 1.9) and external quantum efficiency (EQE) measurements (though the later achieves spectral resolution) lack spatial resolution, whereby the measurements are averaged over a predetermined lateral area. This inherently results in the convolution of recorded information, essentially averaging a result over a measurement area. This can be determined by either the back (or front) contact area and/ or the incident illumination beam dimension. For example, in J-V measurements, AM1.5 illumination incident on a full contact area has the effect of averaging the total performance of a cell to yield a single set of descriptive parameters. Though important and interesting these are, further information can be extracted from the cells under inspection by adding a spatial resolution dimension to the measurement, where smaller components of a cell are measured to cumulatively produce a spatially resolved ‘image’, separating the originally convoluted components of the cell. This process could be compared to pixels in a digital image, where each pixel represents spatially resolved information dependent on the signal recorded from a CCD array, and placed together, in the correct configuration an image can be produced.

The focus of this project and thesis therefore aims to examine primarily CdTe solar cells at relatively high spatial resolution, in a way similar to how a digital camera records a scene using electrical signals to reconstruct a digital representation of that scene using pixels; a solar cell will be separated into smaller divisible components (pixels) to yield spatially resolved images, or maps to describe cell performance and the electrical properties of polycrystalline CdTe thin films. This will be primarily achieved using two spatially resolved characterisation techniques:

1. Laser beam induced current (LBIC) measurements
2. Scanning probe microscopy (SPM) based derivatives:
    (a) Scanning Kelvin probe microscopy (SKPM)
    (b) Conductive atomic force microscopy (CAFM)

Chapter 2, a literature review, will present the development of CdTe thin films for PV applications and the variety of deposition methods used. Furthermore, performance optimization steps and proposed loss mechanisms will be presented and discussed. Chapter 2 will also present the LBIC and SPM techniques as they have been typically applied in materials research with a focus on materials used in the PV research community.

Chapter 3 will briefly describe the cell fabrication process used at the Centre for Solar Energy Research (CSER); metal organic chemical vapour deposition (MOCVD) and the routine cell characterisation methods; J-V and EQE measurements used to quantify cell performance. Furthermore, the following materials characterisation methods: scanning electron microscopy (SEM) and complimentary energy dispersive x-ray (EDX) analysis, and stylus profilometry will be briefly discussed in context to their relevance in CdTe device research and development. Chapter 3 will focus on the optimisation of an LBIC instrument for performing spatially resolved photocurrent measurements on CdTe solar cells. This chapter will also describe the SPM derivatives used for electrical measurements of CdTe solar cells, and describe the conditions found for optimum image quality.

Chapter 4 and 5 will present the principle results revealed using the described characterisation techniques. Chapter 4 will describe the results obtained from LBIC measurements on $Cd_{1-x}Zn_xS$/ CdTe devices, where correlations are drawn against various alternative measurement techniques. Further studies on luminescent down shifting (LDS) layers incorporated into CdTe device structures are also presented and discussed. Chapter 5 will describe results from SKPM and CAFM studies, presenting the effects of p-type doping in CdTe on the measurable contact potential difference (CPD) between the probe tip and CdTe sample surface, and furthermore, the subtle changes in CPD at grain boundaries. Finally, the intricacies of CAFM measurements are discussed, with conclusions that are found to corroborate with observations in SKPM measurements.

2 Literature Review

The primary focus of this thesis centres on the spatially resolved characterisation of CdTe thin film solar cells grown by metal organic chemical vapour deposition (MOCVD). The following review will discuss the advantages and challenges of working with polycrystalline thin films, with a focus on thin film CdTe. Routine 'area-averaged' characterisation techniques will be discussed in contrast to spatially resolved approaches. The development of the all-in-one MOCVD process will be discussed with a focus on its suitability and potential for scalable thin-film photovoltaic solar cell production.

2.1 Preparation of polycrystalline CdTe

CdTe was first proposed as a suitable photovoltaic material in the 1950's [33, 34]. As both n-CdTe and p-CdTe are readily producible, several photovoltaic heterojunction structures including n-CdTe/p-Cu_2Te [35] and ZnO/ p-CdTe [36] have been proposed. n-CdTe saw limited success, conversely p-CdTe was quickly shown to successfully form an effective photovoltaic heterojunction with n-CdS. As recognised today, the modern CdTe solar cell was developed in the early 1970's with Bonnet and Rabenhorst's development of a thin film graded-gap p-CdTe/ n-CdS heterojunction solar cell. This exhibited conversion efficiencies of between 5 – 6 % under 50 mW/ cm^{-2} illumination [17]. n-CdS was shown to provide a good balance of optical and electrical properties, with a band gap of 2.4 eV and good conductivity under illumination. Examples of single crystal p-CdTe/ n-CdS [37] structures were also demonstrated in the 1970's with conversion efficiencies of 7.9 % under 85 mW cm^{-2} illumination, though this coincided with the rise of polycrystalline thin film CdTe demonstrating its future potential, with Kodak patenting process technology for thin film CdTe cells with conversion efficiencies of 8.9 % under 75 mW cm^{-2} illumination in 1978 [38].

Continued research through the 1980's saw Kodak increase laboratory scale device efficiencies to over 10 %. This was followed by subsequent conversion efficiency records of 15.8 % in 1993 by Ferekides *et al.* [39] and 16.5 % in 2001 by NREL [40]. This most recent record stands to date for the highest published CdTe device efficiency over a 1 cm^2 area at AM1.5 illumination.

CdS and CdTe thin films have been successfully produced via a variety of deposition processes. Among them include: electrodeposition (ED), chemical bath deposition (CBD), close-spaced sublimation (CSS), sputtering and chemical vapour deposition (CVD). ED has been widely demonstrated to produce CdTe thin films from solution based precursors such as $CdSO_4$ and TeO_2, deposition has been demonstrated onto both stainless steel (SS) [41] and tin oxide, (SnO_2) coated glass [42]. ED has shown good scalability potential, the process lending itself well to large area thin film deposition, though limited by comparatively low deposition rates, which has restricted significant uptake to date.

CBD has been widely used to deposit both n-CdS and n-$Cd_xZn_{1-x}S$ films for high efficiency CdTe devices. CBD deposits thin, adherent and optically transparent films from a reaction between cadmium acetate, ($Cd(CH_3CO_2)_2$) and thiourea, ($SC(NH_2)_2$) in an ammonia solution [43]. The addition of 10% zinc acetate, ($Zn(CH_3CO_2)_2$) to this solution has been shown to successfully yield $Cd_xZn_{1-x}S$ structures for incorporation into both CdTe [44] and $CuInGaSe_2$ [45] solar cells. CBD CdS films are known to suffer from low crystal quality and high concentrations of impurities; this has led researchers to explore alternative dry processes (such as CSS) which have higher scalability and manufacturing potential. Interestingly, higher quality non-CBD CdS films have not yielded higher performance CdS/CdTe solar cells, and several studies exploring beneficial impurities, such of oxygen, found in CBD CdS have been reported [46, 47].

Perhaps the most common CdTe growth technique; CSS has been extensively demonstrated since early successes were reported by Bonnet *et al.* [17]. CSS typically operates at high temperature, under vacuum conditions in a quartz reaction vessel. A high purity source; 99.999% CdTe granulate is vaporised from an open carbon crucible, followed by deposition of 3 to 8 μm of CdTe onto a heated substrate. Source/ substrate separation is typically between 2 and 20 mm. The substrate is actively or passively heated. Figure 2.1 illustrates a system where both source and substrate are actively heated, where respective temperatures are typically 600 and 700 °C [43]. Alternatively, the source is actively heated and the substrate is passively heated by its close proximity to the source, in this arrangement the source temperature is typically ~ 600 °C and the substrate ~ 540 °C [48]. Growth pressures of 2 to 30 Torr in an ambient of N_2 [43], O_2 [48] or O_2/He [40] have been reported. The scale-up of the CSS process and manufacture of thin film CdTe solar cells has been successfully demonstrated, where the laboratory batch process has been translated to a large area roll-to-roll process [18]. Though commercially attractive due to its simplicity and reproducibility, the CSS process suffers from poor controllability and hence poor materials utilization, and in an industry where feedstock material cost is a significant driver determining total module cost, recent years have seen considerable interest in reducing materials usage.

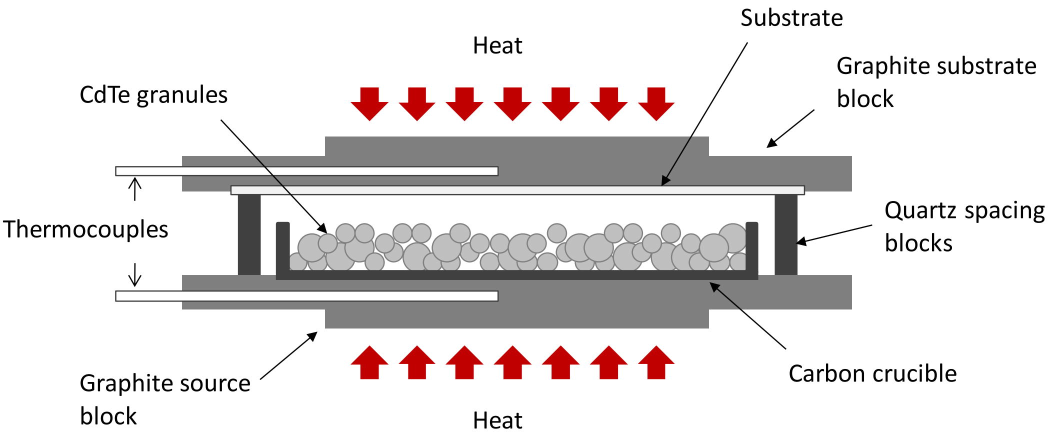

Figure 2.1. Close-spaced sublimation schematic

As discussed in chapter 1, CdTe absorbs 99 % of incident photons within 2 µm of material. Film thicknesses common in CSS manufacture are typically 5 to 8 µm, this is significantly higher than is optically necessary and presents substantial potential for feedstock usage and cost reductions. This has led academic and industrial researchers to explore alternatives such as metal organic chemical vapour deposition (MOCVD) [49] and sputtering [50] where high process controllability is readily achievable.

CdTe solar cells have been successfully grown by sputtering. This is a form of physical vapour deposition (PVD), where high energy particles are bombarded into a target at relatively low temperatures under vacuum. The momentum transfer between the ions and the atoms in the target drives a process where the ejected atoms from the target can deposit onto a substrate. Commercially, sputtering is an attractive deposition technique, where both CdS and CdTe thin films can both be grown with a high degree of controllability [50, 51]. Although sublimation techniques have yielded record CdTe conversion efficiencies, sputtering has also produced a respectable 14.0 % using a ZnO:Al TCO [52]. Proposed losses have been attributed to polycrystallinity effects and incomplete doping and film thickness optimization. Potential optical gains have been proposed where the influence of the CdS window layer and ZnO buffer layer thickness is significant [53].

CdTe/CdS thin film solar cells are most commonly deposited onto transparent conducting oxide (TCO) coated glass substrates. All citations so far have demonstrated deposition onto either boroaluminosilicate glass or soda lime glass with substrate thickness commonly between 3 and 5 mm. The use of glass substrates in thin film PV manufacture has both advantages and disadvantages; glass can withstand high temperature deposition processes and provides a structurally rigid component of the cells encapsulation. Conversely, glass does not allow for shape adaptability and offers little weight saving opportunity; an important consideration for space applications. Alternative flexible substrates with thicknesses of between 10 to 50 μm have been proposed and examples demonstrated. These include polyimide films, where high optical transmission allows for superstrate configuration solar cells [54] and stainless steel (SS), Mo, Ni and Cu foils for production of cells in substrate configuration. Mo is seen as the most appropriate due to its closely matched thermal expansion coefficient with that of CdTe [55, 56]. Conversion efficiencies in this fertile research area have to date been below those of their glass substrate counterparts, with metal foils and polymers yielding ~ 8 % and ~ 11 % efficient cells respectively. This has been recognised as being due to difficulties in forming an ohmic contact with the metallic substrate and incorporating a resistive buffer layer, where thermal expansion coefficient and work function matching requirements limit the choice of available materials [57].

2.2 CdTe cell activation

$CdCl_2$ has been historically recognised as an effective recrystallization mediator in CdS photoconductors [18]. Its use also forms a critical process step in CdTe/CdS cell fabrication. The use of $CdCl_2$ and its considerable effect on cell performance is commonly referred to as an ‘activation’ process, without which cell performance is known to significantly diminish. The mechanism via which the $CdCl_2$ treatment operates and the effect it has on the thin films is not fully understood and many studies have aimed to more fully describe this process where both morphological and electronic changes have been observed to occur. It has been proposed that the treatment activates the junction by reducing the density of interface states at the heterojunction, and this leads to a reduction in reverse saturation current; a voltage-limiting parameter. Furthermore, it has been shown that the $CdCl_2$ treatment also passivates the grain boundary (GB) network; a fundamental polycrystalline defect structure and potential carrier loss pathway. Recent studies have indicated that following the $CdCl_2$ treatment, charge separation is not only impervious to the GB network, but actually increases at GB's [58]. This has been attributed to enhanced GB conductivity and the formation of variable potential barriers that enhance hole transport. These considerations have led to proposals that the band structure at GB's leads to enhanced photogenerated charge carrier separation [59]. Commonly the $CdCl_2$ passivation treatment is accomplished via the deposition of a thin film of $CdCl_2$ followed by an anneal at ~ 400 °C under nitrogen or oxygen. Deposition has been demonstrated using physical vapour deposition (PVD), [60], by spraying an aqueous solution of 0.01M $CdCl_2$ in methanol [61] and by metal organic chemical vapour deposition using dimethylcadmium and tertiarybutylchloride or n-hexylchloride precursors [62].

2.3 CdTe cell losses

Further to the resistive losses described by the J-V curve in chapter 1, photogenerated carriers can recombine prior to separation at the junction. This can occur via several well documented pathways; for a single crystal semiconductor there are 3 main recombination types: radiative recombination, Shockley-Read-Hall (SRH) recombination and Auger recombination. Each of these processes contribute to a reduction in solar cell performance. Radiative recombination occurs via a simple CB to VB transition, accompanied by the radiative emission of a photon. Auger recombination occurs via a similar process but the energy released promotes an intra-CB transition (an electron close to the CB edge is promoted to a higher energy state). The promoted electron will then thermalize back to the CB edge. SRH recombination refers to a defect related transition where an energy state is introduced in the band gap of the semiconductor. A two stage process, SRH recombination occurs when (a) an electron (or hole) is trapped in the mid-band gap energy state followed by (b) the transition of a hole (or electron) to the same mid- band gap energy state before the electron is thermally re-emitted into the CB. SRH recombination is statistically more probable the further the defect energy state is from either of the band edges due to thermalization effects.

The nature of polycrystalline solar cells result in an intrinsically high defect density, and hence are commonly considered an inferior alternative to their single crystal analogues. In the case of group IV materials and III-V compounds this is certainly the case, with μc-Si performing unfavourably when compared to bulk Si with GaAs following a similar trend [63, 64]. Though interestingly, this is not always the case, with $CuInGaSe_2$ and CdTe polycrystalline solar cells actually outperforming their single crystal counterparts [13]. These exceptions to a widely recognised rule require some special consideration in order to understand both material aspects and device operation.

Theory predicts that the inherent breaks in the periodicity of polycrystalline material will create potential recombination sites. This will impact the photogenerated current, I_L by allowing carriers to recombine before diffusing toward the junction thus reducing the minority carrier lifetime. For many years, GB's have been considered to be sites of significant recombination where localized energy states within the band gap create trapped localized charges (SRH recombination). These charges were thought to form electrostatic potential barriers for carrier transport across the GB interface, reducing minority carrier lifetime, increasing the reverse saturation current and decreasing overall cell I_L and V_{oc}. This hypothesis has led many researchers to promote the growth of larger grains in their materials to reduce the extent of the GB network and their proposed effects on I_L via the formation of recombination centres.

Conversely, Bosio *et al.* have suggested that GB's, once passivated (as introduced in section 2.2) can contribute positively to overall cell performance. It has been proposed that the GB's in both CdS and CdTe provide a site for the concentration of structural defects and impurities. This theory suggests that GB's are passivated by the diffusion and subsequent segregation of dielectric materials, like CdF_2, $CdSO_3$, and $CdSO_4$ in CdS and $CdTeO_3$ in CdTe films, and this leads to enhanced carrier transport in the bulk grains. If these impurities can be segregated and confined to localized areas in the material, this suggests that the crystallinity of individual grains can be improved. Based on this hypothesis, it has been proposed that the bulk grains in polycrystalline CdTe will have higher crystalline purity than that found in single crystal analogues. This goes some way to explain how some materials, including CdTe and $CuInGaSe_2$, can outperform their single crystal analogues [13].

Visoly-Fisher *et al.* has further suggested that GB's, with a high concentration of Cl_{Te} donor defects lead to a unique doping profile which act to channel minority carriers towards the junction. This theory suggests that hole depletion at GB's leads to increased band bending. Figure 2.2 illustrates a mechanism where electrons are drawn into the GB core and flow toward the pn junction and conversely holes flow through the grain bulk toward the back contact. This theory indicates that the potential gradient of the GB depletion layer creates multiple junction sites that can be considered to be operating in parallel with respect to one another. Some of these will be bulk grain CdTe/CdS interfaces and others GB CdTe/CdS interfaces, where both can contribute to the separation of photogenerated charge carriers, reducing carrier recombination and enhancing carrier collection [65, 66]. A similar model has been proposed where a small electron barrier has been observed at GB's leading to enhanced collection of photogenerated minority carriers [67, 68].

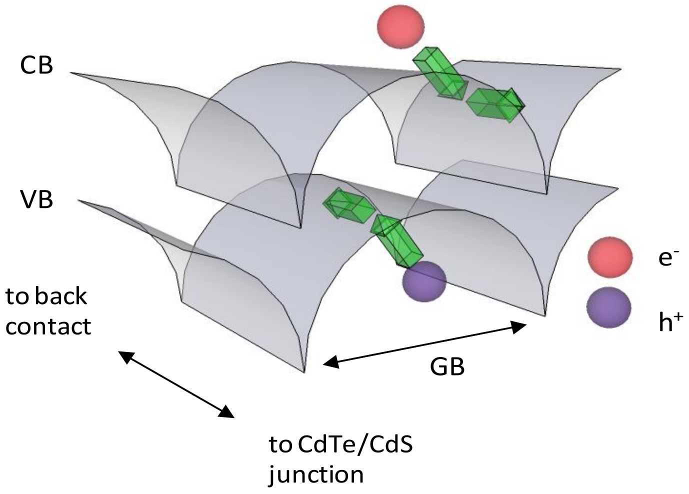

Figure 2.2. Predicted band-bending at grain boundaries, promoting separation of photogenerated charge carriers.

These examples cite an accumulating body of evidence which support the theory that GB networks in polycrystalline solar cells contribute positively to cell performance and goes some way to explain how polycrystalline cells can outperform their single crystal analogues.

Further electrical losses are generally attributed to contacting methodologies and reflect the difficulties in making a functional contact to the high work function, Φ CdTe, (Φ = ~ 5.5 to 5.9 eV). A common approach to address this issue is to use a high Φ metal such as Au (Φ = 5.1 eV), this attempts to alleviate the effects of the Schottky barrier at the metal-semiconductor interface, by closely matching the Φ of both materials. Unfortunately, Au is not an economically sustainable answer to this issue, and other metals struggle to achieve an effective ohmic contact to the CdTe back surface. This has led researchers to explore alternative avenues, these can be summarised by; (a) CdTe back surface doping (b) CdTe back surface etching, (c) forming an intermediate semiconductor between the CdTe back surface and the metal contact and (d) forming high Φ alloys.

CdTe back surface doping has been successfully demonstrated by Barrioz *et al.* [69] in an all-in-one MOCVD process. Thin layers (~ 250 nm) of highly Arsenic (As) doped CdTe at 1.5 × 10^{19} atoms cm^{-3} concentration were used to increase acceptor concentration. These structures were observed to decrease device series resistance (R_s), without any wet-etch processing requirements. Conversely, CdTe back surface wet etching has been widely reported, most commonly: nitric acid/ phosphoric acid (HNO_3, H_3PO_4 and H_2O) [70] or bromine in methanol (Br/ CH_3OH) [71]. These have been recognised to deplete the CdTe back surface of Cd, and form a conductive Te- rich layer, which significantly improves the electrical behaviour of the back contact. Further work has been reported where intermediate layers are introduced into the device structure to improve contact stability and resistance. The deposition of ZnTe:Cu with Ni back contacts achieving > 12 % conversion efficiency have been reported by Gessert *et al.* [72] and Sb_2Te_3 with both Ni and Mo contacts by Abken [73]. Furthermore, composite alloys of Ni, Cu, Sn, and Au have been reported as potential candidates for suitable CdTe back contacts [74].

2.4 Spatially resolved vs. area-averaged metrology

In terms of spatial distribution, cell loss mechanisms can be either common to a full device, such as ineffective activation treatments, or isolated to a spatially defined region of a cell, such as pin-holes, film damage and contamination or thickness and composition variations. Area-averaged techniques such as I-V and external quantum efficiency (EQE) measurements successfully describe macroscopic PV behaviour, but they are unable to separate spatially dependent contributions and isolate defective areas. These measurements are typically averaged over the photoactive region of the cell, often limited by the front and/or back contact architecture. In polycrystalline solar cells, spatial variations will inevitably arise, whether at the nanometer-scale at grain boundaries and film interfaces or at the micrometer-scale where growth related defects can impact cell performance. Different approaches are required so that the separation of these contributing factors can be achieved.

This section will focus on the background, relevance and applicability to PV device research of two spatially resolved methodologies that have been at the focus of this work:

(a) Beam induced current measurements, and
(b) Scanning probe microscopy

Where common metrology approaches average their measurements over a spatially defined area, scanning probe techniques allow for high resolution spatially resolved measurements by effectively compartmentalising a cell into smaller areas. Each area is measured as a 3 dimensional coordinate, and used to plot an XYZ map. The XY dimensions are dependent on the total scan area and the Z dimension on an electrical parameter. In the case of beam induced current techniques the size of each sample area is dependent on:

(a) The step resolution of the scanning stage, and
(b) The incident beam width diameter.

For scanning probe techniques, the resolution is dependent on the step resolution of the scanning stage and the probe tip dimension (usually in the order of a few nanometers).

2.5 Beam induced current

The beam induced current technique has been reported under many guises. First demonstrated in 1951 by Goucher *et al.* when a scanned light spot was used to determine minority carrier lifetime in Ge from spatial variations in photocurrent [75] the technique gained interest in the 1970's and 80's with the advent of increasingly available laser technology. At the same time, developments in scanning electron microscopy (SEM) allowed for electron beam induced current (EBIC) measurements to be successfully demonstrated. These early EBIC measurements (as now) used an electron beam, which had been traditionally used to image a samples surface, to excite carriers in a semiconductor material and examine minority carrier and junction properties. In 1976, EBIC was used to analyse the influence of SiC particles in edge-defined film-fed grown Si ribbon solar cells [76], the technique allowing to spatially identify recombination effects caused by impurities. Further theoretical studies attempting to understand the interaction between the electron beam and an absorbing material were also reported, where a finite three-dimensional EBIC generation distribution was described by Fuyuki *et al.* in 1980 [77] as illustrated in Figure 2.3.

This model assumed a spherical generation region, part of which was above the sample surface and the maximum energy dissipation depth, d_g to be at the centre of this sphere. The generation sphere radius, r and d_g were found to be dependent on the accelerating voltage and the ratio d_g / r was assumed to be constant as shown in Figure 2.3(b).

Further models were also proposed for both light and electron beam induced current flowing in Schottky diodes and shallow pn junction [78] as well as the effects of grain boundaries [79, 80] on the induced current.

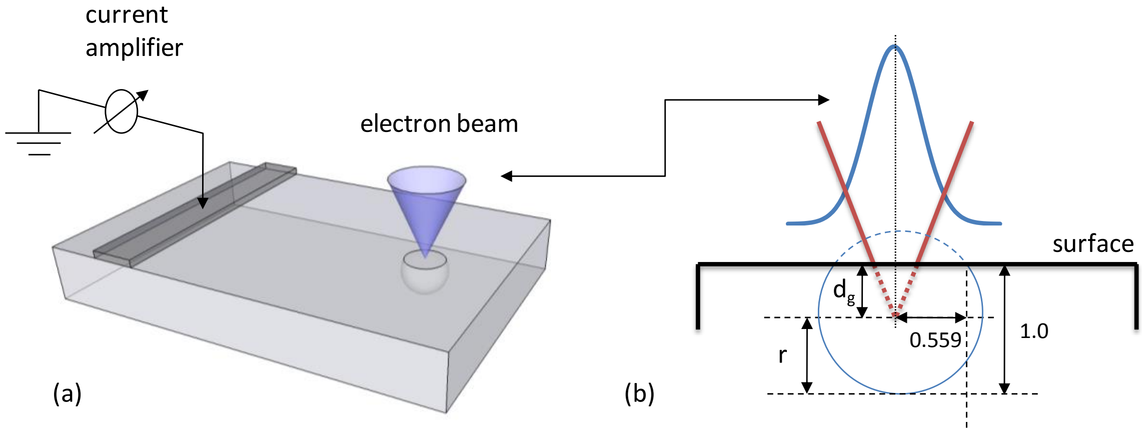

Figure 2.3 (a). Schematic of Fuyuki's EBIC generation volume and (b) schematic of electron penetration, where d_g is the maximum energy dissipation depth

These models considered the incident beam intensity profile to have a Gaussian shape with width, σ which broadened on entering an optically denser medium, this increase in σ was characterised by β, a parameter dependent on the angle of the incident light beam and the refractive index of the absorbing material. The exponential attenuation, (I) of the incident beam intensity (I_o) was described by Beer-Lambert's law:

$$I = I_0 e^{-\alpha d} \qquad [2.1]$$

Where α was the wavelength dependent absorption coefficient and d was the film thickness.

Figure 2.4 illustrates a model used by Marek [79] who developed a light beam induced current technique using a Kr^+ laser, reporting a beam width of 0.93 μm at λ = 647 nm. This system successfully extracted the diffusion length in "semicrystalline solar cell" grains and the recombination velocity at the GB's in this material.

The 'scanning light spot' technique was further demonstrated by Redfield [81], Young *et al.* [82], Sawyer [83] and Seager [84], all reporting its applicability in the investigation of Si grain boundaries (GB's). Redfield [81] considered the GB's as Si-Si interfaces and investigated the effects of annealing on cell activation showing that GB's were electrically inactive prior to heat treatment between 900 and 1000 °C. Young *et al.* [82] studied the effect of Li on the electrical properties of Si GB's using a HeNe laser at an incident beam width of ~ 20 µm at λ = 633 nm and reported an absorption depth of 2.8 µm. This system used rotating galvanometer mirrors (RGM) to raster the laser beam across a stationary sample and produce a 'scanning light spot' map. This rastering approach was in contrast to the mechanical XY translation stage and static light source used by Marek [79], now commonly used today, and reflected a rastering technique which was typically used prior to the advent of high precision XY stepper motors.

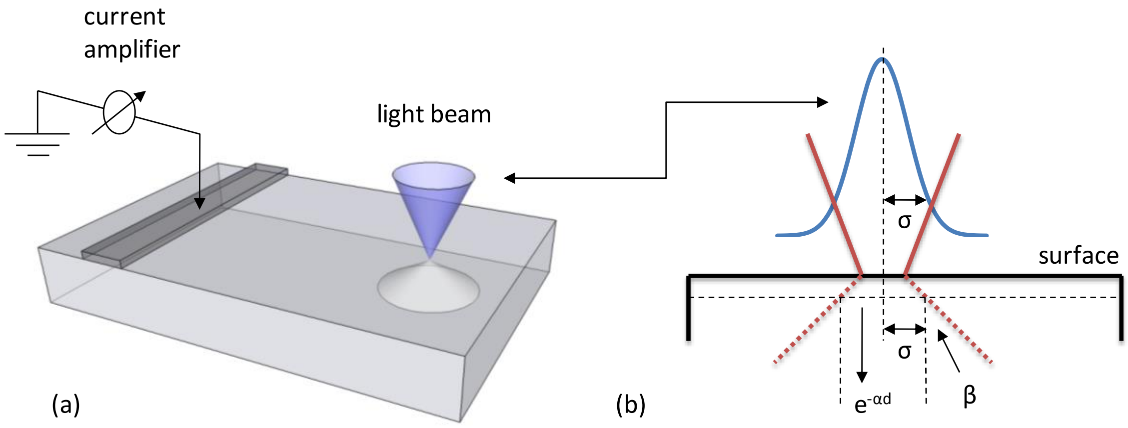

Figure 2.4 (a). Schematic showing the cone-shape absorption profile for light beam induced current mesurements and (b) schematic showing the geometry of the model used by Marek.

Difficulties in beam alignment and maintaining a focused beam over an extended scan area made the RGM approach unattractive in comparison to new stepper motor technologies. Young *et al.* used this experiment to examine the effectiveness of Li as a GB passivation agent and found that both majority carrier mobility and minority carrier recombination at GB's in polycrystalline Si were significantly improved.

Sawyer [83] reported the use of light beam induced current measurements on polycrystalline Si solar cells. This apparatus achieved beam widths of 4.0 ± 0.2 µm at wavelengths between 500 and 950 nm and reported single-axis line scans over 200 and 300 µm to identify the effect of hydrogen as a GB passivation agent. GB activity was evaluated before and after the passivation process step, and GB recombination velocity and diffusion length parameters were successfully extracted from the GB profile measurements. Seager [84] demonstrated the laser beam induced current technique to determine minority carrier diffusion lengths and GB recombination velocities in polycrystalline Si solar cells using a Kr^+ laser tuned to 568, 676 and 799 nm wavelengths reporting beam widths between 5 and 7 µm with approximately 5 %

scattering loss. This work supported earlier theories reported by Zook [78] which described a finite generation volume in LBIC measurements, dependent on the absorption coefficient of the semiconductor similar to that suggested by Marek [79] shown in Figure 2.4.

As interest in compound semiconductors for heterostructure photovoltaics increased, the beam induced current technique was successfully demonstrated on a range of PV devices including CdS/CdTe, $CuInGaSe_2$, InGaAs/GaAs and GaAs/Ge. The spatially resolved technique was used to characterise a range of parameters including majority carrier distributions and minority carrier diffusion length as well as GB passivation treatments and photocurrent generation uniformity over extended lateral ranges.

De Vittorio *et al.* [85] reported the sub-μm photocurrent mapping of InGaAs/GaAs and GaAs/Ge solar cells. This system used a tunable Ar laser focussed to 0.4 μm beam widths, where wavelengths of 351 and 517 nm were set according to the desired photon absorption depth. De Vittorio described a novel approach to beam width measurement where lines and spots impressed onto a photoresist film by the focussed beam were measured using atomic force microscopy. Typical approaches to beam width measurement often use the marginal distribution provided by a line scan taken over an abrupt junction between an active and inactive region of a cell. De Vittorio *et al.* detailed the optical beam induced current (OBIC) imaging of misfit dislocations in InGaAs/GaAs multi-quantum-well solar cells, where trapping centres were identified and associated with dislocation lines. These results were correlated with EBIC measurements on the same sample and were found to be more representative than the EBIC measurements, due to the experimental conditions being closer to the devices normal operating conditions. Furthermore, this study detailed the imaging of anti-phase boundary defects in GaAs/Ge solar cells. These were found to contain trapping centres which decreased vertically transported photocurrent. Application of OBIC measurements on non-PV devices is also discussed, where a GaAs Schottky diode, used in X-ray detection was characterised under various reverse bias conditions.

This example of beam induced current measurements being used to characterize non-PV device structures is not isolated. Spatially resolved photoluminescence (PL) measurements on semi-insulating GaAs crystals were reported by Visser and Giling [86] who used an Ar^+ laser at $\lambda = 488$ nm focussed to a 1 μm beam diameter. A novel approach was used, where the microscope objective and translation stages were contained within a liquid He cryostat. This allowed for fluctuations in impurity and native defect concentrations to be readily identified, where high quantum efficiencies were achieved due to the defects not being thermally ionized. PL was measured at λ = 488 nm and was found to yield information on dislocations and dislocation cell walls.

A further example of beam induced current measurements on non-PV devices is reported by Alietti *et al.* [87] and Shmidt *et al.* [88]. Alietti *et al.* studied the active region width and charge collection efficiencies of GaAs particle detectors. This setup used a filtered halogen lamp, producing light at λ = 700 nm and focussed to 1 μm beam width to produce photocurrent profiles from single axis line scans under a range of applied bias'. This arrangement was used to optimize the balance between spatial resolution and generation volume. Shmidt *et al.* also used the EBIC technique to investigate epitaxial GaN grown by MOCVD and successfully identified contrasting defect densities in two samples where carrier concentrations and Hall mobility were known to vary.

Beyond the applications discussed so far, the beam induced current technique has also been applied to thin film materials aimed at low-cost PV. Examples assessing post-growth treatments and photoresponse uniformity in CdTe and $CuInGaSe_2$ thin films PV devices have been reported. Brown *et al.* [89] described a technique for determining carrier collection efficiency and minority carrier diffusion length in $CuInGaSe_2$ using energy dependent EBIC where beam energies were varied between 2 and 30 kV. Cells incorporating different Ga profiles were examined. It was demonstrated that quasielectric fields, related to compositional grading, were beneficial to carrier collection and reducing back surface recombination.

Galloway *et al.* [90] used a scanning optical microscope (SOM) to produce optical beam induced current measurements on CdS/CdTe modules produced by ANTEC GmbH. This system used a 4 mW He-Ne laser and piezoelectrical rastering (other cited examples typically used XY stepper motors) for device translation reporting a resolution of between 2 to 4 μm. This investigation yielded detailed information on $CdCl_2$ and annealing post-growth treatments showing large differences in collection efficiency between the specimens studied. Furthermore, localized (50 to 100 μm) external quantum efficiency (EQE) measurements were carried out using a monochromated tungsten light source to isolate the junction characteristics in the same materials. This highlighted the buried junction characteristic of untreated CdS/CdTe solar cells.

Tandem optical beam induced current (OBIC) and EQE measurements have been further reported by Major *et al.* [48]. This system differed from Galloway's [90] by using a monochromated quartz halogen lamp for both EQE and OBIC measurements, an approach which although unable to achieve sub-micron resolution was able to record OBIC maps at any wavelength in the cells spectral response range. As such, resolution was limited to 12.5 μm. These measurements detailed buried junction characteristics and related them to CdTe absorber layer thickness. The OBIC results yielded evidence showing an inverse relationship between absorber thickness and area-averaged EQE, where the former decreased the latter was shown to increase. Lateral separation of poorly performing regions was also achieved where localised EQE measurements showed that cell performance was heavily dependent on shallow or buried junction characteristic.

Further work by Galloway *et al.* [91] demonstrated the potential of tandem electron and optical beam induced current measurements for the investigation of GB activity. Several experiments were performed using the SOM setup described above and EBIC apparatus using an SEM where the carrier injection densities of both electron and optical beams were varied. Majority carrier distributions in the CdTe were inferred from these measurements as well as increased hole concentrations at GB's, which was proposed to be consistent with minority carrier repulsion at grain boundaries, indicating that GB's were effectively passivated. Interestingly, this is in contrast to theories proposed by Smith *et al* [58], Visoly-Fisher *et al.* [59] and Woods *et al.* where a barrier to majority carrier transport at GB's has been proposed (as illustrated in Figure 2.2). In either case, these theories share the common theme that GB's enhance charge separation and contribute positively to overall cell performance.

Edwards *et al.* [92] continued this research, using modified SEM equipment to produce variable beam voltage EBIC and cathodoluminescence (CL) measurements. The injection dependent EBIC results indicated that (a) the $CdCl_2$ treatment was critical for GB passivation, leading to increases in minority carrier diffusion length, effectively broadening the depletion width, and (b) that the CdS window layer was effectively increasing the carrier concentration in the CdTe layer. Spatially resolved CL measurements were found to produce very complex results where it was postulated that the number and type of recombination centres varied as a function of distance from the CdS/CdTe interface.

Further studies of tandem EBIC and ion beam induced current (IBIC) measurements on CdTe thin films have also been reported. Baier *et al.* [93] described the use of EBIC and IBIC for the probing of surface and bulk transport properties, respectively, in polycrystalline CdTe. These were considered complimentary techniques due to the penetration characteristics of each incident beam type.

A significant resolution constraining factor in OBIC measurements is the diffraction limit. To overcome this limit the use of near-field SOM (NSOM) has been successfully demonstrated to produce NSOM-OBIC measurements. Reported by Smith *et al.* [58, 94], this technique achieved 50 to 100 nm resolution at $\lambda = 635$ nm using scanning probe microscopy (SPM) based technology. The approach required that the superstrate device structure was illuminated from the back-side (in contrast to standard operation) as illustrated in Figure 2.5(a) below.

Although necessary to ensure optimum resolution, this measurement geometry was in contrast to that found in typical OBIC experiments where the optical beam is directed through the front-side of the cell, as shown in Figure 2.5(b). This latter approach provides irradiance conditions analogous to standard operating conditions. Notwithstanding, the illumination geometry was assumed not to impact the key focus of the investigation: photoresponse at GB's. The observation of enhanced photoresponse at GB's was seen to corroborate other SPM measurements where band-bending at CdTe GB's was predicted to facilitate charge separation as illustrated in Figure 2.2.

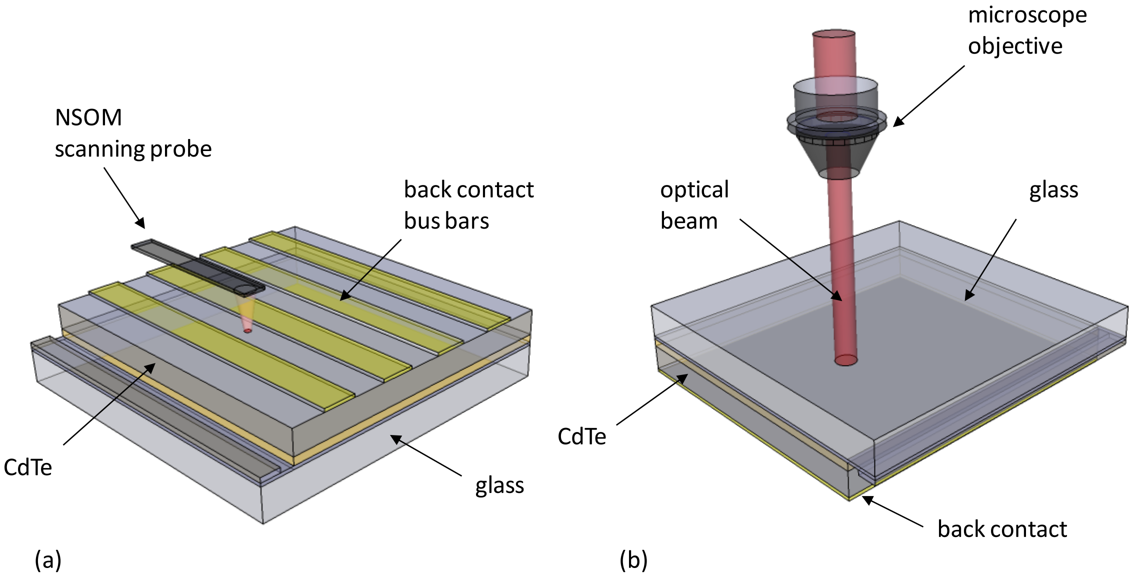

Figure 2.5 (a). NSOM setup and (b) Typical OBIC experimental setup, both on superstrate configuration CdS/CdTe solar cells

A similar approach was also used by McDaniel *et al.* [95] to examine $CuInGaSe_2$ solar cells in substrate configuration, subsequently, and in contrast to Smith *et al.* [58, 94] the geometry and irradiance conditions used in this investigation were both very similar to the devices standard operating conditions. Tapered optical fibres with diameters ranging from 64-140 nm provided sub-micron resolution while a 670 nm laser was used to induce the local photocurrent. Both surface and cross-sectional results were recorded; these showed reduced photoresponse at small grains (< 1 μm) and identified local junction width and depth properties.

Finally, Hiltner *et al.* [96, 97] and Sites *et al.* [98] reported the investigation of spatial variations in collection efficiency in CdTe and $Cu(In_{1-x}Ga_x)Se_2$ based devices. In contrast to other cited examples which typically used HeNe or Kr^+ lasers or monochromated light sources, this system used a series of fibre coupled diode lasers. This was found to be advantageous for several reasons:

1. Reduced cost
2. Increased flexibility
3. Superior beam characteristics

635, 685, 780, 830 and 850 nm lasers were chosen to match the spectral response of the cells under investigation. A maximum resolution of 1 μm at power equivalence of 1 sun was reported. This was dependent on the $1/e^2$ width of the incident beam and the step resolution of the translation stage, typically set to $(1/e^2)/2$. This laser beam induced current apparatus was able to spatially isolate variations in series resistivity, R_s in CdTe, furthermore showing that localised bandgap variations indicated that R_s variations were intricately related to S alloying. Further studies demonstrated the effects of $CdCl_2$ treatments and elevated temperature stress in CdTe solar cells, where increased collection uniformity was observed for $CdCl_2$ treated cells and regions of increased localized resistivity were observed in cells that had been subjected to temperature stress. The latter was suggested to be dependent on the non-uniform penetration of $CdCl_2$ and other contaminants from the back surface into the CdTe absorber, leading to increased alloying and poor material quality.

2.6 Scanning probe microscopy

Scanning probe microscopy (SPM) has been widely reported in the spatially resolved study of semiconductors. This section will focus on two specific SPM based derivatives; scanning Kelvin probe microscopy (SKPM) and conductive atomic force microscopy (CAFM). Furthermore this section will primarily focus on the application of these techniques to PV device and materials characterisation.

2.6.1 Scanning Kelvin probe microscopy (SKPM)

SKPM was first reported by Nonnenmacher *et al.* [99] in 1991. Taking the vibrating capacitor method, also known as the Kelvin method, this paper demonstrated the simultaneous high resolution (< 50 nm) imaging of surface topography and contact potential difference (CPD). CPD = $\Phi_1 - \Phi_2$, where Φ_1 and Φ_2 were the work functions of two closely spaced conductors: one being the probe tip, the second being the material under investigation. This was a nullifying technique, where a voltage was applied between the two conductors until the space in-between was field free and the measured current was zero. This nullifying signal was used to generate the CPD images. This report detailed the spatially resolved CPD measurement of several metal films including Au on Au, Pt on Au and Pd on Au. The probe tips used were Au-coated Si or Ni-Cr. Quantitative interpretation and extraction of Φ values from these results was found to be challenging due to the ambient environment the measurements were carried out in and consequent surface adsorption and contamination effects. Ultra high vacuum (UHV) conditions were proposed to potentially narrow the broad range of calculated Φ values.

SKPM has subsequently been demonstrated in the investigation of a variety of PV and non-PV materials; including single crystal Si [100], microcrystalline Si [101], $CuGaSe_2$ [102], CdTe [103] and GaN [104]. Simpkins *et al.* [105, 106] reported the characterisation of GaN (0001) using the SKPM technique. Results revealed the dependence of surface electronic structure on GaN film thickness, where surface potential variations were associated with threading dislocations present at the GaN surface and the dislocation density (and background donor concentration) was observed to decrease with increasing film thickness. Further SKPM measurements were complimented by conductive atomic force microscopy (CAFM) measurements [106] to reveal further defect structures in GaN, where surface potential variations related to negatively charged threading dislocations were correlated to localised current leakage paths. This study expanded on initial SKPM work to include edge and screw dislocation contributions to overall electrical behaviour. The tandem measurements were able to identify that pure edge and mixed dislocations were negatively charged and not highly conductive and screw type dislocations to be the source of localised leakage paths with no measurable charge.

Chevtchenko *et al.* further reported using the SKPM technique to investigate GaN [104] and ZnO [107]. The surface band bending of undoped *a*-plane GaN on *r*-plane sapphire was reported, where charged surface states were identified to cause upward surface band bending. Furthermore, a complimentary SKPM/CAFM approach was described in a comparative study of different ZnO surfaces. The results detailed the relative and absolute band-bending and the different surface reactivity's in the two samples examined.

Inevitably, high resolution SPM based electrical characterisation techniques have found significant interest amongst researchers interested in polycrystalline materials for PV applications. These spatially resolved techniques are capable of providing detailed information about the inherent compositional, structural and electrical non-uniformities found in these materials (though investigations have not been limited to polycrystalline materials).

Bhushan and Goldade [100] used the technique to study the surface potential change during the wear of single crystal Si (100) at ultralow loads, this investigation examined the effects of humidity and increasing wear cycles, where contaminant or natural oxide layers were increasingly removed. SKPM results showed that the surface potential changed under very specific humidity conditions as a function of increasing wear cycles.

Further studies on Si have been demonstrated by Breymesser *et al.* [101] and Jiang *et al.* [108]. Breymesser *et al.* [101] studied cross-sections of microcrystalline *p-i-n* Si solar cells. These "nanopotentiometric" measurements revealed a graded donor-like defect distribution and a constant boron compensation in the intrinsic layer, with the p-Si and n-TCO layers forming a reverse polarized diode in series with the *p-i-n* diode. These insights led the authors to investigate alternative layer stacking methodologies. Jiang *et al.* [108] used a similar approach to investigate the spatial distribution of electrical potential in cross-sections of *n-i-p* hydrogenated amorphous Si, (a-Si:H). These results provided detailed information on the device depletion width and carrier concentration, also isolating the *i/p* junction as the majority contributor to overall cell performance.

Studies investigating chalcopyrite materials have also been reported. Sadewasser *et al.* [102] elegantly demonstrated the Φ dependence on facet orientation in single grains of polycrystalline material, where subtle Φ differences between [102] and [111] oriented surfaces and more significant differences between [112] and [110] surfaces in *p*-$CuGaSe_2$ solar cells were readily identified. The authors were able to calculate the crystal orientation of the relevant facets from x-ray diffraction (XRD) measurements, where it was known that the [220] direction was perpendicular to the sample surface. These results provided convincing evidence that each crystal orientation led to a characteristic Φ value, a phenomenon attributed to the characteristic surface dipole found for each orientation. Sadewasser *et al.* [109] further demonstrated the SKPM technique in the study of $CuGaSe_2$ and $Cu(In,Ga)S_2$ GB's, where charged defect states at the GB interfaces were observed to cause downward band bending. This study also detailed surface photovoltage measurements, where a 685 nm laser was used to illuminate the sample. Under illumination, a decrease in band bending at GB's was observed, thereby reducing the carrier transport limiting potential barrier at the GB.

Jiang *et al.* [110] performed similar measurements to investigate GB's in $Cu(In,Ga)Se_2$ thin films. These studies detailed the effect of GB potentials on device conversion efficiency by varying the Ga content in the thin films. This was found to sharply impact GB potential, where Ga content in the 28 to 38 % range yielded drops in GB potential from ~ 150 mV to zero, it was observed that cell performance strongly correlated with this result, indicative of the positive role the GB potential was playing in overall cell performance. This finding supports many other cited examples where evidence detailing the positive effects of the GB network (once optimized) and its role in overall cell performance are reported.

The SKPM technique has also been successfully demonstrated in the study of CdTe solar cells. McCandless and Rykov [111] reported the analysis of cross-sectionally mounted CdTe cells. The (commonly used) two-pass interleave process was described by an algorithm where:

1. the probe tip measured the surface topography in tapping mode, followed by
2. the tip ascending to a predetermined lift height above the sample surface, and finally
3. the tip following the recorded XZ surface topography at the set lift height whilst any fluctuation in surface potential was nullified by applying a dc-bias, V_{dc}.

This nullifying signal was used to generate the surface potential image of the mapped surface. The difficulties in interpreting the V_{dc} signal were also discussed, where a number of factors can lead to complications:

1. Surface band bending caused by the surface states and charges
2. The surface Φ differing from the bulk Φ
3. The Schottky effect of the metallic (Co/Cr coated) tip and CdTe surface interface.

These factors were seen to potentially hinder absolute Φ measurements, but to be less critical for relative potential measurements (such as those presented and discussed in [111]). The spatial distribution of the potential was found not to correlate with surface topography, indicating that the primary junction was responsible for the observed localized variations in potential. These results further showed that the primary junction was located entirely within the CdTe film, extending through about half the film. Also identified was a small potential barrier (~ 100 mV) between the CdTe back surface and the back contact.

Visoly-Fisher *et al.* [112] further demonstrated the applicability of the technique in the study of CdTe cells. This study combined two AFM-based electrical characterisation techniques: scanning capacitance microscopy (SCM) and SKPM. In SCM an ac-bias is applied to the sample while the tip is grounded. The capacitance caused by the ac bias provides information on the surface depletion layer in p-type materials. The characterisation of single GB's and single grain surfaces was achieved using the combined SCM/SKPM technique. Results indicated that a hole transport barrier existed at the GB's, where the barrier height was expected to affect intergrain hole photocurrent transport. This observation was directly compared to those made by Sadewasser *et al* [109] where hole depletion at GB's was observed in $CuInSe_2$ and $Cu(In,Ga)S_2$ (as discussed above).

Further cross-sectional analysis of CdTe devices using the same complimentary techniques have also been demonstrated by Visoly-Fisher *et al.* [103]. This study compared two device structures taken from different sources and found that the electrical and metallurgical junction coincided, this was in contrast to McCandless and Rykov [111] who described a homojunction in similar CdTe devices. The origin of this disagreement may lie in subtle differences in the device structures studied, where Visoly-Fisher *et al.* [103] studied devices that incorporated highly resistive SnO_2 layers and conversely McCandless and Rykov [111] studied devices that did not. Alternatively, this discrepancy may have been caused by different sample preparation techniques. Visoly-Fisher *et al.* [103] describes a crude sample fracturing process and no further sample preparation, this was claimed to eliminate extraneous surface defects that might affect the electronic properties. In contrast McCandless and Rykov [111] described a complex sample preparation procedure, involving the mounting of a fractured sample at ~ 60° in an epoxy puck. Once cured, the cross section was exposed by multiple grinding and polishing steps using SiC paper and diamond and alumina slurries.

Moutinho *et al.* [113] further discussed the influence of sample preparation for SKPM (and electron backscatter diffraction (EBSD)) measurements. This study detailed the preparation of CdTe/CdS cross-sections for both SKPM and EBSD. It was found that a combination of chemical (Br in MeOH solution) and mechanical (diamond lapping films with various grits) polishing procedures, combined with ion beam milling, yielded optimum surface conditions for EBSD measurements but were more challenging for SKPM measurements. Samples were sandwiched between two glass slides using epoxy resin to avoid the 'rounding' of the film. EBSD results revealed columnar CdTe grains which nucleate in small grains in the first stages of growth. Successful cross-sectional SKPM results revealed important aspects of the junction including layer intermixing and the pn junction location.

As presented and discussed so far, spatially resolved SPM based electrical measurements are often combined, as demonstrated in some of these examples. This complimentary approach is also found in the application of CAFM and will be discussed further in the section 2.6.2.

2.6.2 Conductive atomic force microscopy (CAFM)

CAFM measurements have been widely reported in the investigation of both PV and non-PV devices and materials. The inherent non-uniformity commonly found in many semiconducting materials have made this an attractive characterisation tool, able to detail current transport pathways, GB affects and inter- and intra- grain conductivity variations in polycrystalline materials. The application to a variety of different materials including organic and inorganic photovoltaic materials has been successfully demonstrated.

Dominget *et al.* [114] and Troyon and Smaali [115] have both reported investigations where CAFM has been used for the electrical characterisation of non-PV materials. Dominget *et al.* [114] used the technique to measure the impact of chemical mechanical polishing on surface leakage currents in several copper structures. The technique enabled the authors to identify high surface leakage current levels in samples that had undergone short polishing times and lower leakage currents after increased polishing times. Thus, optimization of this processing stage was effectively achieved. Furthermore, Troyon and Smaali [115] presented a novel approach where an AFM instrument was placed within an SEM. This effectively combined the CAFM and EBIC techniques and was used to investigate the influence of electron irradiation on the electronic transport mechanisms during conductive AFM imaging of InAs/GaAs quantum dots [QD's] capped with a thin GaAs layer. This process involved irradiating the sample surface with a field emission gun and collecting the electron beam induced current via the AFM probe tip. Two main findings were described:

1. High charge retention times in InAs/InP, indicating a potentially exploitable memory effect.
2. The contrasting conduction mechanisms observed for the two probe tips used during the measurements; a Co/Cr coated tip where electron conduction was observed and diamond coated tips where hole conduction was observed.

This combined EBIC/CAFM technique provided unparalleled resolution and bore similarities to a study reported by Mates *et al.* [116] who described the complimentary (but separate) use of both CAFM and transmission electron microscopy (TEM) for the study of Si solar cells.

Mates *et al.* [116] described the detailed study of low-temperature mixed-phase microcrystalline Si (μc-Si:H) and amorphous Si (a-Si:H) where initial AFM surface topography imaging revealed isolated microcrystalline grains of similar diameter embedded in an amorphous phase. This was complimented by cross-sectional TEM imaging which indicated that the amorphous phase had a columnar structure (close to the surface) and that the μc-Si:H grains had (a) an approximately 100 nm growth "incubation layer" and (b) a conical type shape. These topographic features were examined using CAFM and revealed changes in a-Si:H conductivity with proximity to μc-Si:H grains. This provided evidence suggesting that hydrogen-rich column boundaries were acting as potential barriers for the electronic transport and led Mates *et al.* to draw correlations with GB behaviour in μc-Si:H solar cells.

Researchers working on organic PV solar cells have also showed significant interest in the CAFM technique where several reports have been published. Ginger *et al.* [117, 118] reported a novel photoconductive AFM (pCAFM) technique to map photocurrent distributions in polymer/fullerene organic PV solar cells. This was achieved by aligning an AFM probe tip at the centre of a diffraction limited laser spot, as illustrated in Figure 2.6.

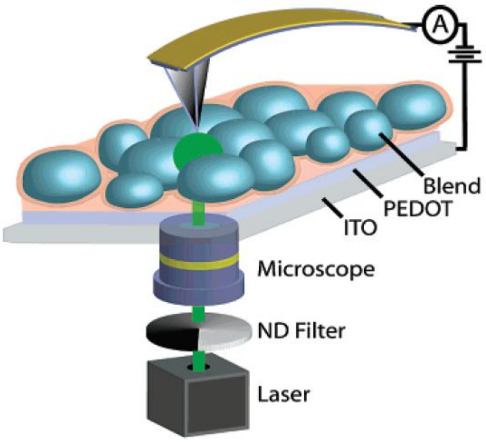

Figure 2.6. Schematic showing laser focussed through the transparent electrode onto the PV blend film as used by Ginger *et al.* (image courtesy of Ginger *et al.*)

This approach could be described as an optical equivalent to the EBIC/CAFM study presented by Troyon and Smaali [115]; an OBIC/CAFM technique. Reporting ~ 20 nm resolution, results showed that local photocurrents correlated well with device performance. Multiple sources of performance heterogeneity were proposed, these were related to lateral variations in both the film structure and the TCO. The results showed that device performance could be improved by obtaining greater control and regularity of the film morphology and that buried interfaces needed to be more fully understood.

Similar studies detailing functional polymer systems for organic PV were reported by Alexeev and Loos [119]. In contrast to Ginger *at al.* [117, 118] it was found that measurements carried out under ambient conditions were subject to chemical degradation and tip/ surface interface interference caused by an adsorbed water layer. Better success was found when measurements were carried out in an inert atmosphere. Alexeev and Loos commented that the CAFM technique operating under a range of applied bias' (between tip and TCO) provided reliable information on the spatial distribution and relationship between charge collection and domain interfaces, where mixed phase interfaces were proposed to enhance charge mobility.

$CuInSe_2$ and $Cu(In,Ga)Se_2$ polycrystalline thin films have also been studied using the CAFM technique. Azulay *et al.* [65] performed several measurements under varying applied bias', observing that PV and dark currents at bias voltages of < 1V mainly flowed through the GB's. Beyond a forward bias of 1V, photocurrent was observed to flow through the grain interiors. Interpretation of these results, yielded a proposal that a 'potential landscape' existed which resembled the band bending presented in Figure 2.2, though differing to the extent that electrons were considered the dominant carriers at the GB's, leading to the conduction band offset at the GB being reduced compared to the valance band offset. Azulay uses this evidence to draw comparisons with Smith *et al.* [58] and Visoly-Fisher *et al.* [59] indicating that charge separation, and resultant preferred current pathways are induced at GB's in a mechanism similar, but subtly different to that described for CdTe based devices, where less band bending at the GB is observed.

CdTe has also been at the focus of several CAFM studies. Visoly-Fisher *et al.* [59, 66] have extensively reported on the role of GB networks in polycrystalline CdTe, postulating that this inherent defect structure can constructively contribute to overall cell performance. In a model developed from earlier SCM and SKPM work, Visoly-Fisher *et al.* [112] describes GB depletion and a barrier to hole transport. This hypothesis is considered to corroborate CAFM measurements where a mechanism of charge carrier generation is proposed. Here, the AFM laser generates electron hole pairs which can be separated at the cells junction. If the cell is then connected in a circuit, via the TCO and the CAFM tip contacting the back surface (similar to that illustrated in Figure 2.6), the current can be extracted from the cell and measured. Two CdTe cells were studied one with and one without a $CdCl_2$ and anneal treatment. In $CdCl_2$ treated cells, low currents close to GB's but high currents at GB cores were observed, these high currents were suggested to be minority carrier currents flowing against the field direction. The increased band bending found at GB's [112] correlates with these results where electrons are drawn into the GB core, leading to a decrease in measured current close to the GB. Visoly-Fisher *et al.* [59] conclude that the $CdCl_2$ treatment leads to a unique doping profile at the GB's which leads to localised type inversion. This hypothesis is consistent with high Cl concentrations in CdTe where n-type behaviour can be induced. The resultant complex band structure is responsible for the enhanced carrier separation and overall increase in device performance observed.

Visoly-Fisher *et al.* have also reported CAFM measurements under various applied bias conditions finding that the V_{oc} at GB's is lower than in bulk grains, this has been interpreted to further indicate GB depletion (increased band bending). Figure 2.7 (b) below illustrates the mechanism proposed by Visoly-Fisher *et al.* [66]. This model considers the positive GB contribution to overall cell performance, where the junction is represented as a combination of many diodes connected in parallel. The 'filled' diodes represent the main CdTe bulk grain

/CdS cell junction and the ‘empty’ diodes represent the additional CdTe GB/CdS junction diodes.

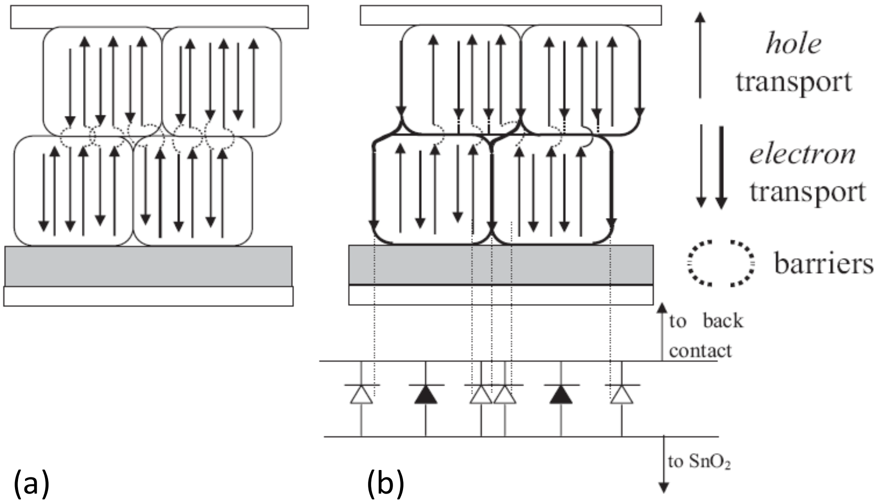

Figure 2.7. Schematic presentation showing (a) conventional charge separation and transport confined to the grain bulk and (b) mechanism proposed by Visoly-Fisher *et al.* showing additional charge separation at GB’s and electron transport along GB’s (image courtesy of Visoly-Fisher *et al.*)

CdTe based devices have been further investigated using the CAFM technique by Moutinho *et al.* [120-122]. These reports detail both surface and cross-sectional studies. Surface CAFM studies [121] reported the analysis of devices before and after $CdCl_2$ treatment, and further reported on the effects of two etching solutions: 1. Br in CH_3OH and 2. HNO_3/H_3PO_4 (NP) and discussed their contrasting effects on conductivity. In contrast to Visoly-Fisher *et al.* [59] it is proposed that the observed increases in current intensity in samples that had undergone a $CdCl_2$ treatment cannot unambiguously be attributed to the changes in the film itself. Instead, changes in the rectifying tip/surface contact are proposed, where distinguishing the contributions from the bulk sample and any measurement artefacts is challenging. This disagreement could be due to different sample preparation processes and measurement conditions (eg. Visoly-Fisher *et al.* [59] reported zero applied bias conditions whereas Moutinho *et al.* [121] reported measurements using forward bias’ of 7 and 8 V). The CAFM technique successfully revealed the contrasting effects of the two etch solutions. The Br in CH_3OH treatment showed to significantly increase GB conductivity. This was attributed to preferential etching and the formation of a Te rich layer at the GB’s. Conversely, the NP etch created a conductive layer over the whole CdTe surface, where an ohmic tip/surface contact was observed. This was in contrast to the untreated and Br in CH_3OH treated samples where a rectifying contact was observed.

Moutinho *et al.* also reported using the CAFM technique for the investigation of CdTe cross-sections [120]. This study examined the effects of several back contacting methodologies, including the deposition of Au/Cu and ZnTe:Cu layers and graphite pastes onto the CdTe back surface. In addition, the effects of the etch solutions discussed above were also investigated. Results revealed that Cu diffused into the material creating high-conductivity regions inside the CdTe film, a process which was enhanced by both etch solutions. Furthermore, the conductive regions were largely concentrated at the GB's, which, if extending toward the junction were observed to lead to short-circuits.

The role of Cu in CdTe/CdS solar cells was also reported by Moutinho *et al.* [122]. This work expanded the theory that described how the Cu back contact layer diffuses via the GB's into the CdTe by proposing a current transport model. In this model, photons absorbed in the CdTe were assumed to generate carriers close to the pn junction. In an absorber layer several microns thick, the increased conductivity of the GB's toward the CdTe back surface was proposed to enhance hole collection at the back contact. This optimization process is therefore confined to absorber layers with thicknesses between 6 and 8 μm, and would not provide any advantage in thin CdTe layers (where instead increased micro-shorts are likely to cause significant device degradation).

Increased hole transport at GB's is a proposal that is in contrast to Visoly-Fisher *et al.* [59] who propose a GB barrier to hole transport, therefore confining hole transport to the grain bulk. This inconsistency is likely due to subtle differences in the materials studied, where, for example, Cu diffusion is leading to unique grain and GB conductivity conditions. A unifying theory is not immediately obvious, though the sensitivity of the GB's to impurities and the subsequent band-bending observed further highlights the capacity of the CAFM to detect very subtle variations in electronic structure.

2.7 CdTe by metal organic chemical vapour deposition (MOCVD)

MOCVD is widely used in the compound semiconductor industry for the fabrication of electronic and optoelectronic materials. The first successful large scale (> 1cm^2) deposition of CdTe onto a CdS-coated SnO_2:F/glass substrate, operating at ~ 10 % conversion efficiency was reported by Chu *et al.* [123].

An all-in-one CdS/CdTe deposition process has also been successfully demonstrated by Berrigan *et al.* [124]. This novel approach highlighted the potential of the MOCVD technique to deposit both CdS and CdTe thin films sequentially, overcoming traditional process limitations where each layer was grown separately, and often by different techniques. Furthermore, Berrigan *et al.* [124] successfully produced p-CdTe by As doping; a process considered particularly challenging by Chu *et al.* [123], who reported that low-resistivity p-CdTe films could not be obtained. The growth characteristics of this process were measured using an *in situ* laser interferometry system [125] which provided detailed information on film thickness, growth rates, and roughening. Furthermore, this technique yielded a reflectance dependent roughening parameter, F_{rs} which Berrigan *et al.* correlated to device R_s; an important parameter in the fabrication of a solar cell.

This MOCVD process has been refined over the course of several studies [49]. These have included investigating different II/VI ratios by varying the organometallic precursor concentrations [126], developing an *in situ* $CdCl_2$ treatment process [62] and optimizing the As doping of the CdTe layer using secondary ion mass spectroscopy (SIMS) to quantify dopant incorporation [127]. Barrioz *et al.* [69] further reported using a highly As doped (1.5×10^{19} atoms cm^{-3}) back contact layer (~ 250 nm) to improve the back contact quality in CdTe devices. The inclusion of this layer eliminated any post-growth wet etching requirement, a common process prior to back contact metallisation. A further multi-variant Taguchi matrix based statistical methodology was used to determine critical CdTe/CdS growth variables for further investigation [128]. The role of the TCO in device performance has also been critically analysed, Irvine *et al.* [129] concluding that complex contributions from contact architecture, R_s and R_{sh} determined TCO suitability in MOCVD CdTe devices.

Efficient materials utilization is a parameter of key interest when considering the commercial viability of a large scale thin film manufacturing process. Therefore, the ability to readily control growth conditions in MOCVD makes it an attractive candidate for scalable manufacture. To this end, there is an ongoing ambition to fabricate devices with thicknesses determined only by absorption requirements (and not by processing limitations). The challenges involved have been detailed by Irvine *et al.* [130] where increased sensitivity to substrate contamination and shunting were both observed as CdTe layer thickness was decreased. Jones *et al.* [131] further reported the growth of “ultra-thin” CdTe solar cells where it was suggested that device performance was not only optically limited by the thinness of the absorber, but by junction characteristics and the proximity of the metallurgical junction to the back contact. Notwithstanding, devices with a 0.2 µm thick absorber layer were shown to successfully operate at ~ 3.5 % conversion efficiency.

3 Experimental

This chapter will principally describe the characterisation techniques used in this study. This will include the development and modification of existing laser beam induced current (LBIC) equipment and the use of a scanning probe microscope (SPM) for electrical characterisation. Furthermore, routine solar cell characterisation techniques, including current-voltage (I-V) and external quantum efficiency (EQE) measurements will be presented. As a preliminary introduction, the MOCVD process and cell fabrication will be described.

3.1 CdTe solar cell fabrication

MOCVD has been used (unless otherwise stated) for the deposition of all thin films described in this thesis. The first stage in cell fabrication involves a comprehensive cleaning process; a key preparative step which can determine surface morphology and film coverage. Careful insertion of the cleaned substrate into the deposition chamber follows. The sequential deposition of n-CdS, p-CdTe:As and $CdCl_2$ completes the fabrication of the window and absorber layers. Following an annealing and subsequent cooling step, the material is removed from the deposition chamber, rinsed with deionised (DI) water and inserted into a metal evaporator, where Au back contacts are thermally evaporated onto CdTe back surface. The final preparative step involves the partial removal of MOCVD deposited layers to expose the TCO and allow for electrical contact to the front electrode. This cell is now ready for characterisation.

3.1.1 Substrate preparation

The substrates used were either Sn-doped In_2O_3 (ITO) on boroaluminosilicate glass or F-doped SnO_2 (FTO) on soda lime glass commercially sourced from Delta Technologies Ltd and NSG Pilkington respectively. ITO on glass substrate preparation was as follows:

1. CH_3OH swab and N_2 dry
2. 15 minute ultrasonic DI water bath
3. CH_3OH rinse and N_2 dry

4. 15 minute ultrasonic bath in 2% decon90 surface decontaminant and 98% DI water.
5. CH_3OH rinse and N_2 dry.

A cleaning procedure as developed and advised by Pilkington was used to clean the FTO on glass substrates. This simply involved a nylon brush scrub using DI water. Following batch cleaning, multiple substrates were stored in a heated cabinet. Immediately prior to insertion of the substrate into the deposition chamber, a final CH_3OH swab and N_2 dry was carried out.

3.1.2 Metal organic chemical vapour deposition (MOCVD)

An all-in-one sequential process was carried out at atmospheric pressure (AP) to deposit n-CdS or n-$Cd_{1-x}Zn_xS$, As-doped CdTe and $CdCl_2$. In this process a carrier gas, H_2 was used to transport the selected organometallic precursors to a heated deposition chamber. A heated graphite susceptor was used to ensure uniform substrate heating. Figure 3.1 illustrates the process where a 240 nm CdS or $Cd_{1-x}Zn_xS$ window layer is initially deposited (archetypal for superstrate configuration solar cells). This is followed by a two-stage 2.25 µm As-doped CdTe growth [69, 127]. The As concentration in the bulk 2 µm of CdTe is approximately 1×10^{18} atoms cm^{-3}, this is followed by a 250 nm highly As-doped CdTe layer with As concentration ~ 1.5×10^{19} atoms cm^{-3}. A $CdCl_2$ activation treatment completes the MOCVD deposition process.

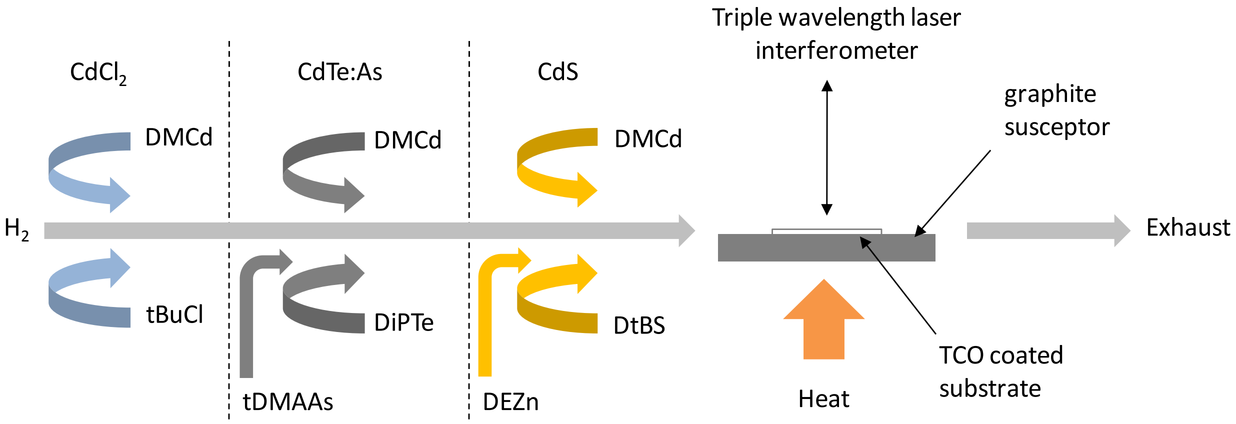

Figure 3.1. Schematic diagram of MOCVD experiments setup

Precursor flow was regulated using mass flow controllers (MFC's). Layer thickness was monitored in real-time *in situ* using a triple wavelength interferometer. This ensured that a reflectance signal was successfully obtained for each deposited layer. *In situ* measurement also provided real-time growth rates, allowing for the calculation of layer growth time. Table 3.1 summarises the typical growth temperatures, layer thicknesses and precursors used for each MOCVD deposited layer or treatment.

Layer/ *Treatment*	**Thin film**	**Growth temp (°C)**	**Thickness (nm)**	**Precursors**
Window	CdS ***or*** $Cd_{1-x}Zn_xS$	315	240	DMCd - dimethylcadmium - $Cd(CH_3)_2$ DtBS - ditertiarybutylsulphide - $(C_4H_9)_2S$ DEZn - diethylzinc - $Zn(C_2H_5)_2$ (DEZn)
		360	240	
Absorber	CdTe:As ***and*** $CdTe{:}As^+$	390	2000	DMCd - dimethylcadmium - $Cd(CH_3)_2$ DiPTe - diisopropyltelleride - $(C_3H_7)_2Te$ tDMAAs - tris(dimethylamino)arsine - $As(N(CH_3)_2)_3$
		390	250	
Activation	$CdCl_2$	200	-	DMCd - dimethylcadmium-$Cd(CH_3)_2$ tBuCl - tertiarybutylchloride - $(C_4H_9)Cl$
Anneal	-	420	-	-

Table 3.1. Summary of layers, growth temperatures, layer thicknesses and precursors

3.2 *Device processing*

Figure 3.2 follows the development of a CdTe solar cell beyond the main MOCVD growth process. Following the removal of the recently deposited material from the deposition chamber (1) excess $CdCl_2$ is removed by rinsing in DI water ($CdCl_2$ is a hygroscopic solid and hence readily soluble in water). This is followed by a N_2 blow dry. A lightening of the back surface after this rinsing stage is typically observed (2). The material is then carefully placed into a metal evaporator for back contact metallisation. An Edwards E306A coating system was used with a tungsten coil element. A 6 cm length of 0.2 mm diameter Au wire was then inserted into the coil. A 110×110×0.5 mm stainless steel (SS) mask was fixed at a constant height above the coil, where optimum film coverage has been found. The mask typically contained 16 5×5 mm^2 apertures, at 5 mm spacing but masks were also designed with 16 10×10 mm^2 apertures at 1 mm spacing. Furthermore, masks containing combinations of both apertures sizes were produced, with devices also being completed in this format. Evaporation was carried out at 4×10^{-5} mbar pressure at a source current of 40 A. This produced an array of 16 5 × 5 mm^2 contacts with ~80 nm thickness on the CdTe back surface (3).

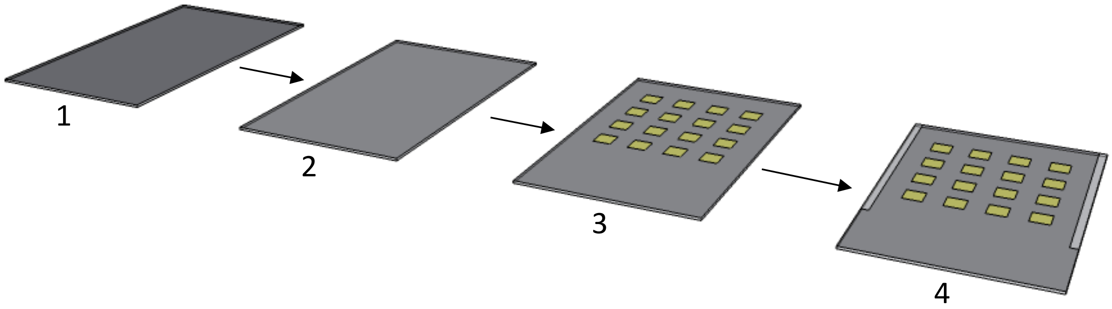

Figure 3.2. Development of cell post-MOCVD growth

To complete post growth processing, electrical contact to the front (TCO) electrode must be made. This step involves the removal of the MOCVD deposited layers to expose the TCO layer along two edge strips. This is achieved by scraping approximately 2 mm strips of the edge off the deposited layers using a sharp blade, to form two front contact bars along each side of the device. To ensure that CdTe particulates generated in this process can be safely captured, a droplet of DI water is placed on the hydrophobic CdTe surface prior to scraping; the released particulates are then safely contained within the droplet. Further DI water rinsing ensures a controlled environment is maintained and safe disposal of CdTe particulates is achieved. Device completion is accomplished by applying an In/Ga eutectic paste to the exposed TCO surface (4).

3.3 Current – voltage (I-V) measurements

Light and dark I-V measurements provide a convenient method to describe a solar cell's performance. The technique provides the following parameters: short circuit current (I_{sc}), open-circuit voltage (V_{oc}), fill factor (FF), and efficiency (η). These are extracted from the I-V curve, itself produced from a voltage bias sweep where the cell was contacted at both front and back electrodes.

An Abet Technologies Sun 2000 solar simulator was used as the light source in these measurements. This instrument was calibrated to AM 1.5 irradiance using a Fraunhofer ISE-calibrated mono-FZ-Si solar cell ensuring a constant power output over the active cell area. A Keithley 2400 source meter was used to (a) bias the cells through a range from – 1 V to + 1 V at 0.02 V resolution and (b) measure cell current at the applied bias'. A custom built sample platform allowed for routine measurements to be carried out at a constant height below the solar simulator lens, this apparatus also incorporated a fan to ensure a constant temperature (~ 25°C) was maintained throughout the measurement. The dark I-V curve was typically measured first, where the cell was covered to ensure no light exposure. Upon removal of the cover, the lamp was switched on and a light I-V curve was measured.

Custom software was used to control the bias sweeping and log both light and dark current data. This software also calculated the cells maximum power point (P_{max}) at V_{mp} and J_{mp} in addition to providing the parameters described above. Furthermore, the calculation of both series resistance (R_s) and shunt resistance (R_{sh}) values was achieved via the extraction of the reciprocal gradient from the light I-V curve in forward and reverse bias respectively. Solar cell performance can be limited by high R_s and/or low R_{sh}. Values of R_s of between 1 – 2 Ω cm^{-2} and R_{sh} = 1 – 2 kΩ cm^{-2} were typical, and considered to be experimentally acceptable results.

3.4 External quantum efficiency (EQE)

The external quantum efficiency of a cell is described by the ratio of the number of charge carriers generated by and collected from a solar cell to the total number of photons incident on that cell. This differs from internal quantum efficiency (IQE) measurements which describe a ratio dependent on charge carrier generation and *absorbed* photons by accounting for optical loses such as transmission and reflection.

EQE measurements were performed using a Bentham PVE300 Photovoltaic Characterisation System. This system used a dual light source where a Xe short arc lamp was used for wavelengths between 300 nm and 649 nm and quartz halogen lamp for wavelengths between 650 nm and 1800 nm. Wavelength dispersion was achieved using a Czerny-Turner triple diffraction grating monochromator. This provided monochromated light at 5 nm band width. Mirror based relay optics allowed the beam to be directed from the monochromator into the main instrument housing and be imaged at the sample plane. The monochromated output is synchronised with the detected (cell) signal via an optical chopper and lock-in amplifier. Absolute beam calibration was accomplished using a calibrated Si photodetector traceable to the Physikalisch-Technische Bundesanstalt (PTB), Germany. A temperature controlled vacuum mount secured samples at a constant temperature (25°C) throughout the measurement.

Typical EQE measurements were carried out between 300 and 1000 nm, this ensured that the full spectral range of the device including the band edges of both the window and absorber layers was captured. The beam image dimension could be adjusted by allocating different width slits at the exit of the monochromator. Slits were assigned to ensure the incident beam (once the sample was correctly aligned) was contained within the contact area. This was a critical consideration determining the validity of the results; if the beam was misaligned over the active cell region, a false spectral response reading would result.

3.5 Scanning electron microscope (SEM)

In scanning electron microscopy samples are imaged using a high energy electron beam. The beam is scanned across the surface in a raster pattern. The interaction of the incident electrons with the sample produces a characteristic signal which can be used to produce a topographic image. The primary electron beam is absorbed and scattered within a finite interaction volume, this produces (a) elastic (backscattered electrons (BSE)), (b) inelastic (secondary electrons) scattering and (c) electromagnetic radiation. Each can be detected by specialized detectors.

The Hitachi TM3000 instrument uses a high resolution BSE detector and dual accelerating voltages (5kV and 15 kV) to provide easy flexibility between imaging and analytical modes. Backscattered electrons can provide detailed information on both topography and composition. An accelerating voltage of 15 kV was typically selected for optimized resolution in topographical imaging mode. This allowed for a magnification range between 15 and 30,000 times, far beyond the confines of a typical optical microscope. Imaging resolution was approximately 30 nm, with > 1mm depth of field. Figure 3.3 illustrates the sample as mounted for (a) back surface analysis and (b) cross-sectional analysis. In the later measurement, cross sections were mounted onto a modified SEM stub, where a recess had been cut providing a slot into which a sample could be mounted perpendicularly.

A manual XY translation stage allowed for ± 17.5 mm movement on both axes. The z-height was fixed at an optimized sample – backscatter-electron detector distance. A fast pump-down diaphragm vacuum system allowed for quick and easy sample loading and exchange.

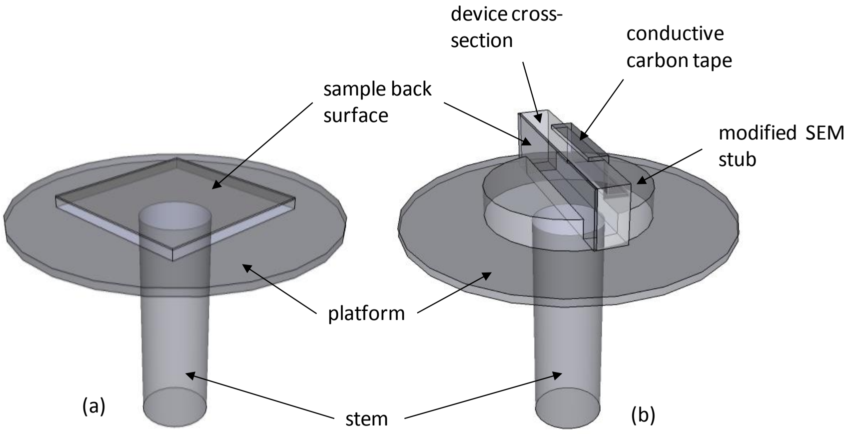

Figure 3.3. Stud arrangement for (a) back surface SEM analysis and (b) cross-sectional SEM

3.5.1 Energy-dispersive X-rays analysis (EDX)

This complimentary analytical technique provides information on the elemental composition of a sample. In contrast to SEM, in EDX mode, emitted X-rays are detected. These are representative of the atomic structure from which they originate. This elemental 'fingerprint' yields a spectrum which details a samples elemental composition. In EDX, the primary electron beam ionizes an inner shell electron from an atom close to the sample surface. This ionization event, creates an electron vacancy, which is filled by a high energy outer-shell electron, this transition leads to the emission of an X-ray photon. Figure 3.4 shows how the X-ray energy released is dependent on which shell the electron is transferring from and to. These characteristic x-rays are used to plot an EDX spectrum.

An Oxford Instruments Swift ED3000 X-ray microanalysis system designed for the Hitachi TM3000 was used for these measurements. This allowed for light element detection from boron upwards. Further to single point EDX spectra, the measurement of both EDX line scans and XY maps was also possible.

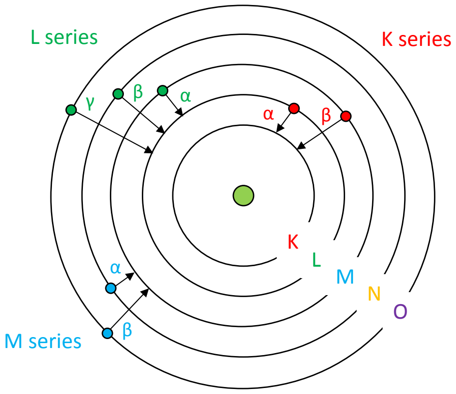

Figure 3.4. Diagram representing electron transitions in EDX spectroscopy

3.6 Profilometry

Profilometry was used to compliment *in-situ* interferometry measurements to determine film thickness. The *ex-situ* technique can also be used to quantify surface roughness and thin-film stress. A profilometer is a 2-dimensional contact method, where a stylus is scanned over a surface, and vertical displacement is sensitively measured as a function of the stylus' lateral position.

A Veeco Dektak 150 stylus profilometer was used for these measurements. This instrument provided a maximum 1mm Z-range over a maximum 55 mm single axis translation. The sample platform accommodated a maximum sample size of 150 mm. A 12.5 μm diameter stylus was used at a force of 5 mg. A 'hills and valleys' measurement was typically used to ensure that both positive and negative vertical displacement could be successfully recorded. The XY scan resolution was dependent on the scan length and scan duration. The Z vertical displacement resolution was 1 Å.

3.7 Laser beam induced current (LBIC) instrument

This section details the modifications and procedural optimization that was carried out as part of this project. Prior to its commencement, significant contributions to instrument construction and software programming were made by Vincent Barrioz and Rachael Rowlands-Jones [132]. This work continues from these early developments.

3.7.1 Instrument summary

As illustrated in Figure 3.5, the LBIC instrument uses a series of computer controlled systems to produce spatially resolved photocurrent measurements, these are primarily:

1. Laser trigger control
2. Device signal measurement
3. Translation stage control

The system operated using one of three fibre coupled lasers; a Power Technology Inc. (PTI) IQ series diode laser was used for measurements at 405 nm and PTI PPMT series diode lasers were used for the measurements at 658 nm and 810 nm. These successfully covered the spectral response region of a $Cd_{1-x}Zn_xS$/ CdTe solar cell. The lasers were powered by a dedicated DC power source and triggered by a computer controlled signal voltage via a Labjack U12 (a USB-based PC-real world interface), essentially a square wave signal synchronised to the device signal measurement and translation stage control.

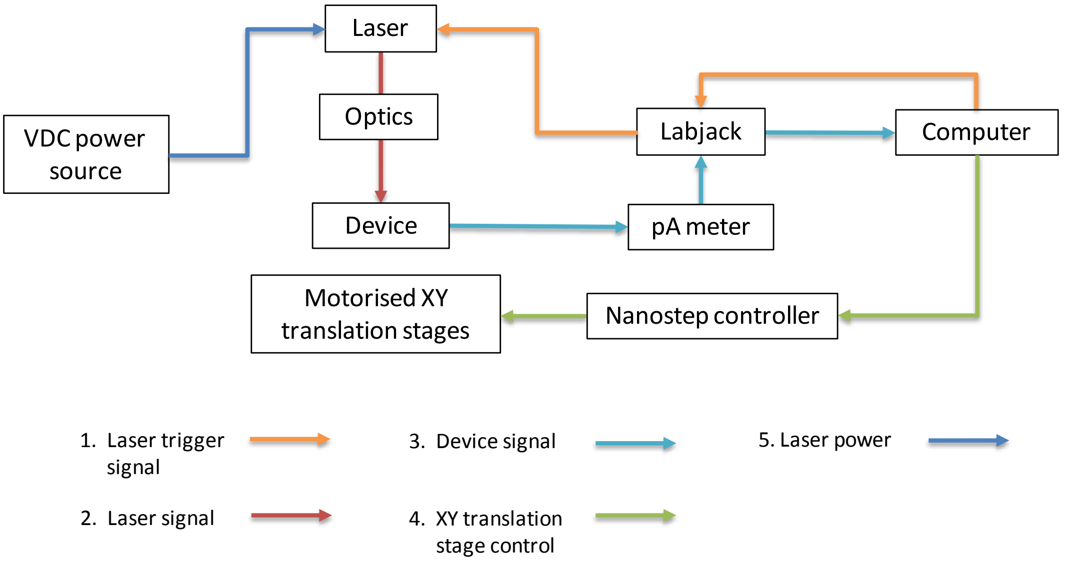

Figure 3.5. Schematic showing LBIC components and systems

This software controlled approach negated the requirement of a lock-in amplifier to synchronise LBIC signal recovery and translation stage, so simplified the apparatus without compromising the technique integrity.

As illustrated in Figure 3.6, the laser beam was relayed to the sample platform via a single mode (658 nm and 810 nm lasers) or a multi mode fibre (405 nm laser). The fibre coupling initially entered a collimating lens via a manual XY and tilt stage. This is followed by a beam splitter, which provided the option to monitor beam stability during the measurement, and finally an Olympus LUCPlanFl long-working distance dry objective lens, with numerical aperture (NA) 0.6 was used to focus the beam. The minimum theoretical beam widths using this objective were 0.3 µm for the 658 nm laser and 0.4 µm µm for the 810 nm laser [132].

A manual Z- translation stage allowed the sample to be moved into and out of focus; a key resolution determining parameter. This yielded the desired $1/e^2$ beam width, as calculated from ‘over-contact edge’ scans, where an abrupt junction between on and off contact regions provided an integral based on the distribution of the incident beam profile.

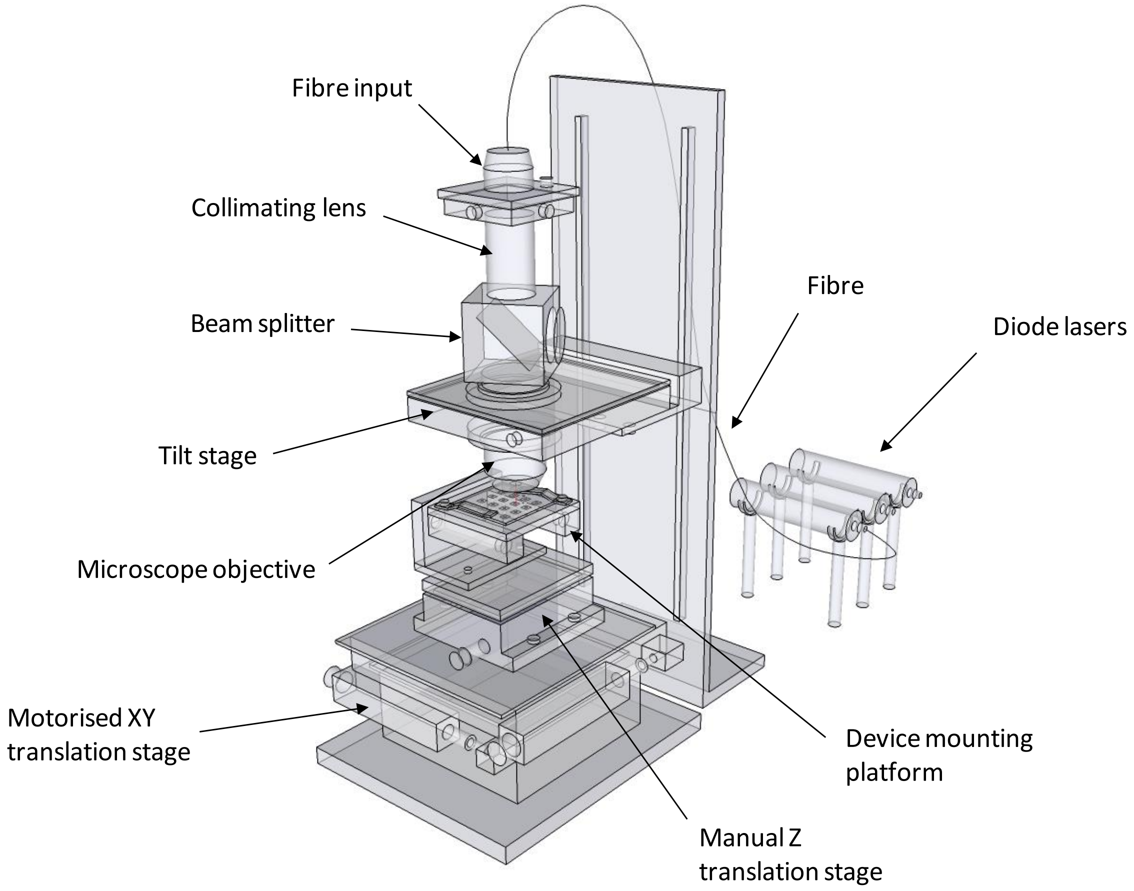

Figure 3.6. Illustration of LBIC instrument

XY translation was achieved using a computer-controlled Melles Griot motorised XY translation stage, this provided a minimum step resolution of 1 µm over a 25 mm range. Typically step resolution was set to one half the beam width to ensured good data point overlap.

Electrical contact was made via an array of conductive spring-loaded pins mounted into a Perspex base, an array of 18 pins allowed for good sample flexibility, and also to make multiple electrical contacts simultaneously. An HP 4140B pA meter was used to measure the device signal (the laser beam induced current) allowing for accurate signal recovery to 10^{-12} A (± 5 %). This signal was recorded by the custom written Visual Basic (VB) software via a Labjack U12.

During the course of this project several software and hardware additions and modifications were made to the instrument. These aimed to improve laser control, provide beam width and power calibration, and increase electrical contacting flexibility.

3.7.2 Hardware modifications

The following items of hardware were added to, or used in the calibration and operation of the LBIC instrument:

1. PTI IQ-series 405 nm diode laser
2. Orlin VTS-1 precision manual z-translation stage
3. Custom-built multi-contact device mounting platform
4. Ophir BeamStar FX 33-HD laser beam profiling camera
5. PTB-calibrated Si photodetector

The addition of a 405 nm diode laser broadened the spectral range of the LBIC system. Figure 3.7 highlights the wavelengths of each incident laser and its position relative to the spectral response of a typical $Cd_{1-x}Zn_xS$/ CdTe device. Prior to the incorporation of the 405 nm laser into the LBIC system, 658 nm and 810 nm lasers were used: these were both highly absorbing in the CdTe. Measurements made at these wavelengths were potentially able to identify defects in the CdTe absorber layer, the isolation of these defects within the device cross-section will be discussed in further detail in section 3.7.6.

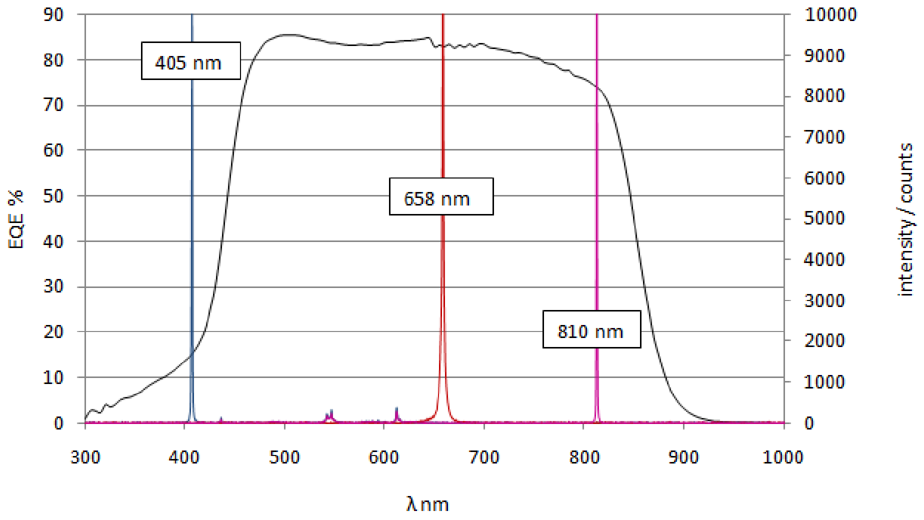

Figure 3.7. Laser wavelengths superimposed onto an EQE spectrum of a $Cd_{1-x}Zn_xS$/ CdTe device

The 405 nm laser provided a carrier excitation wavelength that, as shown in Figure 3.7 was marginally outside the $Cd_{1-x}Zn_xS$ absorption edge and therefore outside the spectral response of the cell. This yielded a measurement that was very sensitive to window layer absorption and transmission, and could be used to spatially identify defects in the window layer material.

A manual z-translation stage was also incorporated in the setup. Z-axis adjustment effectively determined the measurement resolution by allowing the sample to be moved relative to the focal point of the incident beam. This determined the beam spot size. Z-height adjustment prior to the installation of this component was achieved only via the fitting or removal of shims, these were placed on the vertical section of the sample mounting platform (indicated by a red arrow in Figure 3.8), thus affording discreet incremental translation on the z-axis. This approach restricted z-translation resolution to the thickness of the installed shim, and required significant disruption to the instrument mounting to achieve z-height translation. The manual z-translation stage therefore provided increased z-height resolution via micrometer adjustment (10 μm /increment and 500 μm /full rotation) over a 7 mm range. Furthermore, this ensured minimal disruption to the device mounting platform, or any other component of the instrument.

The replacement of the existing device mounting platform reflected the evolution of PV devices within the research group. This evolution saw sample dimensions increasing from 25 × 17 mm^2 to 25 × 75 mm^2 where three 5 × 5 mm^2 Au contacts were evaporated onto the former and 16 (or 28) 5 × 5 mm^2 Au contacts were evaporated onto the latter. The incorporation of a new mounting platform therefore provided two notable advantages: an easy and flexible approach to mounting larger devices and the potential to make multiple electrical contacts simultaneously. The latter enabled LBIC mapping over multiple contact areas in a single data acquisition, or area scan. Prior to this, multiple contact mapping was only possible via the manual re-positioning and contacting of each individual contact area.

As shown in Figure 3.8, an array of 16 holes were arranged at 1 cm intervals, these corresponded to the evaporated back contact array found on a typical CdTe cell (Figure 3.2). Typically only a fraction of these were occupied by a contact pin simultaneously, due to the translation range limitation of the XY stage, but this arrangement ensured maximum flexibility for novel and unusual contacting architectures.

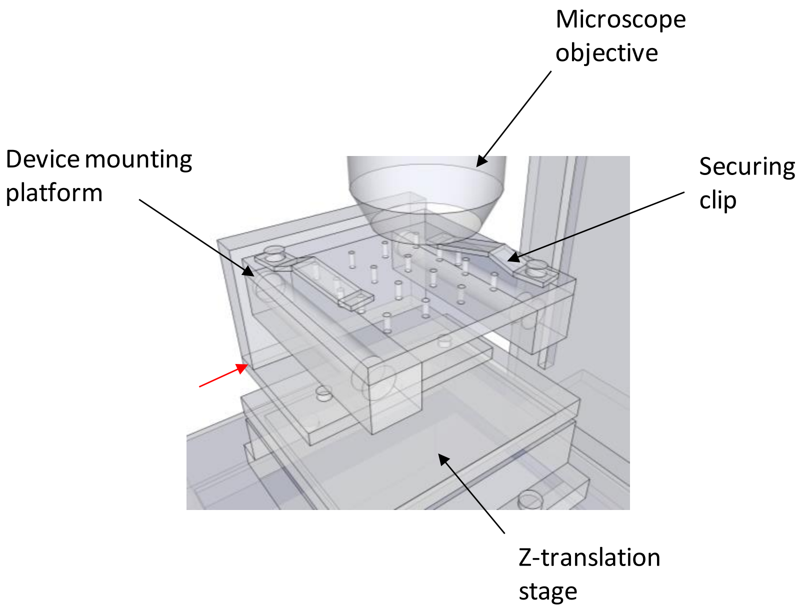

Figure 3.8. Multi contact device mounting platform

In addition to forming an electrical connection to the back contact, two further spring contact pins were aligned on the mounting platform to provide an electrical connection to the TCO front contact. Once correctly aligned, the device was secured using two spring clips, as highlighted in Figure 3.8.

An Ophir Beamstar FX33-HD laser beam profiling camera was used for initial beam characterisation. This was an *ex-situ* measurement, used only in the beam alignment phase prior to device mounting. This was due to the requirement of the camera to be placed directly where the mounting platform was ordinarily situated. The measurement software displayed the incident beam in 3D and 2D, as well as X and Y line profiles. Furthermore, some common width definitions were provided: D4σ, 90/10, $1/e^2$ and FWHM. The $1/e^2$ beam width was used in all beam approximations due to its significance in Gaussian beam profiles.

Absolute beam irradiance calibration was achieved using a PTB calibrated Si photodetector and HP 4140B pA meter. The known detector responsivity (A W^{-1} nm^{-1}) at each of the laser wavelengths allowed for accurate calculation of the beam power at a series of different laser currents, (I_{laser}) or trigger voltage settings. This calibration technique is presented in further detail in section 3.7.5.

3.7.3 *Laser control and modulation*

Laser control and trigger synchronisation to (a) the X and Y translation stages and (b) LBIC signal logging was achieved by modifying the existing software. Prior to modification, a function generator was used to produce a square-wave which operated the laser module. As a consequence, the laser control system operated independently to the signal logging and translation stage systems, and therefore modulation was not possible. To overcome this, the incorporation of the laser trigger control into the other software controlled systems was clearly desirable.

To this end, two additions were made to the VB software:

1. Basic laser operation (on/off), which provided easy laser operation during calibration and beam alignment stages, and
2. Full laser trigger integration and modulation with the translation stage and signal recovery systems. This ensured that the laser was switched synchronously with both the LBIC signal logging and the translation stage step motion. The Labjack U12 (already used to interface the pA meter output to the PC) provided an analogue signal voltage output (AO0) to the laser. AO0 could be varied via input to the VB software, depending on the required signal voltage.

3.7.4 *Beam width approximation*

LBIC measurement resolution is dependent on two interrelated parameters: (a) the step increment of the XY stage and (b) the incident beam width. To ensure that good data point overlap is achieved, the XY step increment is typically set to ½ the beam width. Therefore the beam width is the primary determinant of the XY step increment and thus the overall instrument resolution. Consequently, the careful measurement of the beam width at all stages of component installation and sample mounting is very important.

Two distinct beam measurement techniques were used. Initially, during instrument reconstruction, it was desirable to monitor the beam alignment using a beam profiling camera (as introduced in section 3.7.2). This instrument successfully ensured the *ex-situ* measurement of the beam width, and additionally provided real-time information on the 3 dimensional Gaussian distribution of the beam.

Figure 3.9 illustrates the Ophir Beamstar software display, showing the output of the 658 nm laser at the fibre end. The Gaussian shape of the beam prior to entering the instrument optics is clearly defined. Figure 3.9 (a) and (b) respectively show the 2D and 3D display, where manipulation of the X and Y axis' provide a single axis display: (c). Furthermore the numerical values were also displayed as shown in Figure 3.9 (d). This multi-output display made possible the rapid measurement of beam characteristics during the instrument construction stages. Although, due to the inherent *ex-situ* nature of the measurement, significant disruption to the instrument setup was required before a device could be mounted for the LBIC measurement.

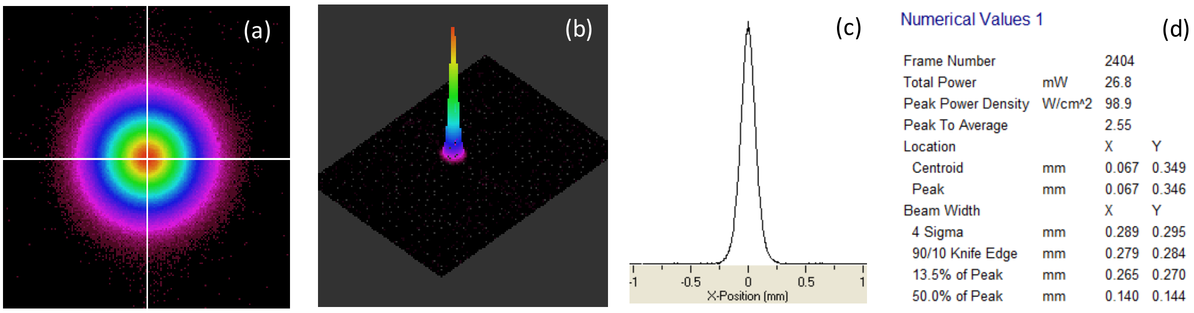

Numerical Values 1

Frame Number		2404	
Total Power	mW	26.8	
Peak Power Density	W/cm^2	98.9	
Peak To Average		2.55	
Location		X	Y
Centroid	mm	0.067	0.349
Peak	mm	0.067	0.346
Beam Width		X	Y
4 Sigma	mm	0.289	0.295
90/10 Knife Edge	mm	0.279	0.284
13.5% of Peak	mm	0.265	0.270
50.0% of Peak	mm	0.140	0.144

Figure 3.9(a) 2D (b) 3D (c) single axis and (d) numerical data output from Ophir Beamstar software, showing 658 nm laser beam at fibre end. NB. the displayed peak power density value is uncalibrated and therefore arbitrary.

An alternative *in-situ* method which would yield the $1/e^2$ beam width and hence the measurement resolution of the area scan was therefore required. An 'over-edge' line scan is commonly used for beam width measurements of this type. This necessitates that the beam is linearly translated between a photo active and a photo inactive area. The interface between these two regions must be abrupt, and often a knife-edge or similar is used. This provides an integral based on the marginal distribution of the incident beam to precisely extract the $1/e^2$ beam width. An alternative method can be used to achieve very similar ends: this approach makes use of the abrupt junction that can be produced by scribing around the perimeter of a back contact area. This successfully yields the abruptly defined and separated areas of photoactivity and inactivity required for the 'over-edge' line scan. This method therefore requires no additional components and can be carried out immediately prior to an area scan without disruption to the sample mounting.

Figure 3.10 shows four 'over-edge' line scans, recorded at different relative z-heights, (0, 100, 160 and 200 μm). The $1/e^2$ beam width, $W_{1/e2}$ was calculated using the following method:

1. An average off-contact value, a and an average on-contact value, b, were initially determined; this provided the total range, r.
2. The $1/e^2$ beam width is then determined by taking two points where the intensity falls to $1/e^2 = 0.135$ the maximum, using the over-edge technique this equates to two points, $L_a = a + 0.135r$ and $L_b = b - 0.135r$.
3. Calculation of the x-intercept at these upper and lower limits, yields L_{ax} and L_{bx}, where $W_{1/e2} = L_{bx} - L_{ax}$.

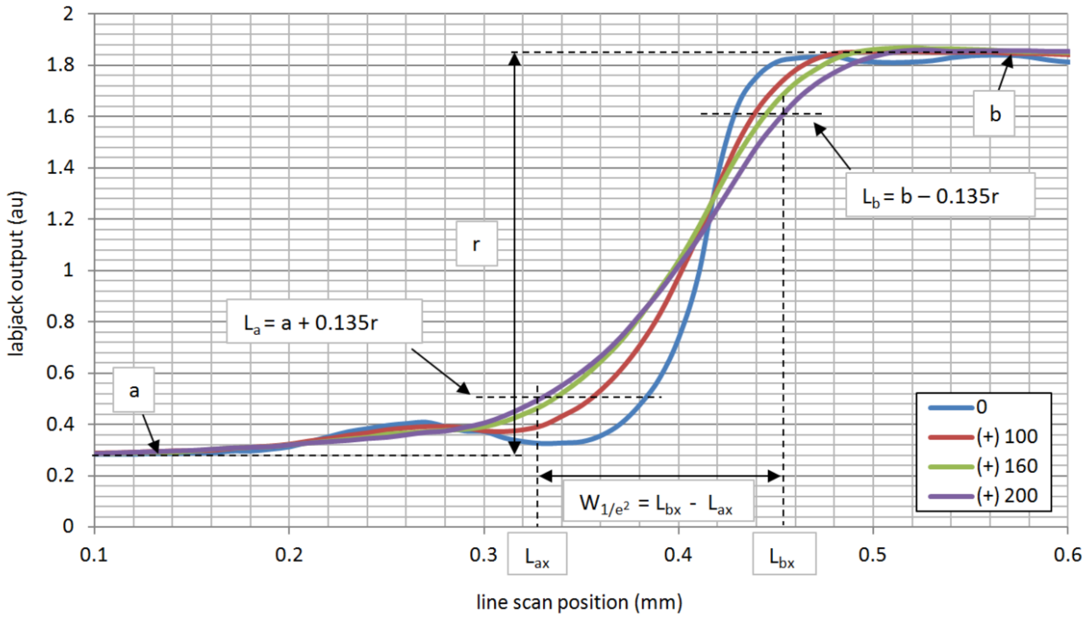

Figure 3.10. Plot showing the calculation of laser beam spot size using the 'over-edge line scan technique

A trial and error process can then be used to calculate the desired beam width. Figure 3.11 shows four calculated beam widths using the technique presented above, a linear relationship between z-height and beam width is clearly demonstrated. This approach therefore allows the extrapolation of any desired beam width by plotting only a few data points, followed by the correct adjustment of the manual z-translation stage.

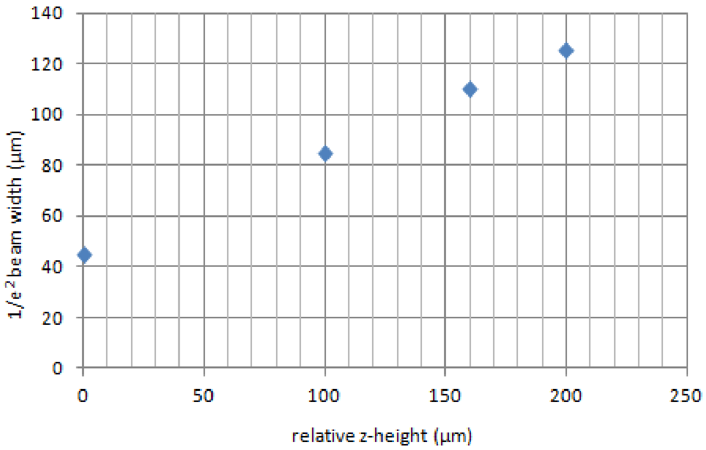

Figure 3.11. Trial and error beam width measurement at z-heights 0 to + 200 µm

Figure 3.12 below shows the beam width as a function of z-height over a 1.8 mm range. These values were recorded using the Ophir beam profiling camera, and therefore not subject to any scattering effects associated with the superstrate cell configuration. Notwithstanding, the beam width's linear dependence on z-height follows the same trend found in Figure 3.11.

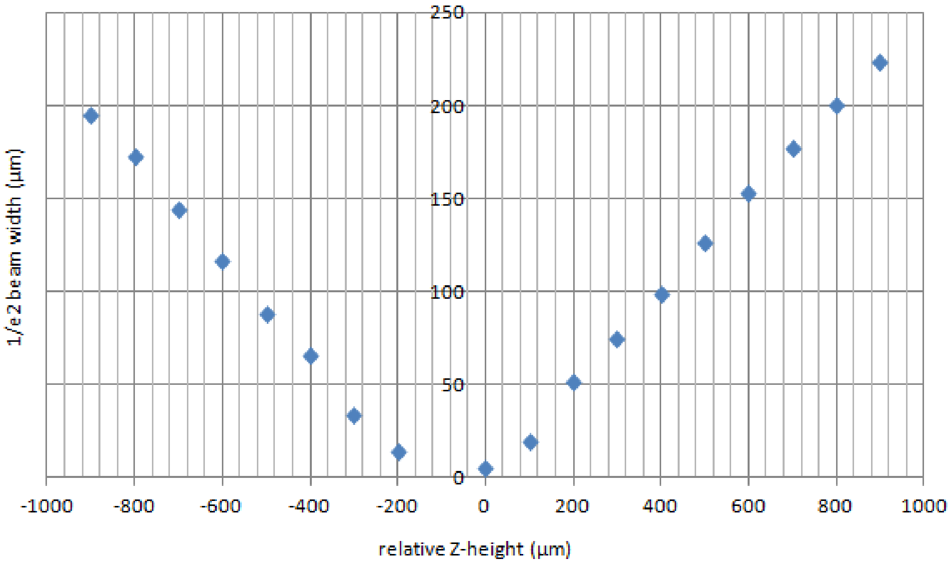

Figure 3.12. 658 nm beam width dependence over 1.8 mm z-height range

Furthermore, the beam profiling camera recorded a minimum beam width of 5 µm, (the camera's minimum measurable beam width). Although significantly higher than the theoretical minimum width of 0.3 µm (calculated by Rowlands-Jones [132]) this value represented the smallest *ex-situ* measured beam width. *In-situ* measurements using the technique described above achieved minimum beam widths of approximately 10 µm. Multiple contributions, including beam scattering and diffuse off-contact/on-contact boundary effects will all have contributed to limitations when attempting to set and measure specific $1/e^2$ beam widths.

3.7.5 *Irradiance calibration*

Irradiance calibration at each incident wavelength was achieved via a two stage process, involving the accurate measurement of:

1. The beam spot size area, A, via the calculation of the $1/e^2$ beam width.
2. The laser beam power, P_o (W).

The laser beam spot size is readily calculated from the $1/e^2$ beam width using the methods discussed in section 3.7.4. P_o was calculated using a calibrated Si photodetector. Detector responsivity, R at λ = 300 to 1000 nm is shown in Figure 3.13, the laser wavelengths and corresponding detector responsivity figures are labelled.

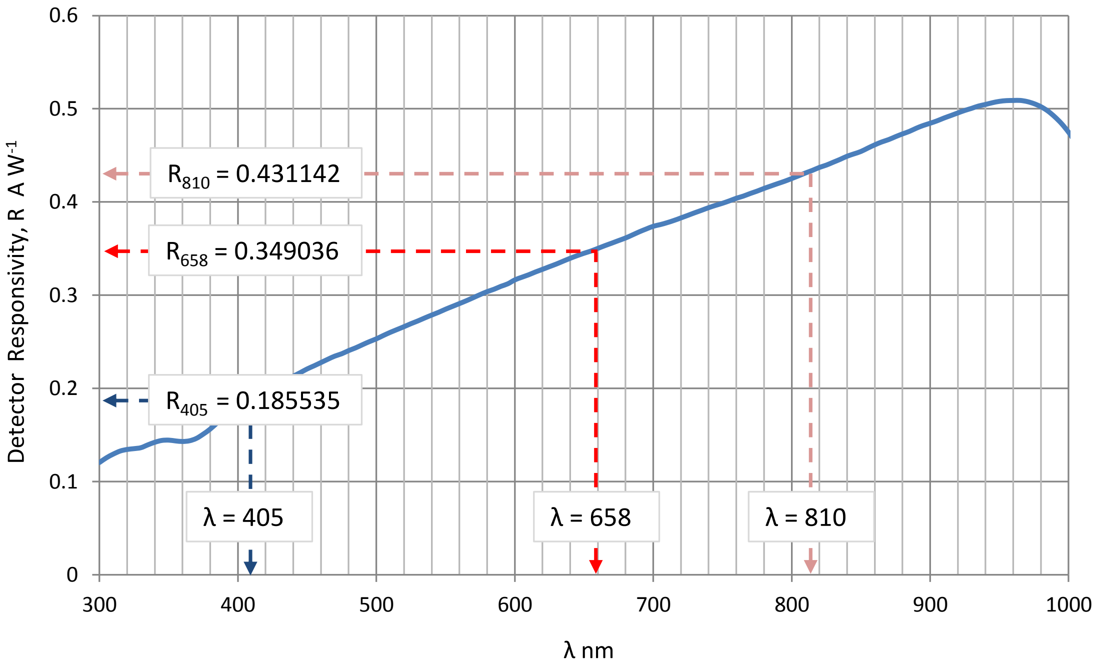

Figure 3.13. Si photodetector responsivity curve

The Si detector current signal, ($I_{detector}$) was measured using an HP 4140B pA meter. The laser power, P_o could be readily tuned via the adjustment of the trigger signal voltage (405 nm laser) or I_{laser} (658 and 810 nm lasers). This provided the means to plot calibration curves over a broad power output range. The 405 nm laser operated over a trigger signal range between 0.3 and 1.1 V, where $I_{detector} = P_oR_{405}$. Conversely, for the 658 nm laser a range of 10 to 100 mA where $I_{detector} = P_oR_{658}$ was used, and for the 810 nm laser a range of 45 to 120 mA where $I_{detector} = P_oR_{810}$ was used. Figure 3.14 shows the calibration plots for the 3 diode lasers used, where P_o (W) is plotted against trigger voltage or laser current.

Adjustment of these plots to calculate power density over the P_o range at several beam widths was achieved by calculating the spot size area, as shown in Table 3.2. This yielded the calibrated beam power density, P_d where $P_d = P_o/A$. Figure 3.14 further shows the area-adjusted beam power density for four $1/e^2$ beam widths: 100, 50, 25 and 10 µm at each laser wavelength.

	$1/e^2$ beam width (µm)			
	100	**50**	**25**	**10**
Area, A (µm^2)	7854	1963	491	79

Table 3.2. Beam spot size areas for 100, 50, 25 and 10 µm $1/e^2$ beam widths

Figure 3.14 (a) shows that the 405 nm laser, with a peak output rating of 100 mW prior to optical hardware related attenuation and losses, operates between a range of 14.1 nW and 22.0 µW, dependent on the trigger signal voltage. Therefore, for a $1/e^2$ beam width of 100 µm, to achieve an equivalent irradiance of 100 mW cm^{-2}, or 1 sun, a trigger voltage of 0.7 V is required. Conversely, at a reduced $1/e^2$ beam width of 10 µm, a reduced trigger voltage of approximately 0.4 V achieves the same irradiance. Figure 3.14 (b) and (c) equivalently illustrate the laser current requirements to achieve similar irradiances at 658 nm and 810 nm respectively.

Furthermore, the accurate determination of P_o and $1/e^2$ beam widths enabled the calculation of the photon flux density, Φ for each laser, at any desired $1/e^2$ beam width, where $\Phi = P_d/E$ and $E = hc/\lambda$. Table 3.3 shows the equivalent photon flux (photons s^{-1} m^{-1}) per laser wavelength used and Table 3.4 shows the area dependent photon flux as dictated by the $1/e^2$ beam width. ($h = 6.63 \times 10^{-34}$ J.s and $c = 2.98 \times 10^{8}$ m s^{-1}).

Laser λ (nm)	**Energy (J)**	**Energy (eV)**	**Φ at 1 sun (photons s^{-1} m^{-1})**
405	4.90×10^{-19}	3.06	2.04×10^{21}
658	3.02×10^{-19}	1.88	3.31×10^{21}
810	2.45×10^{-19}	1.53	4.08×10^{21}

Table 3.3. Photon energies at each laser wavelength, λ and equivalent photon fluxes, Φ.

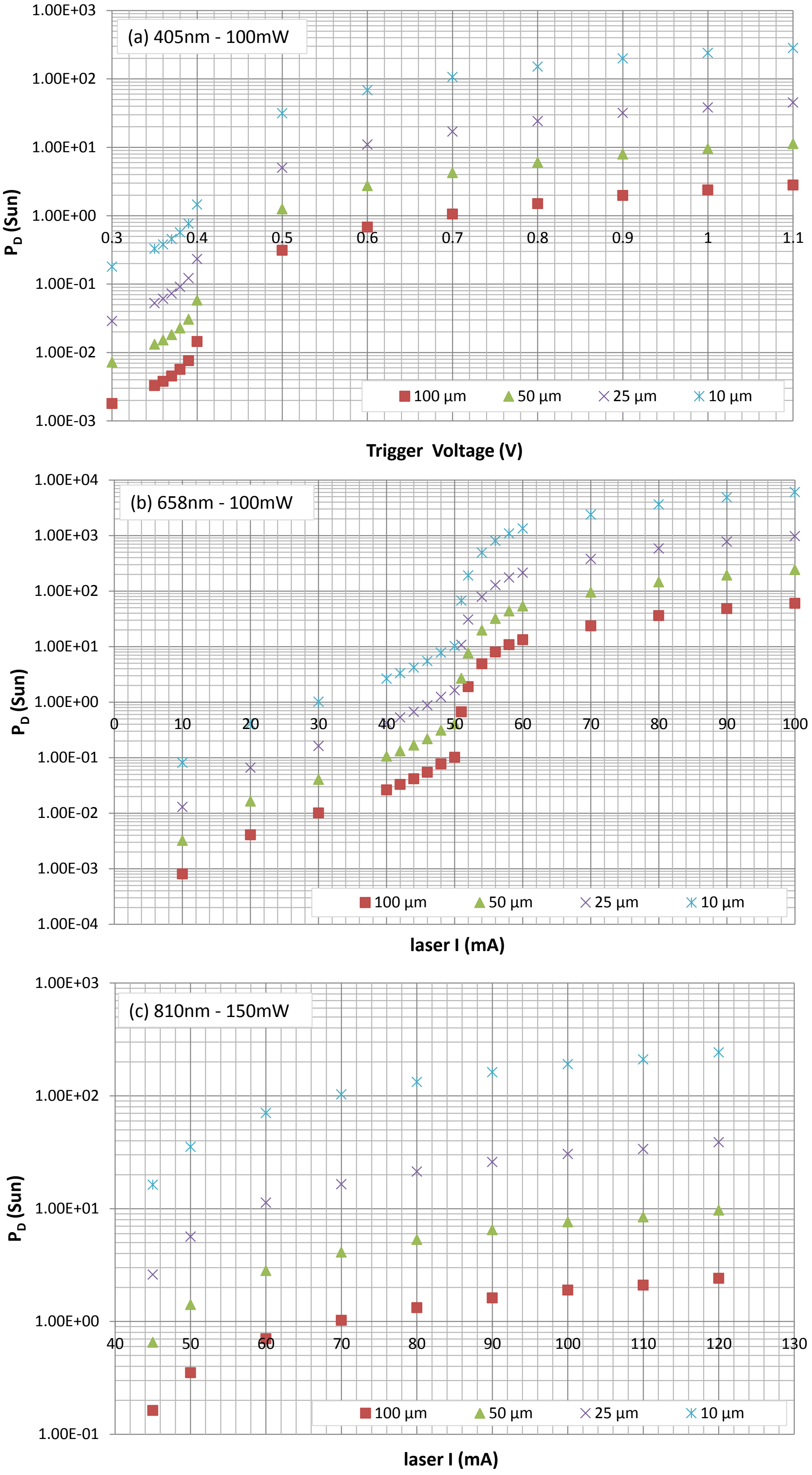

Figure 3.14. Absolute calibration curves for (a) 405 nm laser at 0.2 to 1.1 V trigger voltages, (b) 658 nm laser at laser current 10 to 100 mA and (c) 810 nm laser at 45 to 120 mA.

	Laser λ (nm)	**Beam area, A (μm^2) (assuming 1/e^2 beam width (μm))**			
		7854 (100)	**1963 (50)**	**491 (25)**	**79 (10)**
Φ at 1 sun (photons s^{-1} A^{-1} λ^{-1})	**405**	1.60×10^{13}	4.00×10^{12}	1.00×10^{12}	1.60×10^{11}
	658	2.60×10^{13}	6.50×10^{12}	1.63×10^{12}	2.60×10^{11}
	810	3.20×10^{13}	8.01×10^{12}	2.00×10^{12}	3.20×10^{11}

Table 3.4. Photon flux (# photons s^{-1} A^{-1}) for each labelled 1/e^2 beam width to achieve irradiance equivalence = 1 sun

The calibrated Si photodetector also provided a method whereby the photon energy dependent penetration depth δ_p, could be calculated.

3.7.6 Penetration depth calculation

The penetration depth, δ_p is defined as the depth within a material where the intensity of incident radiation, I falls to 1/e (~37 %) its original value, I_o. δ_p is described as 1/α where α is the photon-energy dependent absorption coefficient.

The Beer-Lambert law, $I = I_o\ e^{-\alpha d}$ describes the exponential decay of radiation inside a material, where d is the thickness of the absorbing layer (in the case of thin films). Thin films (where the intensity of the transmitted beam can be measured) can be used to calculate α and therefore δ_p, where $\alpha = -\ln (I/I_o)/d$.

Experimentally this was calculated using a series of standard samples to separate reflection, (R) and absorption, (A) losses due to the glass substrate and the TCO and window layers. Layer thicknesses were determined by *in-situ* interferometry during film growth, and confirmed by profilometry. Initially a measurement of the laser beam incident onto the Si photodetector yielded I_o. The following samples were then placed in the path of the incident laser beam:

1. Blank 25 x 50 x 0.7 mm^2 boroaluminosilicate glass, ($I_{glass} = I_o - R_{glass}$)
2. 5 – 15 Ω / □ ITO on glass, ($I_{ito} = I_o - R_{glass} - A_{ito}$)
3. 240 nm $Cd_{1-x}Zn_xS$ on 5 – 15 Ω / □ ITO on glass, ($I_{240nm\ CdZnS} = I_o - R_{glass} - A_{ito} - A_{240nm\ CdZnS}$)
4. 240 nm $Cd_{1-x}Zn_xS$/ 500 nm CdTe on 5 – 15 Ω ITO on above glass, ($I_{500\ nm\ CdTe} = I_o - R_{glass} - A_{ito} - A_{240nm\ CdZnS} - A_{500nm\ CdTe}$)

Crucially, this yielded $I_{240\text{ nm CdZnS}} = I_o - R_{glass} - A_{ito} - A_{240\text{nm CdZnS}}$, (sample #3) allowing CdTe-only absorption could be calculated, where the CdTe absorption coefficient, $\alpha = -\ln((I_{500\text{nm CdTe}}/ I_{240\text{nm CdZnS}})/d)$. Samples 1 and 2 also successfully highlighted the transmission losses related to the glass substrate and TCO.

Table 3.5 summarises the transmittance results, where increased short wavelength absorption is clearly seen in both $Cd_{1-x}Zn_xS$ and CdTe layers. $I_{240\text{nm CdZnS}}$ and $I_{500\text{nm CdTe}}$ were calculated from the transmittance through sample #3 and sample #4 respectively.

λ nm	**Sun**	**I_o %**	**I_{glass} %**	**I_{ito} %**	**$I_{240\text{nm CdZnS}}$ %**	**$I_{500\text{nm CdTe}}$ %**
405	1	100.00	97.48	84.91	14.21	4.6×10^{-3}
658	1	100.00	92.65	78.29	68.04	9.51
810	1	100.00	94.88	85.93	72.63	28.39

Table 3.5. Normalized transmittance measurements for calculation of absorption depth, δ_p

These values yielded both α for d = 2000 nm (the standard CdTe absorber thickness) and δ_p as illustrated in Figure 3.15 where incident wavelengths are overlaid onto a schematic of a $Cd_{1-x}Zn_xS$/ CdTe device. This shows the relative proximity of the wavelength dependent δ_p to the pn interface and CdTe back surface. The calculated α values are in broad agreement with established values for CdTe [133] where small discrepancies can be attributed to differences in thin film fabrication and measurement techniques. These results allowed the diagnostic analysis of subsequent LBIC maps taken over full CdTe devices, where the isolation of defect structures within the device cross-section was made possible – a hypothesis which will be discussed in further detail in Chapter 4.

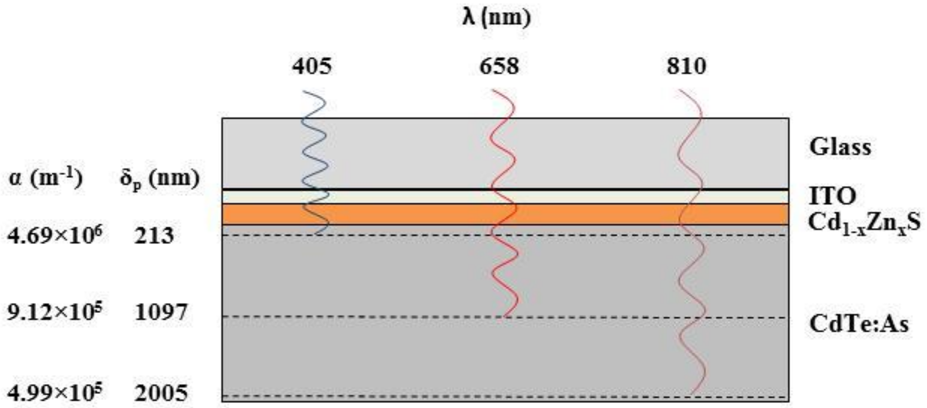

Figure 3.15. Schematic of CdTe device showing absorption coefficients, α and penetration depths, δ_p

3.8 Scanning probe techniques

The versatility of the scanning probe microscope (SPM) has proven to be an invaluable tool in the materials science community. Many derivatives based on this technology have been developed where the simultaneous acquisition of both topographic and electronic properties is made readily possible. Surface potential (SP) imaging, also known as scanning Kelvin probe microscopy (SKPM) and conductive probe atomic force microscopy (CAFM) demonstrate two AFM derived techniques which have been particularly applicable in the investigation of PV materials, as discussed in chapter 2.

Each AFM technique relies on the same basic principle where a sharp probe tip is scanned in a raster pattern across a samples' surface. The action of translating the tip in X and Y directions leads to Z-axis displacement. Accurate measurement of this displacement is facilitated by reflecting a laser beam off the probe cantilever onto a position sensitive photodetector (PSPD). This allows the instrument to be operated in one of two ways: the PSPD signal can be used to directly produce a spatially resolved topographic image of the surface, or, as is more commonly the case, the PSPD signal is used in a feedback loop to operate a Z-translation of the platform using a piezoelectric element. This nullifies the PSPD signal by using a reference signal, known as the setpoint. This feedback loop signal is used to generate the topographic image; a process which ensures high measurement precision and increased sensitivity to irregular surfaces.

An AFM instrument can be operated in a variety of modes, this project details the use of the following: TappingMode™, contact mode and non-contact mode. In TappingMode™ an oscillating probe tip lightly taps the surface whilst being rastered across a sample, the change in oscillation amplitude is used in the Z-feedback loop to produce a topographic image. TappingMode™ is a commonly used AFM mode which eliminates potentially detrimental lateral forces and demonstrates increased resilience towards any surface liquid layer – a common feature in an ambient imaging environment. TappingMode™ AFM is used in the first of two passes, known as interleave, used in SKPM measurements, TappingMode™ is used to produce the topographic image prior to the non-contact second pass to record the SP image.

In contact mode AFM, the probe is in perpetual contact with the sample surface. The probe cantilever must have a spring constant lower than the effective spring constant holding the atoms together. As the probe tip is rastered across a sample, the contact force causes the cantilever to bend to accommodate topographic changes. The non-contact mode, also known as LiftMode makes use of van der Waals interactions between a samples surface and a vibrating cantilever, this is achieved by applying an AC-signal correlating to the cantilevers resonant frequency. As the tip is rastered across a sample, the change in resonance frequency or vibration amplitude is used by the Z-feedback loop to adjust the Z-height and maintain a constant signal in response to the lateral changes. As in TappingMode™ AFM this feedback loop signal is used to generate a spatially resolved image.

3.8.1 Scanning probe tips

The selection of an appropriate probe tip is of critical importance when making preparations for either SKPM or CAFM measurements. For SKPM, the instrument manufacturer advises using Cobalt/ Chromium, (Co/Cr) or Platinum/ Iridium, (Pt/Ir) coated tips. A brief survey of the literature and with reference to Chapter 2 shows use of both coatings; Simpkins *et al.* [105, 106] reported using Co/Cr coated tips [105, 106] in the investigation of GaN, and alternatively Sadewasser *et al.* [102] reported using Pt/Ir coated tips for studying various chalcopyrite materials. Furthermore, Bhushan and Goldade [100] and Breymesser *et al.* [101] both reported SKPM studies on Si solar cells using doped diamond-coated silicon tips. This clearly demonstrates the individual requirements of different materials, and the necessity to tailor probe choice accordingly.

For CAFM, either a doped diamond-coated Si tip or Pt/Ir coated tip is suggested. Again, examples of both are found in the literature: Mates *et al.* [116] used a Pt/Ir probe to produce highly detailed current images on mixed phase Si but a doped diamond-coated Si tip failed to achieve the same high resolution on polycrystalline $CuIn(Ga)Se_2$ as reported by Azulay *et al.* [65]. Ballif *et al.* [134] and Mountinho *et al.* [121, 122] further reported using doped diamond-coated Si tips, in surface and cross-sectional characterisation of CSS grown CdTe, both achieving high resolution current imaging.

As summarized in Table 3.6 and illustrated in Figure 3.16 each tip and cantilever has different properties and therefore choosing a tip appropriate to the application is very important. This is well exemplified when considering the ac- voltage induced mechanical oscillation used in SKPM.

Si tip coating	**Application**	**Cantilever length µm**	**Spring Constant, k, N m^{-1}**
Co/Cr coated	SKPM	225	2.8
Pt/Ir coated	SKPM (CAFM)	225	2.8
Doped diamond- coated	CAFM (SKPM)	125	42

Table 3.6. Summary of Si coated probes used in SPM electrical characterisation

This is heavily dependent on matching the spectral component of the ac oscillation to the cantilevers resonant frequency, this therefore demands that a cantilever with a low spring constant is preferable.

Figure 3.16 provides a good insight into the dimensions of each tip and cantilever used. Immediately evident is the shorter cantilever used by the doped diamond-coated Si tip (125 µm), which yields the high spring constant, k = 42 N m^{-1}. Conversely, the 225 µm cantilever common to both the Co/Cr and Pt/Ir coated Si tips yields k = 2.8 N m^{-1} is evidently preferable in achieving ac-induced mechanical oscillation.

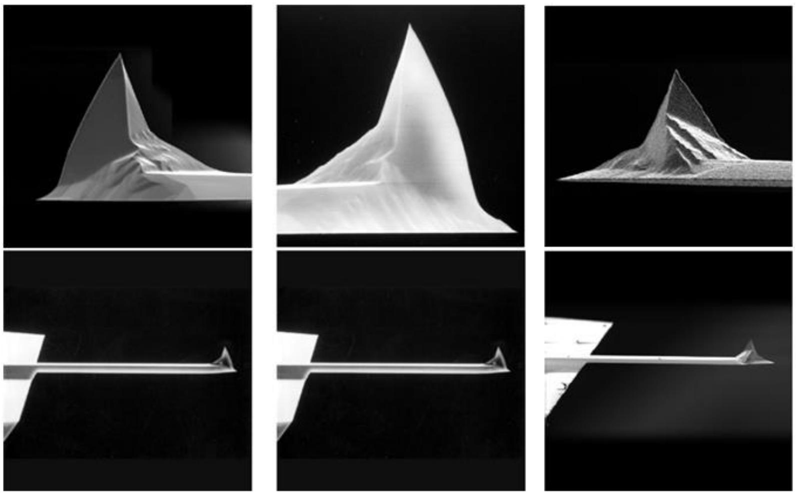

Figure 3.16. SEM images of Veeco probes. Top left: Co/Cr tip and bottom left: cantilever. Top center: Pt/Ir tip and bottom center: cantilever. Top right: doped diamond coated Si tip and bottom right: cantilever. For scales refer to table 7 above. (Images from Veeco Probe catalogue)

3.8.2 Scanning Kelvin probe microscopy

The scanning Kelvin probe microscope (SKPM) incorporates the traditional Kelvin probe principle into an SPM, where high resolution spatially resolved images of surface potential, or contact potential difference (CPD) can be produced. As shown in Figure 3.17 (a) when electrical contact is made between two conducting materials with different Fermi levels, E_f, electrons, e^- from the material with the lower work function Φ flow to the material with the higher Φ, in Figure 3.17 (a) this shows e^- flowing from the CdTe with $\Phi = \Phi_{CdTe}$ to the SPM tip with $\Phi = \Phi_{tip}$ where $\Phi_{tip} > \Phi_{CdTe}$. In SKPM these materials form a parallel plate capacitor with equal and opposite surface charges, equating to E_f equilibration (Figure 3.17 (b)). A voltage is applied until the electric field between the conductors disappears and a null output signal is measured (Figure 3.17 (c)).

CPD measurements can be performed using a static capacitor by measuring the charge flow between two conducting materials, but due to time dependent surface charge dissipation effects continuous measurement is generally not possible. The Kelvin probe technique overcomes this issue by using a vibrating probe to produce a varying capacitance.

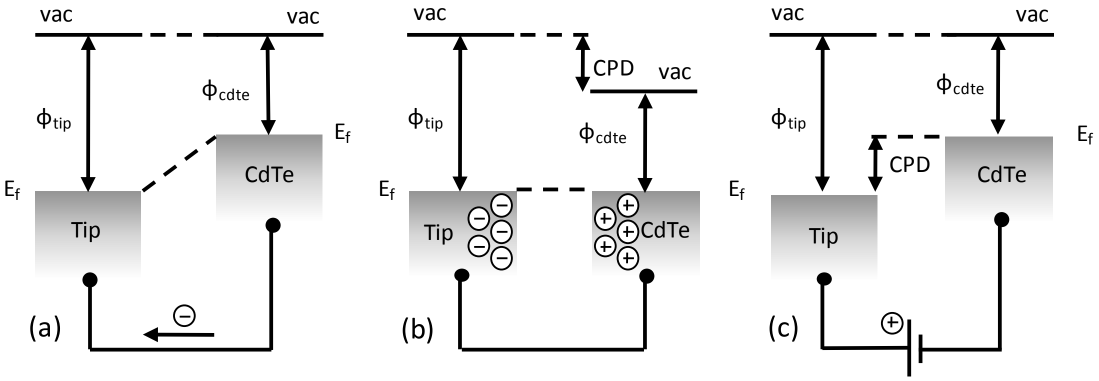

Figure 3.17. Energy level diagram showing (a) electron flow when a conducting SPM tip and CdTe are brought together (b) equalisation of Fermi levels, E_f and (c) application of a nullifying voltage, V_b = - CPD

In SKPM an SPM cantilever with a conducting tip, is induced into mechanical oscillation by applying a ac-voltage, $V_{ac}\sin(\omega t)$ between the tip and sample, in addition to a dc-bias, V_{dc}. The ac-voltage induces an oscillatory electrostatic force:

$$F = \frac{1}{2}\frac{\partial C}{\partial z}V^2 \quad [3.1]$$

Where the spectral component at the frequency ω, of the ac-voltage is:

$$F_\omega = \frac{\partial C}{\partial z}(V_{dc} - CPD)V_{ac}\sin(\omega t) \quad [3.2]$$

$\partial C/\partial z$ is the capacitance gradient between the sample and probe tip. The oscillation at frequency ω is used to nullify the amplitude to zero, where V_{dc} matches the CPD, it is this signal which is used to generate the CPD image.

The instrument used throughout this investigation was a Veeco Dimension 3100. Figure 3.18 shows a schematic of this instrument, in addition to the SKPM and CAFM components. This diagram shows the basic AFM components including the laser, PSPD and piezoelectric actuated Z-feedback loop as well as the SKPM ac- and dc- voltage output and signal amplification circuits. As shown in Figure 3.19, SKPM uses a dual-pass (interleave) process; where each single-axis line scan is first recorded in TappingMode™, this pass produces the topographic image. The topographic line scan is then used to re-trace the same path in non-contact mode, at a pre-selected constant lift height, typically between 50 – 100 nm.

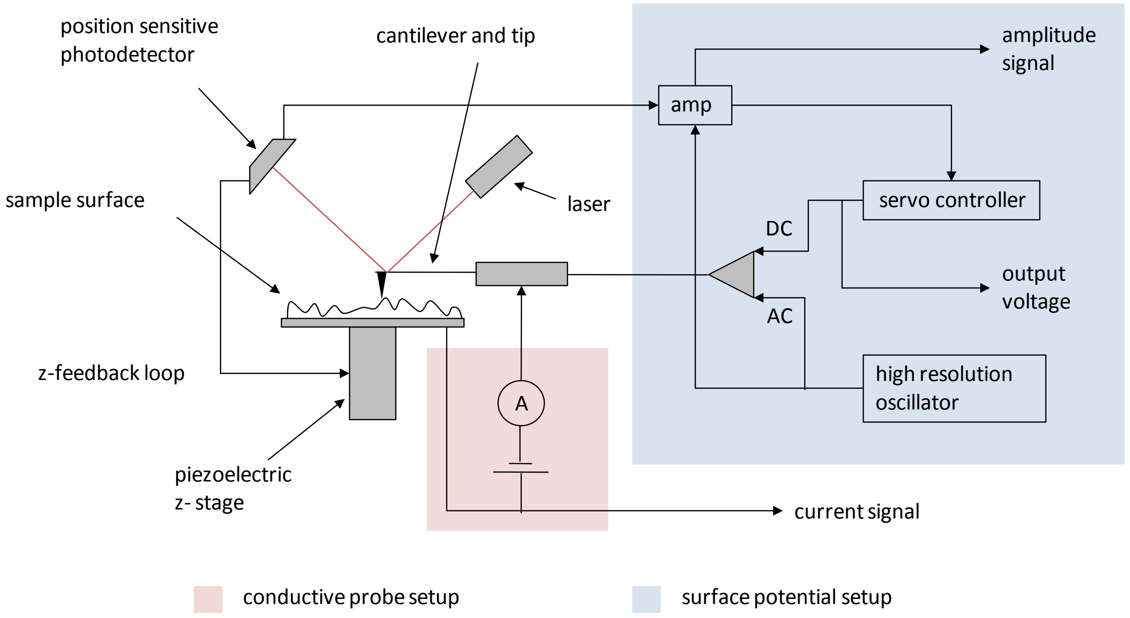

Figure 3.18. Schematic of SKPM and CAFM setups

Figure 3.19 further highlights the separation of topographic and SP effects where, in the non-contact second pass, changes in SP are isolated. This is repeated along the XY plane until both topographic and SP images have been generated. Calibration of the instrument to yield absolute Φ values can be achieved by determining the SPM tip Φ, where $\Phi_{sample} = \Phi_{tip} - CPD$. This is usually accomplished by reference to a material of known Φ.

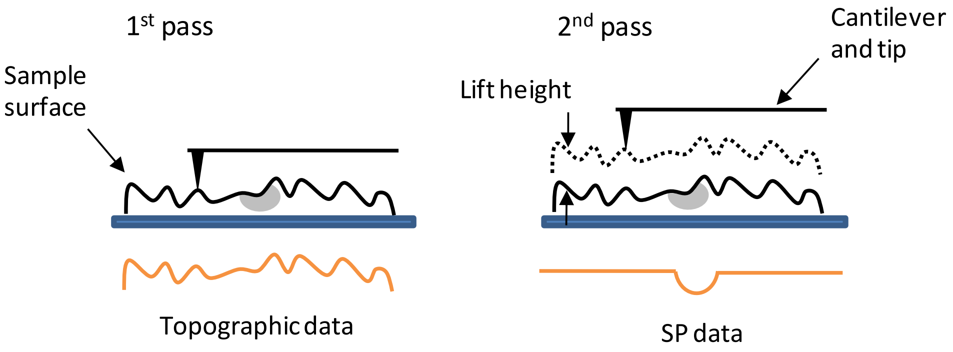

Figure 3.19. Interleave process used in SKPM: 1st pass is made using TappingMode to measure surface topography and the 2nd pass is made using LiftMode to measure SP

Due to their inert nature, Au or highly oriented pyrolytic graphite (HOPG) are both well suited to this function. Examples of this calibration stage will be discussed in further detail in Chapter 5.

3.8.3 *Conductive atomic force microscopy*

In this AFM derivative, the Veeco Dimension 3100 with additional CAFM current amplifier is operated in contact mode, where the topographic signal is measured via the z-feedback loop and current mapping is simultaneously performed. Figure 3.20 illustrates the contacting methodology. Ag paint was used to make electrical contact between the TCO and sample platform, itself the bias source. The current passing between the sample back surface and the scanning conductive tip was measured.

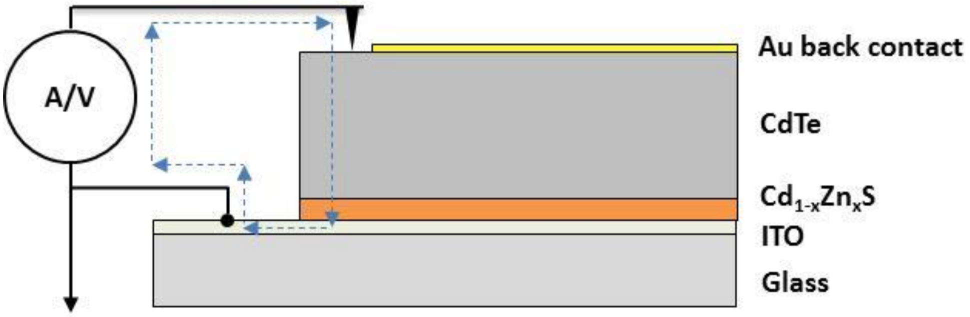

Figure 3.20. Schematic of CdTe cell as contacted for CAFM

Typically, a dc-voltage bias was applied to the sample via the front contact, though high applied biases were discouraged due to the potential effect of localised lattice phonons leading to increased localised resistance.

The scan rate was also an important consideration dictating the quality and reproducibility of the measurement; too slow a rate could lead to charge build up, and irreproducible results. Conversely, too fast a rate could result in smearing of both topographic and current images. Therefore an optimized scan rate is important. A trial and error process was typically used to optimise each CAFM measurement where scan rates were typically between 0.25 and 1 Hz.

4 LBIC Results and Discussion

The optimisation of the LBIC system described in chapter 3 provided the opportunity to successfully use the instrument for the spatially resolved study of PV device structures. This section will present several studies where the triple wavelength LBIC system has yielded interesting insights into performance limiting parameters in thin film solar cells.

4.1 Window layer uniformity in $Cd_{1-x}Zn_xS$ / CdTe devices [135, 136]

The role of the window layer in $Cd_{1-x}Zn_xS$/ CdTe device structures was investigated using the optimized triple wavelength LBIC technique. The growth of a full device structure where the $Cd_{1-x}Zn_xS$ window layer was found to be highly non-uniform presented a serendipitous opportunity to study how this parameter led to lateral photoresponse non-uniformity. Examination of this device provided extensive evidence demonstrating the critical role film uniformity has in overall device performance.

To further understand the observed window layer non-uniformity, a $Cd_{1-x}Zn_xS$ layer which exhibited identical features was grown in isolation. This sample was characterised using profilometry, SEM and EDX, and provided the opportunity to indirectly characterise the non-uniformity observed in the window layer of the full device structure. Profilometry provided information on variations in roughness, surface coverage and thickness. SEM and EDX were also used to identify the features present in the $Cd_{1-x}Zn_xS$ layer.

Furthermore, I-V measurements were used to reveal performance losses which could be related to the window layer uniformity. The triple wavelength LBIC technique expanded on these macroscopic measurements to provide diagnostic analysis of lateral carrier generation and collection uniformity at three wavelength dependent photon penetration depths, $\delta_{p.}$ This approach allowed for the isolation of defects within the device cross-section. This was used to show that $Cd_{1-x}Zn_xS$ film thickness and surface coverage strongly correlated to lateral device performance and window layer thickness distribution.

In addition to these samples, a high performance device was examined where near optimum surface coverage of both the $Cd_{1-x}Zn_xS$ and CdTe layers was observed. This control device allowed effective comparisons to be drawn between all the contact areas studied. Table 4.1 below summarizes the samples used for this study.

Sample	Structure	No. of contacts
A	Poorly nucleated Cd$_{1-x}$Zn$_x$S on ITO/ Glass	n/a
B	Poorly nucleated Cd$_{1-x}$Zn$_x$S / CdTe on ITO/ Glass	4
C	Cd$_{1-x}$Zn$_x$S / CdTe on ITO/ Glass	1

Table 4.1. Summary of samples used in Cd$_{1-x}$Zn$_x$S study

4.1.1 *Cd$_{1-x}$Zn$_x$S layer characterisation*

Figure 4.1 (a) below shows an optical microscope image of sample A, illustrating the non-uniform surface of the film. A 0.5 mm strip was etched through the Cd$_{1-x}$Zn$_x$S thin film to the substrate beneath using a 0.1% Br in MeOH solution, the remaining surface was covered with adhesive tape to ensure the successful preservation of the film. This provided a reference depth for the profilometer scan. Figure 4.1 (b) shows a 4 mm profilometry line scan taken over the solid line indicated in Figure 4.1 (a). The dashed lines in both the image and the graph indicate the position of the etched strip. The arrows indicate the direction of the line scan.

Inspection of the microscope image initially indicates that incomplete island coalescence during film deposition has resulted in partial surface coverage. Further information provided by the profilometry measurement concludes that the layer has a variable thickness where an approximately 300 nm thin film is found over the majority of the sample, but the film thickness drops abruptly to between 20 and 50 nm at the positions initially suspected to exhibit no film coverage.

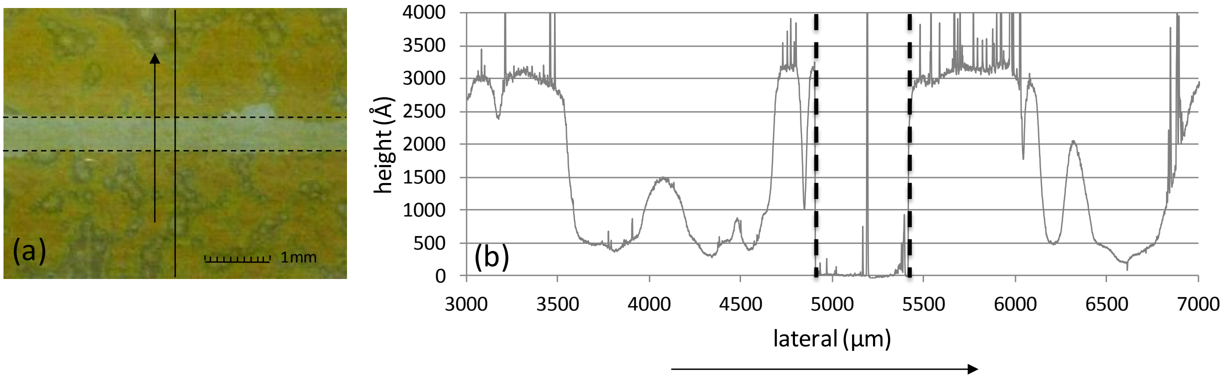

Figure 4.1(a). Profilometry on poorly nucleated Cd$_{1-x}$Zn$_x$S at position indicated in (b) optical microscope image of sample

Further mapping analysis by SEM and EDX revealed the thickness non-uniformity over the scanned areas. Large area EDX scans (5 × 5 mm^2) with dimensions equivalent to the LBIC area scans were used to make direct comparison of the features possible. Figure 4.2 (a) shows an initial SEM image taken over an area of the same dimension to Figure 4.1 (a) and the complimentary EDX maps over the same region. The most abundant EDX signals were Cd $L_{\alpha 1}$, S $K_{\alpha 1}$ and Si $K_{\alpha 1}$, and these are respectively presented in Figure 4.2 (b, c and d). These maps clearly illustrate the non-uniform thickness distribution of the window layer. Regions of abundant Cd and S are abruptly separated by islands of very thin $Cd_{1-x}Zn_xS$ where high Si EDX signals are measured from the boro-aluminosilicate glass substrate.

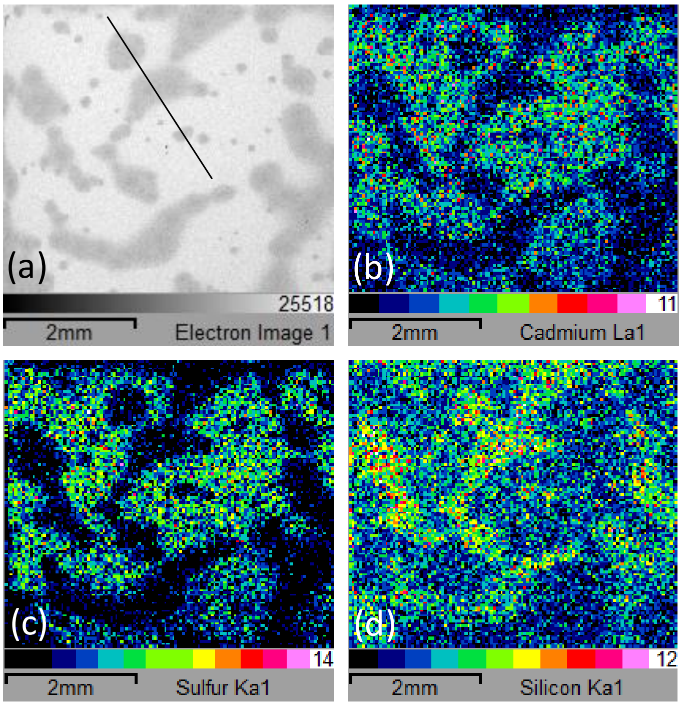

Figure 4.2(a) SEM image of sample B and corresponding EDX maps for (b) Cd $L_{\alpha 1}$ (c) S $K_{\alpha 1}$ (d) Si $K_{\alpha 1}$ signals

Furthermore, Figure 4.3 below shows an EDX line scan taken at the position indicated in Figure 4.2 (a). This expands on the EDX maps to include both Al $K_{\alpha 1}$ and Zn $K_{\alpha 1}$ signals, present in the substrate and deposited film respectively. The line scan clearly shows a reciprocal relationship between the Si $K_{\alpha 1}$ and Al $K_{\alpha 1}$ signals compared to the Cd $L_{\alpha 1}$, S $K_{\alpha 1}$ and Zn $K_{\alpha 1}$ signals, further highlighting the non-uniform film thickness distribution.

The successful characterisation of the non-uniform $Cd_{1-x}Zn_xS$ film provided a good basis on which the triple wavelength LBIC results could be interpreted.

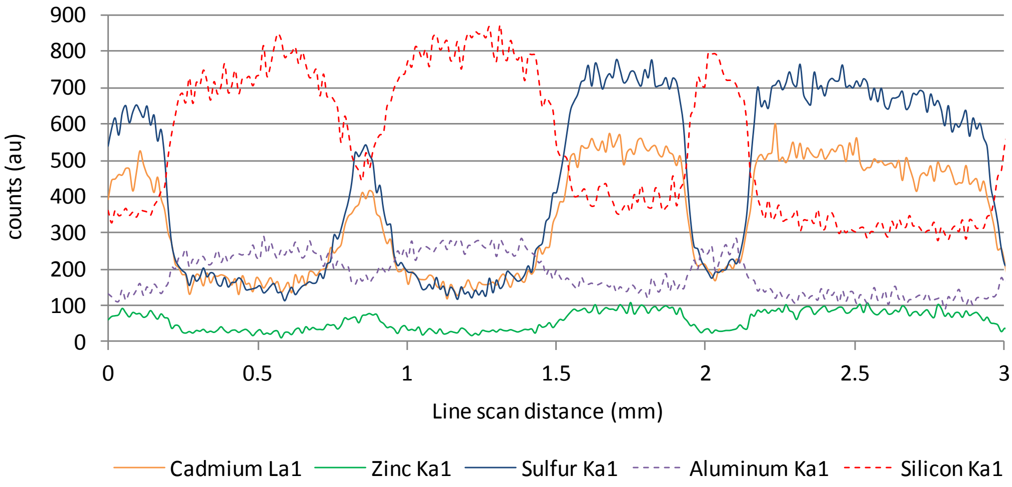

Figure 4.3. EDX line scan over line indicated in Figure 2(a)

4.1.2 LBIC results

Figure 4.4 (a) – (c) show 17 × 17 mm^2 LBIC maps at λ = (a) 405 nm, (b) 658 nm, (c) 810 nm of sample B where Figure 4.4 (d) shows an image of contacts 1 – 4 through the glass substrate. The non-uniformity in the LBIC images (Figure 4.4 (a) – (c)) clearly correlates with the non-uniformity in the $Cd_{1-x}Zn_xS$ window layer visible (through the glass substrate) in Figure 4.4 (d). This LBIC non-uniformity was not apparent in devices where inspection through the glass substrate showed good $Cd_{1-x}Zn_xS$ uniformity. Scribing around the perimeter of each back-contact provided an indication of its position and relation to the LBIC maps. Each of the 4 responsive regions [1-4] corresponds to the four 5 × 5 mm^2 Au back contacts defining the photoactive areas of the device. Contact 1 exhibited the lowest device efficiency, η = 7.8 % (Table 4.2), and open-circuit voltage, V_{oc} = 545 mV. Contact 1 also produced the largest area of high photoresponse at λ = 405 nm as can be seen in Figure 4.4 (a). Approximately 81% of this contact (calculated using a grid system and manually allocating each high/low response region) gives an induced LBIC current between 75 and 82 nA. The remaining 19% of the area gives a significantly lower induced photocurrent of 22 to 28 nA.

The large differences in window layer thickness, as presented in section 4.1.1 account for the large observed differences in photoresponse at λ = 405 nm in the two regions described above. This bimodal distribution of $Cd_{1-x}Zn_xS$ thickness, provides an explanation for the blue-LBIC device photoresponse, where transmittance, % T at λ = 405 nm was 54.1 % in the 50 nm $Cd_{1-x}Zn_xS$ regions and 10.4 % in the 300 nm regions. From these % T measurements it is clear that a high blue-LBIC response would occur in regions where the $Cd_{1-x}Zn_xS$ thickness is 50 nm and conversely a region of low blue-LBIC response would occur in regions where the thickness of $Cd_{1-x}Zn_xS$ was 300 nm.

Contact 2, in Figure 4.4 follows a near identical trend, where high blue optical transmission leads to increased photoresponse at 405 nm over approximately 71 % of the contact area. Contacts 3 and 4 exhibit larger areas of lower photoresponse at 405 nm, due to the increased concentration of ~ 300 nm thick islands of $Cd_{1-x}Zn_xS$ leading to a reduced blue response compared to contacts 1 and 2. For contacts 3 and 4 the 50 nm thickness of $Cd_{1-x}Zn_xS$ accounts for ~ 40 % by area in contact 3 and ~ 55 % in contact 4, the remaining low response regions (22 to 28 nA) correspond to ~ 300nm $Cd_{1-x}Zn_xS$ where high absorption in the $Cd_{1-x}Zn_xS$ leads to low carrier generation and collection in the CdTe layer.

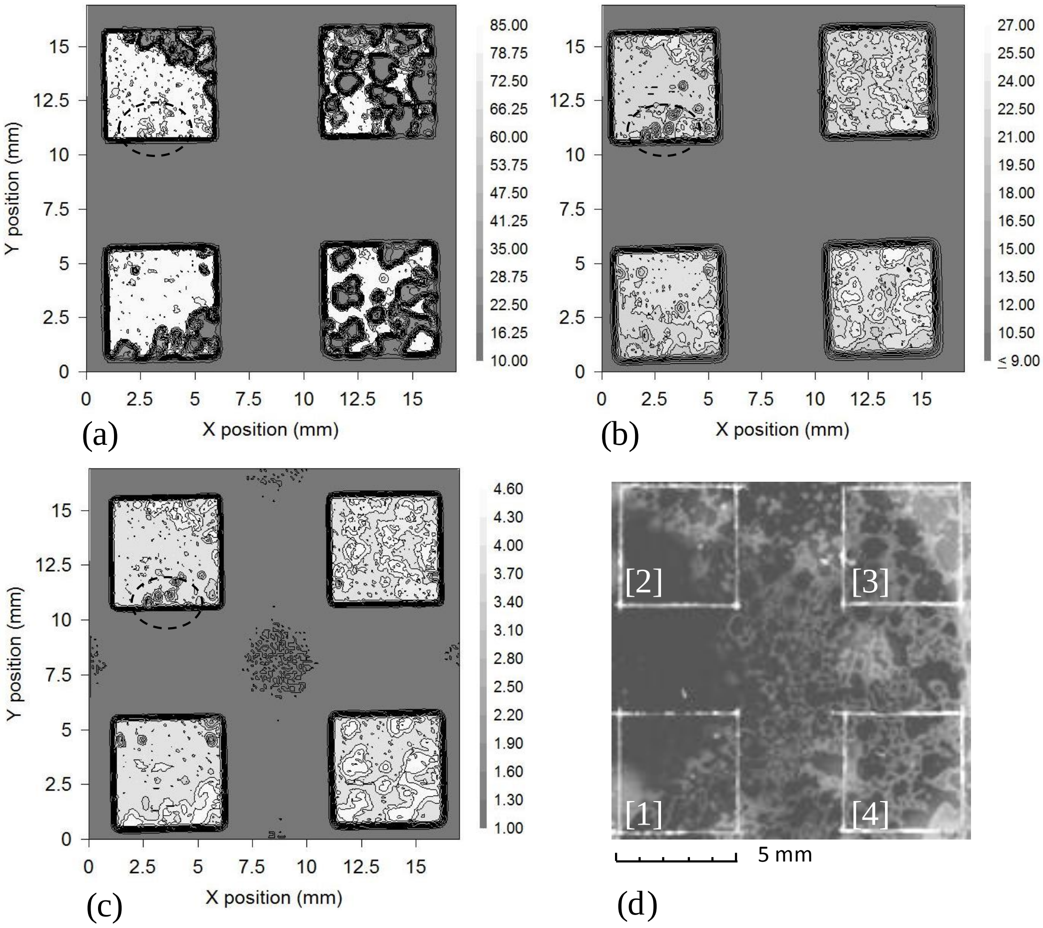

Figure 4.4. 17 x 17 mm2 LBIC maps over 4 individual 5 x 5 mm2 contact areas at λ = (a) 405nm, (b) 658nm, (c) 810nm and (d) image of contacts 1 - 4 through aluminosilicate glass substrate. (Grayscale = 10 - 85 nA (Figure 4.4 (a)), 9 – 27 µA (Figure 4.4 (b)) and 1.0 – 4.6 µA (Figure 4.4 (c))

Figure 4.5 below shows the J-V curves for contacts 1-5 under AM1.5 illumination. The J_{sc} of all the measured contacts fall between a narrow range of 23.0 to 23.8 mA cm^{-2}, showing the J_{sc} to be insensitive to the observed lateral non-uniformities. Conversely the V_{oc} is shown to change as a function of window layer thickness uniformity.

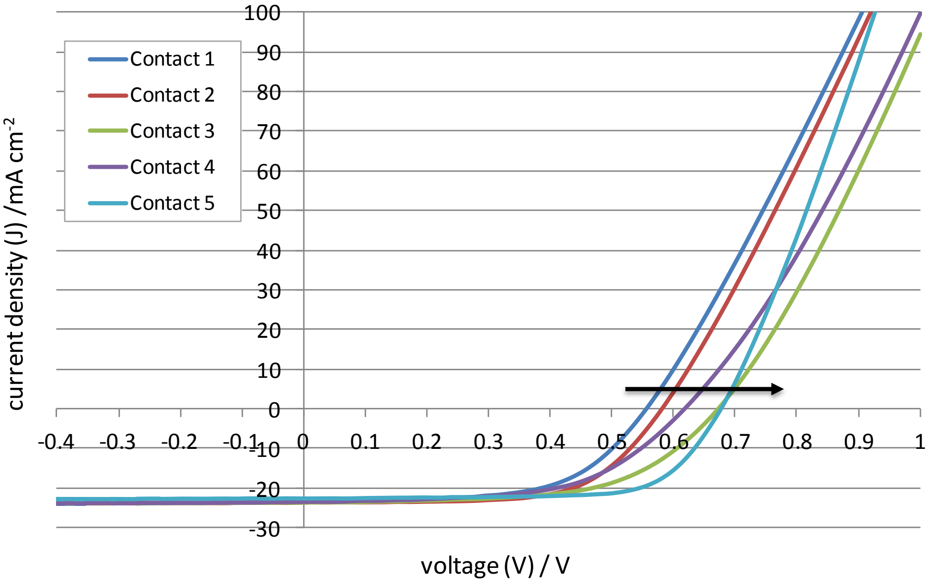

Figure 4.5. J-V plots of contacts 1.5 under AM1.5 illumination conditions showing V_{oc} increase in devices exhibiting increased $Cd_{1-x}Zn_xS$ surface coverage.

Figure 4.6 shows the V_{oc} for each device plotted as a function of the thicker $Cd_{1-x}Zn_xS$ percentage surface coverage and shows a linear correlation.

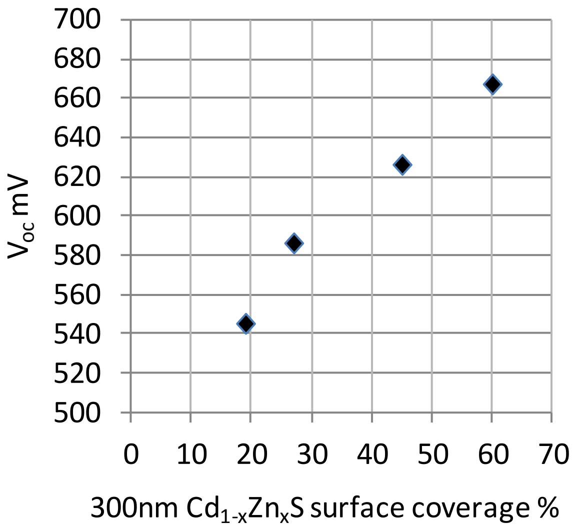

Figure 4.6. Plot showing relationship between open circuit voltage (Voc) and incidence of the thicker (approximately 300nm) $Cd_{1-x}Zn_xS$ surface coverage for each of the devices shown in Figure 4.4.

As the total thick $Cd_{1-x}Zn_xS$ surface area increases from 19 % in contact 1 to 60 % in contact 3, the V_{oc} increases linearly from 545 mV to 667 mV. This trend is explained by a higher V_{oc} in laterally defined islands of thicker $Cd_{1-x}Zn_xS$, where increased LBIC response was observed at λ = 658 nm and 810 nm. This is found to be evident in Figure 4.4 (b) and (c) where photoresponse at 658 nm and 810 nm follow the same spatial pattern, but with opposite response, when compared to LBIC maps recorded at λ = 405 nm. When a low LBIC response at 405 nm was measured, a peak LBIC response in the 658 nm and 810 nm maps was observed, corresponding to a region of high V_{oc}.

One possible relationship between V_{oc} and LBIC response can be considered by localized variations in carrier recombination impacting minority carrier lifetime, τ. Equation [4.1] gives the reverse saturation current (I_s) in a p-type semiconductor using: the elementary charge (e), cross-sectional area (A), carrier diffusion coefficient (D), intrinsic carrier concentration (n_i), acceptor level (N_A) and minority carrier lifetime (τ). This shows that a drop in τ will lead to an increase in I_s. Equation [4.2] shows that increased I_s will lead to a drop in V_{oc}, (where I_L is the light – generated current).

$$I_s = eA\left(\sqrt{\frac{D}{\tau}}\,\frac{n_i^2}{N_A}\right) \qquad [4.1]$$

$$V_{oc} = \frac{nkT}{e}\ln\left(\frac{I_L}{I_s}\right) \qquad [4.2]$$

It is postulated that where the $Cd_{1-x}Zn_xS$ thickness is 300 nm and higher LBIC response at longer wavelengths is measured, an increased τ and reduced I_s leads to localised regions of high V_{oc}. Conversely, in regions where the $Cd_{1-x}Zn_xS$ layer is thin, τ is reduced, causing an increase in I_s and corresponding decrease in V_{oc}. This conclusion implies that a thin $Cd_{1-x}Zn_xS$ window layer leads to a more defective depletion region in the CdTe and therefore yields a device with a higher recombination rate.

Figure 4.6 and Table 4.2 show that $Cd_{1-x}Zn_xS$ thickness distribution correlates with the measured V_{oc} for each of the devices but R_{sh} is shown to be independent of this distribution. This indicates that the variation in window layer thickness over each contact does not correlate with shunting in the same way that the V_{oc} has been shown to correlate with the window layer coverage. Shunting is normally associated with micro-shorts in the CdTe absorber and not necessarily related to the thickness of the window layer. Koishiyev et al. suggests a 2-D model where modules are divided into cells, sub-cells and microcells [137, 138]. If a similar methodology is considered; where each contact is compartmentalised into a number (n), of photo active regions, or 'micro-cells', where n is dependent on the step increment of the LBIC instrument. This model shows that the fill factor (FF) contribution to the cell efficiency loss can be explained by the moderate to high clustering of shunted microcells. This corresponds to the observed R_{sh} independence to the $Cd_{1-x}Zn_xS$ window layer thickness distribution, where pin-holes are found to be present in both thick and thin regions of the $Cd_{1-x}Zn_xS$ and CdTe layers. A phenomenon discussed in further detail in section 4.1.4.

Contact	**η (%)**	**J_{sc} (mA cm^{-2})**	**V_{oc} (mV)**	**FF (%)**	**R_s (Ω cm^2)**	**R_{sh} (Ω cm^2)**
[1]	7.8	23.8	545	60.0	3.3	571
[2]	8.7	23.7	586	62.8	3.2	1685
[3]	9.3	23.6	667	59.3	3.8	1124
[4]	8.4	23.8	626	56.0	4.0	719
[5]	10.9	23.0	687	70.9	2.6	2005

Table 4.2. Current density – voltage (J-V) results from devices [1] – [5]. All results measured over full 5 x 5 cm2 contact areas

Figure 4.7 (a) – (c) shows LBIC maps of contact 5 at λ = (a) 405 nm, (b) 658 nm and (c) 810 nm. This contact was taken from a different PV device from contacts 1-5, where AM1.5 device efficiency was measured at 10.9 %. Good LBIC uniformity can be seen at all incident wavelengths in contrast to the poorer devices shown in Figure 4.4. At λ = 405 nm, LBIC response was low, where a relatively uniform (300 nm thick) $Cd_{1-x}Zn_xS$ window layer (measured using *in situ* laser reflectance during deposition) absorbs the majority of incident photons, as expected. The LBIC response shown in Figure 4.7 (a) shows small variations in blue light transmission over the 5 × 5 mm^2 contact area, where a plateau response of 50 to 60 nA was measured and small (~ 100 μm diameter) spikes in response (~ 90 nA) are observed.

The circled defect in Figure 4.7 (a) – (c) indicate a 250 to 300 μm wide window layer pin-hole, where a maximum signal response of ~ 110 nA was recorded at λ = 405 nm. Evidence of this pin-hole was also found at λ = 658 nm and 810 nm where a reduced LBIC response was observed. Overall, this cell showed an increased V_{oc} of 687 mV (compared with contacts 1 - 4) and is consistent with more uniform $Cd_{1-x}Zn_xS$ film thickness. However, this still falls short of what would be expected for the best devices, which would require removing the pin-holes observed in Figure 4.7.

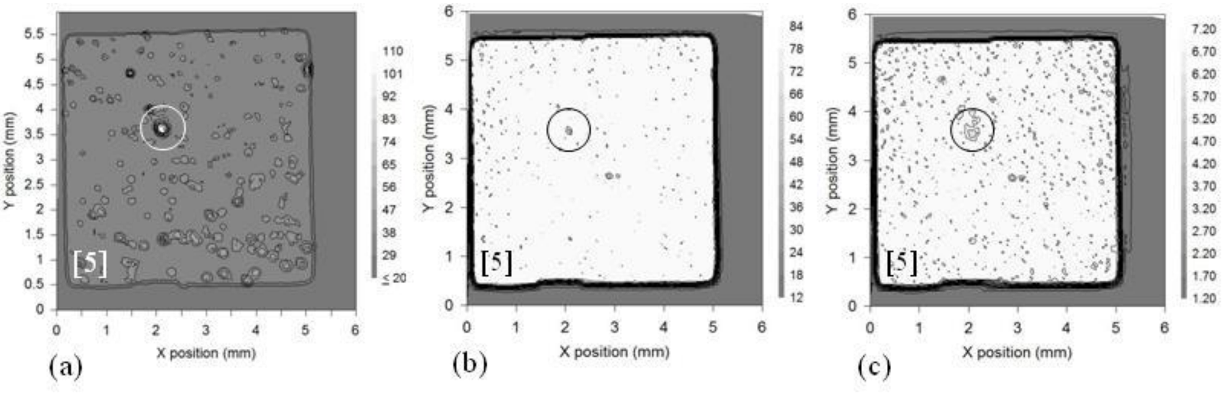

Figure 4.7. 6 x 6 mm^2 LBIC maps over contact 5, 5 x 5 mm^2 contact areas at λ = (a) 405nm, (b) 658nm, (c) 810nm. (Grayscale = 20 – 110 nA (Fig 6 (a)) and 12 – 84 µA (Fig 6 (b)) and 1.2 – 7.2 µA (Fig 6 (c))).

An extrapolation of the plot in Figure 4.6 indicates that 100 % surface coverage with thick $Cd_{1-x}Zn_xS$ would yield a V_{oc} = 780 mV, whereas experimental results from the most uniform $Cd_{1-x}Zn_xS$ device in this study (Figure 4.7) show a lower V_{oc}. This can be attributed to the remaining defects observed in these LBIC maps from which it can be concluded that $Cd_{1-x}Zn_xS$ uniformity and surface coverage can be improved further. These improvements would take the $Cd_{1-x}Zn_xS$ window layer into the performance realms of bi-layer materials; where TCOs are combined with high-resistivity buffer layers to compensate for the effects of thin CdS [139]. This would be an alternative route to high V_{oc} where relatively thick alloy window layers can also provide high short wavelength transmission.

4.1.3 Back surface contamination

In contrast to the window layer non-uniformity contribution observed in the LBIC images, additional defects were identified, circled in Figure 4.4 (a) – (c). The dashed circle in each image highlights a series of defects, where the LBIC response drops by 39 % (~ 26 µA to 15 µA) and 42 % (~ 4.3 µA to 2.5 µA) in both 658 nm and 810 nm maps respectively. These defects are also identified in the 405 nm map showing a decrease of 13 %, (~ 81 nA to 70 nA), though these features are visibly smaller in the 405 nm map compared to their 658 nm and 810 nm counterparts. These defects measure 200 to 300 µm in Figure 4.4 (a) and 500 to

600 µm in Figure 4.4 (b) and (c). Inspection of the back contact surface using SEM and EDX analysis confirms that these longer wavelength dependent defects originate from back surface contamination.

Figure 4.8 (a) and (b) below show the Au back contact and the uncoated CdTe separated by a horizontal scribed line. Furthermore, several 0.5 to 1 mm diameter defects are observed in the SEM image. By reference to the complimentary EDX maps, highlighted in Figure 4.8 (c), the high concentration of Ga at the same locations as the defects indicate that this contamination is In/Ga eutectic paste. This eutectic was used on the device to enhance front contact conductivity, and *should* remain isolated to the TCO surface. Any Au surface contamination shows a significant impact on photoresponse at 658 and 810 nm, whereas it is seen to be less sensitive at 405 nm, indicating that the effect of this contamination decreases towards the pn junction where the majority of carriers from the blue laser are generated.

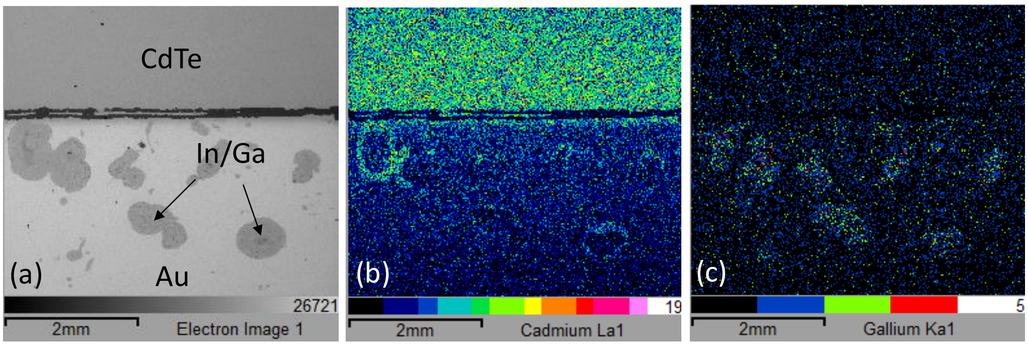

Figure 4.8. SEM image of contact 2 edge in sample B and corresponding EDX maps for Cd $L_{\alpha 1}$ and Ga $K_{\alpha 1}$

4.1.4 High resolution LBIC on $Cd_{1-x}Zn_xS$ / CdTe devices [136]

The LBIC studies presented in section 4.1.2 were expanded to include higher resolution measurements on both samples B and C. This was achieved by reducing the beam width to approximately 10 µm and the XY translation step to 5 µm. The incident laser beam power was adjusted with reference to the calibration tables presented in chapter 3 to maintain a comparable carrier injection density.

Figure 4.9 shows a 0.5 x 0.5 mm LBIC map of contact 5 (Figure 4.7) at incident wavelengths, λ = (a) 405 nm, (b) 658 nm and (c) 810 nm. Photoresponse is characterised by two primary observations:

1. A relatively uniform photoresponse at all 3 incident wavelengths over the majority of the area.
2. The identification of pinhole defects (labelled with arrows).

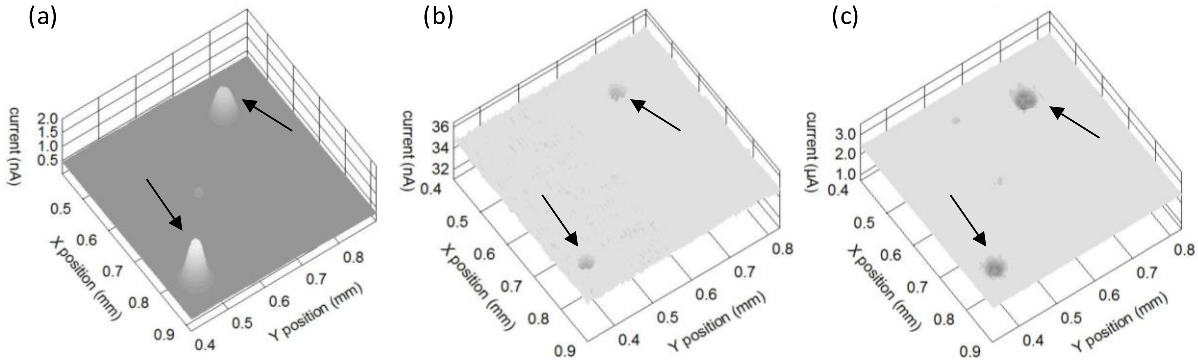

Figure 4.9. LBIC maps over 0.5 x 0.5 mm area on 240 nm $Cd_{1-x}Zn_xS$ / 2µm CdTe at (a) 405 nm (b) 658 nm and (c) 810 nm incident laser wavelengths

The plateau LBIC response observed at all incident wavelengths indicates uniform photoresponse at the 3 wavelength dependent generation depths. Figure 4.9 (a) shows low blue response corresponding to high absorption in the $Cd_{1-x}Zn_xS$ window layer, as observed in the similar lower resolution measurements on the same material. Conversely, Figure 4.9 (b) and (c) show red and IR transmitted through the $Cd_{1-x}Zn_xS$ is highly absorbed in the CdTe producing relatively higher LBIC responses.

The LBIC identified defects highlighted in Figure 4.9 show that photoresponse is affected at all incident wavelengths, though the way in which the defect impacts the LBIC response does vary. At $\lambda = 405$ nm the defect is observed as a high ‘spike’ in photoresponse whereas, at $\lambda = 658$ nm and 810 nm, at the same XY coordinates the defect is seen as a ‘dip’ in photoresponse. The triple-wavelength LBIC technique has provided a diagnostic route to identify the origin of the pin-hole defect within the cross-sectional structure of the device.

The defects identified in Figure 4.9 indicate that approximately 50 µm diameter pin holes in the $Cd_{1-x}Zn_xS$ window were responsible. This leads to reduced $Cd_{1-x}Zn_xS$ absorption and consequently increased blue LBIC response in these localised regions. These window layer defects are also observed to effect wavelengths that are absorbing in the CdTe absorber layer ($\lambda = 658$ and 810 nm), where a pin hole in the $Cd_{1-x}Zn_xS$ window layer leads to reduced photocurrent in the CdTe, indicating that these regions represent localised areas where either (a) carrier generation and collection or (b) minority carrier diffusion was poor.

Figure 4.10 (a) – (c) show 0.5 x 0.5 mm LBIC maps of contact 4 (Figure 4.4) where $Cd_{1-x}Zn_xS$ window layer thickness was known to vary from ~ 50 to 300 nm. LBIC responses at all wavelengths contrast with the results shown in Figure 4.9; where, most notably, the presence of $Cd_{1-x}Zn_xS$ window layer pin holes were identified.

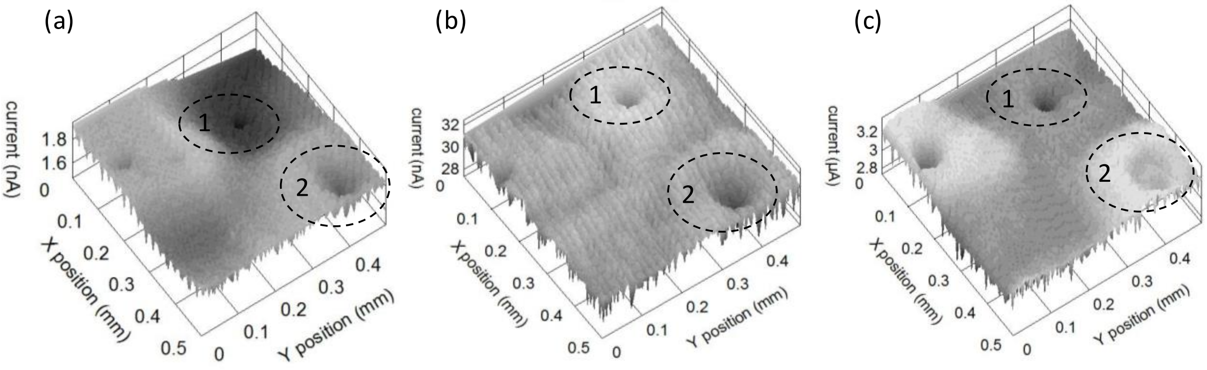

Figure 4.10. LBIC maps over 0.5 x 0.5 mm area on variably nucleated $Cd_{1-x}Zn_xS$ / 2μm CdTe at (a) 405 nm (b) 658 nm and (c) 810 nm incident laser wavelengths.

Figure 4.10 shows pin hole defects at all incident wavelengths, though contrasting from Figure 4.9 by appearing as drops in LBIC response at 405 nm as well as 658 nm and 810 nm. This indicates that pin holes in the CdTe, causing very low absorption, are leading to a sharp drop in LBIC photoresponse at all wavelengths.

Furthermore, the known $Cd_{1-x}Zn_xS$ thickness distribution leads to a variable LBIC response over the full scanned area at all wavelengths; this is in contrast to the plateau-type response found in Figure 4.9. Two different regions in Figure 4.10 are highlighted where thickness variations relating to both the $Cd_{1-x}Zn_xS$ and CdTe layers can be seen; region 1 shows a pin hole defect where the surrounding LBIC response varies in each map. At $\lambda = 405$ nm (Figure 4.10 (a)) the average LBIC response was low, indicative of increased blue absorption and a thicker $Cd_{1-x}Zn_xS$ layer. At $\lambda = 658$ nm (Figure 4.10 (b)) an increased LBIC response was measured, in contrast, at $\lambda = 810$ nm (Figure 4.10 (c)) a relatively low LBIC response was measured. This indicates that increased red but reduced IR absorption was occurring. This result can be explained by a localised region (over the scan area) of thin CdTe where 1 - (1/e) absorption at 810 nm requires 2005 nm of CdTe. In contrast, region 2 in Figure 4.10 shows a relatively high response region surrounding the pin hole defect in each LBIC map, giving a ‘volcano’ appearance. In Figure 4.10 (a) this is consistent with a thinner $Cd_{1-x}Zn_xS$ layer, leading to reduced blue absorption. At $\lambda = 658$ and 810 nm, a relative increase in local photoresponse can be explained by increased absorption due to a localised region of thicker CdTe which is leading to a higher LBIC response at both wavelengths.

Figure 4.9 and Figure 4.10 both clearly illustrate the versatility of the triple wavelength LBIC instrument to isolate the origins of different defects to different layers within a device cross-section. This has provided unparalleled insights into how lateral variations in film thickness uniformity impact lateral photoresponse uniformity in CdTe solar cells.

4.2 LBIC on fluorescent nanocrystals [140]

The LBIC instrument was used to analyse the spatially resolved scattering effects of a luminescent down shifting (LDS) layer incorporated into a full CdTe device structure. CdSeS alloyed quantum dots (QD’s) incorporated into a polymethyl, methacrylate (PMMA) polymer matrix were used to form the LDS layer. Figure 4.11 (a) and (b) below show the front and back side of the CdTe solar cell defined by the 5 × 5 mm^2 back contact surface area, a scribe around this contact area provided a reference point for the LBIC scan area. An intentionally scratched back contact provided a reference for lateral collection in LBIC measurements with and without the QD-LDS layer. The delaminated QD-PMMA LDS film is shown in Figure 4.11 (c). The film was originally deposited onto a glass microscope slide using the doctor-blading technique. This delamination conveniently allowed for the film to be mounted on the cell where a refractive index matching optical gel was used to adhere the film to the front side of a CdTe solar cell as shown in Figure 4.11 (d). This eliminated any air interface at the QD-LDS film - glass substrate interface and minimised reflection losses associated with this interface.

Figure 4.12 shows the EQE spectra of the CdTe device shown in Figure 4.11 with and without the QD-LDS layer adhered to the front surface. In the EQE measurement of the device incorporating the QD-LDS layer a 16 % increase in EQE between 300 – 450 nm is observed relative to the standard non-QD-LDS device. This corresponds to a significant increase in blue light collection.

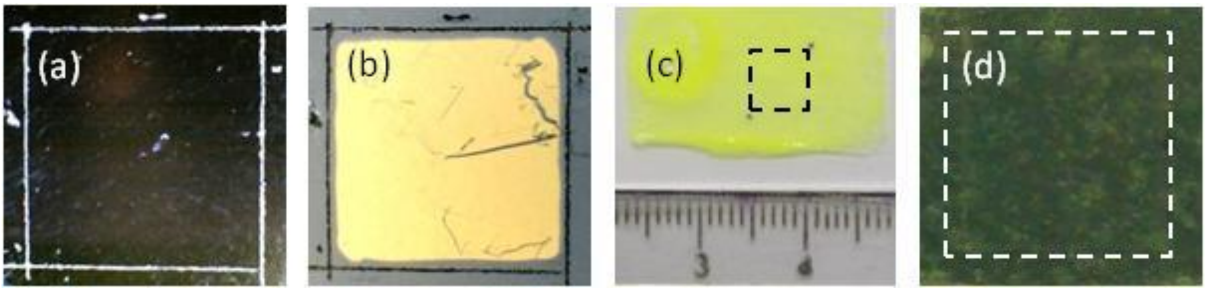

Figure 4.11. Images showing (a) the front side and (b) the back side of the CdTe solar cell used for the QD-LDS-CdTe-LBIC study, (c) the delaminated QD-LDS film and (d) the QD-LDS film adhered to the front side of the CdTe cell using optical gel to minimize reflection losses by removing the QD-LDS film-substrate air interface.

Conversely, above the $Cd_{1-x}Zn_xS$ absorption edge at ~ 450 nm EQE losses are observed at all wavelengths up to the CdTe absorption edge. These losses are attributed to (a) QD and device absorption overlap between 450 and 500 nm and (b) long wavelength scattering losses associating with the QD-LDS layer. Figure 4.13 shows LBIC maps of the CdTe device with and without the QD-LDS layer at 405, 658 and 810 nm as labelled.

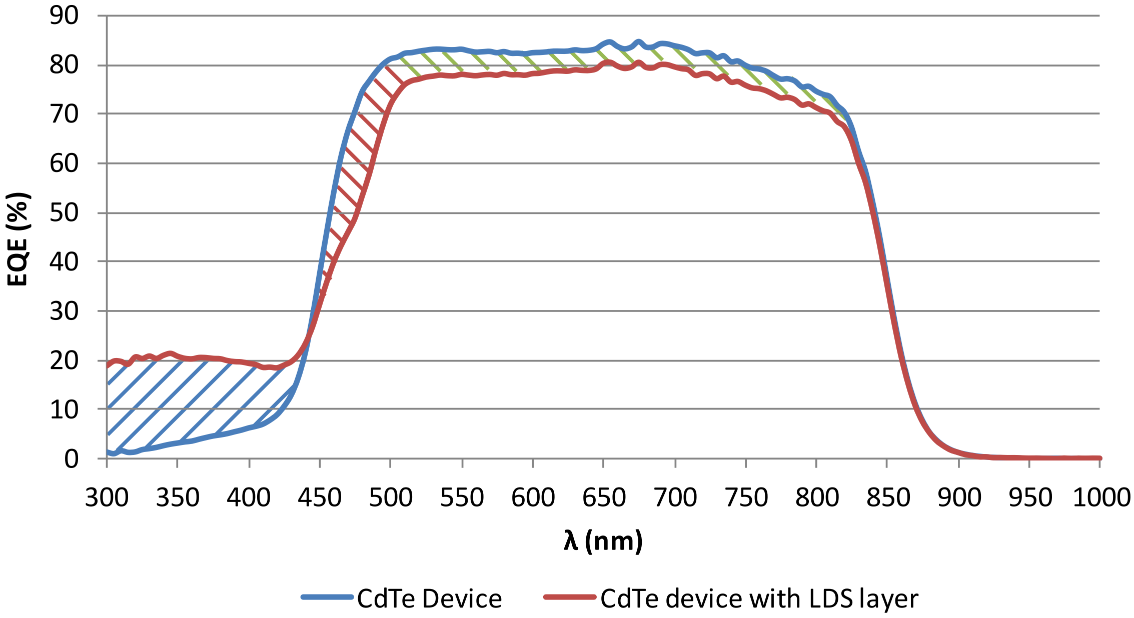

Figure 4.12. EQE spectra of full CdTe device with and without luminescent down shifting (LDS) layer

Figure 4.13 (a) shows a 405 nm LBIC map of the CdTe device without the QD-LDS layer. The boundary of the back contact area is clearly defined where an abrupt drop in carrier collection outside the 5 × 5 mm^2 contact area is observed. Furthermore, the scratches on the back contact (Figure 4.11 (b)) are clearly visible as well as some further carrier collection non-uniformity associated with both the window and absorber layer.

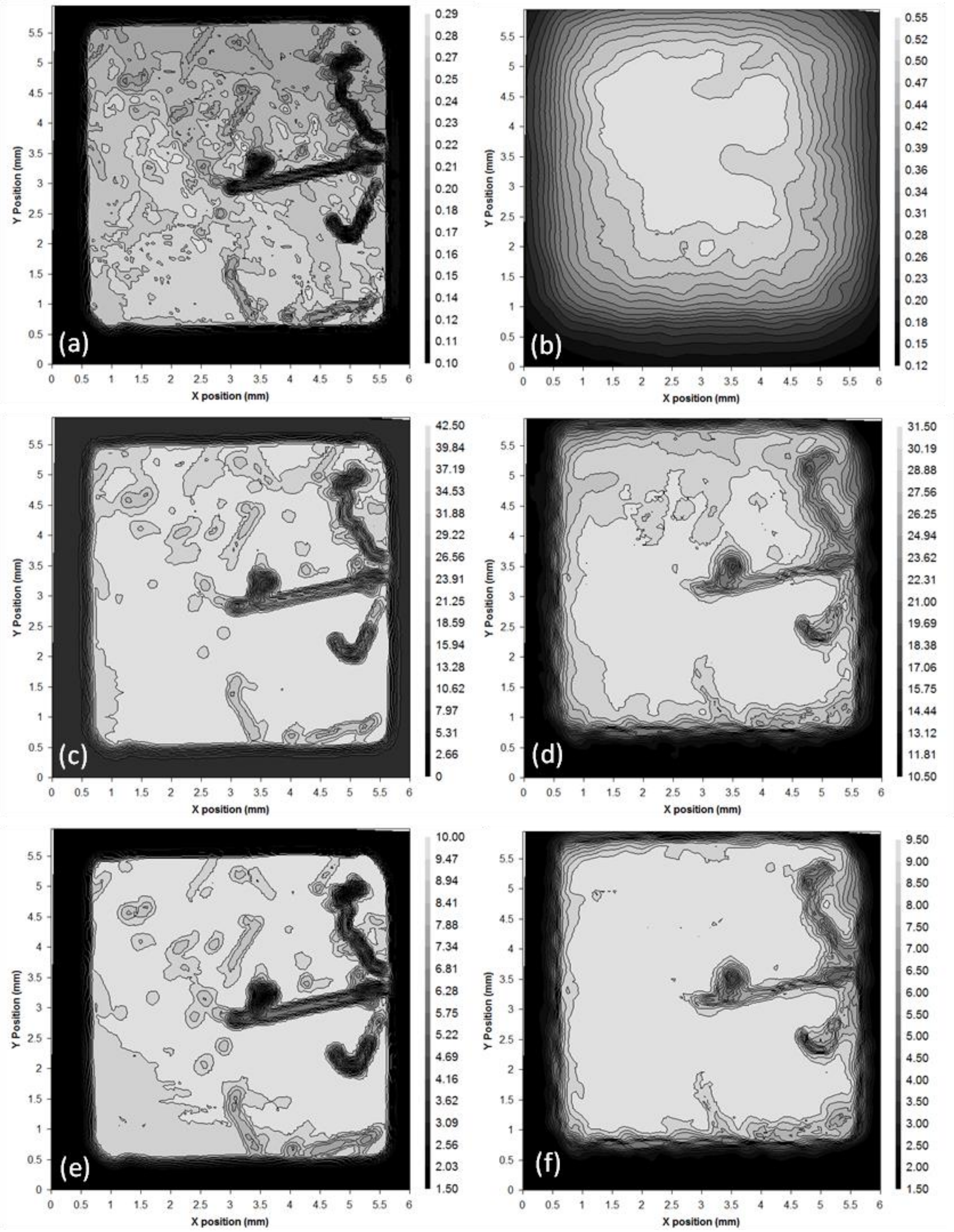

Figure 4.13. LBIC maps showing 5 × 5 mm^2 CdTe contact without QD-LDS layer at (a) 405 nm (c) 658 nm and (e) 810 nm and the same contact with a CdSeS QD in PMMA LDS layer adhered to the front surface of the cell at (b) 405 nm (d) 658 nm and (f) 810 nm

The non-uniformity contributions can be isolated to each layer with reference to the LBIC maps at longer wavelengths (Figure 4.13 (c) and (e)). Figure 4.13 (b) shows an LBIC map at 405 nm of the CdTe contact with the QD-LDS layer adhered to the front surface of the device. Two key observations can be made:

1. A significant reduction in the definition of both the active area and scratch is observed when compared to the standard device due to the isotropic light emission of the QD's as illustrated in Figure 4.14. This light scattering effectively increases the LBIC collection area per LBIC data point measured resulting in reduced image resolution and blurring of the defects observed in the standard device at this wavelength. Furthermore the effective contact area is observed to increase due to incident light absorbed by the QD-LDS layer outside the back contact area being emitted in the direction of the active area of the device.
2. The overall current measured when using the QD-LDS layer and the 405 nm laser is higher. A peak current of 0.55 µA is measured on the device incorporating the QD-LDS layer compared to 0.29 µA on the standard CdTe device. This is consistent with the EQE spectrum which clearly shows enhanced blue response at this wavelength.

Figure 4.13 (c) and (d) respectively show LBIC maps at 658 nm of the standard CdTe device and the CdTe device with the QD-LDS layer. Similarly, Figure 4.13 (e) and (f) show the corresponding LBIC maps at 810 nm on the standard CdTe device and the device using the QD-LDS layer.

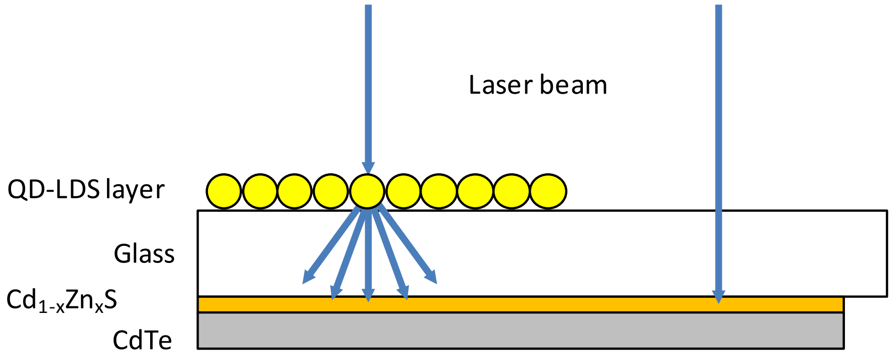

Figure 4.14. Schematic showing LBIC laser beam with and without the QD-LDS layer.

These LBIC maps highlight the transparency of the longer wavelength lasers with respect to the QD-LDS layer. The contact edges and scratch defects are still defined in each image (Figure 4.13 (d) and (f)), though some blurring of the main contact area, and the appearance of gradations in LBIC response beyond the contact boundaries is observed. This indicates that when the laser beam is incident at positions between approximately 0 and 0.3 mm outside the primary contact area (as delimited by the first LBIC measurements and shown in Figure 4.13 (c) and (e)) light is being scattered back toward the contact area and producing a low LBIC signal. Any potential gains this may provide are evidently outweighed by the total scattering and reflection losses which lead to an overall reduction in carrier collection at each of these longer wavelength measurements. At 658 nm the peak LBIC current without the QD-LDS layer was 42.5 μA, this was observed to drop to 31.5 μA when the QD-LDS layer was placed on the device. The 810 nm measurement follows a less pronounced but similar trend with a peak LBIC current of 10.0 μA without the QD-LDS layer and 9.5 μA when the QD-LDS layer is placed onto the cell.

This corresponds with the EQE measurements shown in Figure 4.12 where a reduced carrier generation and collection is observed at wavelengths above ~ 450 nm and provides a suitable explanation for the observed losses at these wavelengths.

4.3 *LBIC on Plasma Cleaned TCO substrate device*

The LBIC instrument has demonstrated the capacity to characterise carrier collection uniformity on devices where defects are known to exist. This has proven of interest when attempting to determine the effects of certain material non-uniformities on PV device performance. In contrast to the overtly non-uniform devices, a uniform device was chosen for LBIC study where prior to thin film deposition the TCO had been cleaned using an Ar^+ plasma. This process was carried out by Plasma Etch Inc. USA.

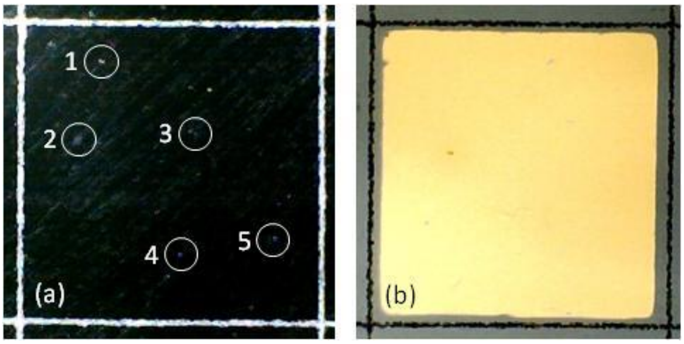

Figure 4.15 Image of (a) front side and (b) back side of CdTe device where prior to thin film deposition, the substrate was cleaned using an Ar plasma, by Plasma Etch Inc.

Figure 4.15 shows an image of (a) the front side of the CdTe device through the glass substrate and (b) the back contact defining the active area of the device. Scribing around the contact area ensured easy sample and beam positioning.

Figure 4.16 below shows LBIC maps of the plasma cleaned $Cd_{1-x}Zn_xS$/ CdTe device at (a) 405 (b) 658 and (c) 810 nm. A significant improvement in photoresponse uniformity at all wavelengths is observed when compared with a device having undergone a standard ultra-sonic bath clean, as shown in Figure 4.7. Although an improvement in collection uniformity is observed there remain significant defects which are most notably exhibited in Figure 4.16 (a). This LBIC map shows 5 prominent defects (labelled 1-5) at 405 nm. As discussed in Chapter 3, photon absorption at this wavelength is consistent with window layer absorption and any subsequent carrier generation and collection can indicate the position of lateral non-uniformities (thin regions) in this layer. The position of these LBIC identified defects are also shown in Figure 4.15 (a) where the appearance of small blemishes seen through the glass side of the device are confirmed to be window layer defects and cell performance limiting areas.

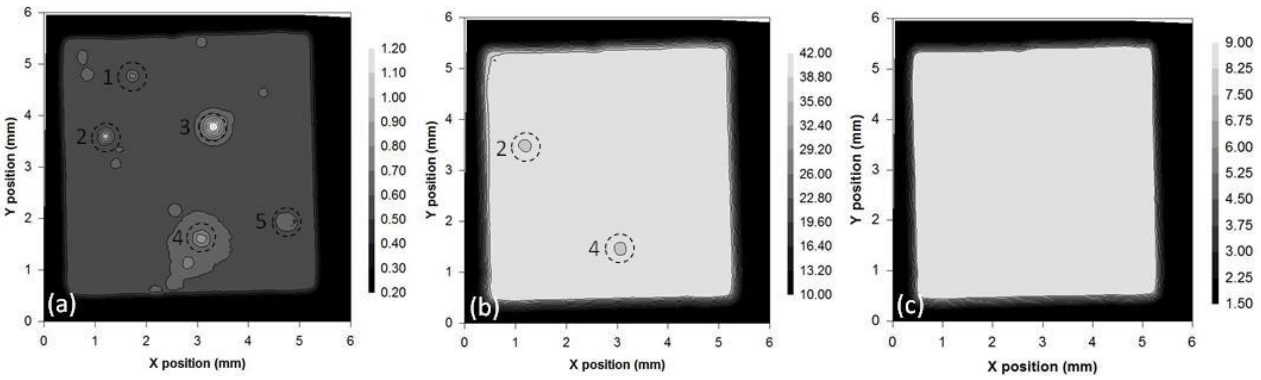

Figure 4.16. LBIC maps of plasma cleaned platform device at (a) 405 (b) 658 and (c) 810 nm. Grayscale = µA

Previously, as shown in Figure 4.7, window layer defects have been seen to reduce carrier collection at longer wavelengths, this is also observed in this device, where defects 2 and 4 (labelled in Figure 4.16 (a) and (b)) are observed at both 405 and 658 nm. At 405 nm, all defects are observed as circular spikes in photoresponse, conversely, at 658 nm, defects 2 and 4 are seen as dips in photoresponse. This is consistent with earlier results which indicated isolated regions of weak cell performance coincide with regions of high blue transmittance (indicative of localised regions where the window layer is very thin).

Interestingly, only two of the five defects shown in Figure 4.16 (a) are found in Figure 4.16 (b) and none are observed in Figure 4.16 (c). This indicates that the window layer defects observed in devices grown on plasma cleaned substrates are less detrimental to carrier collection at longer wavelengths than those observed in devices grown onto conventionally cleaned substrates where conversely, the effects of window layer defects *have* been observed to lead to localised reductions in photoresponse at both 658 nm and 810 nm wavelengths (as shown in Figure 4.7).

This observation highlights an overall improvement in the lateral carrier collection uniformity of the device when using the plasma cleaning technique prior to thin film deposition. Although, the LBIC technique has also shown that window layer related defects continue to persist and further work is required to refine the cleaning procedure to fully eliminate these defects.

5 SPM Results and Discussion

This chapter presents a series of spatially resolved investigations studying thin film CdTe PV devices using scanning Kelvin probe microscopy (SKPM), also known as surface potential (SP) microscopy, and conductive probe atomic force microscopy (CAFM). These techniques are both scanning probe microscopy (SPM) derivatives based on the atomic force microscope (AFM).

5.1 Scanning Kelvin probe microscopy (SKPM)

5.1.1 Calibration of SKPM probe tip

SKPM measures the contact potential difference (CPD) between two different conductors, providing a relative indication of work function (Φ). To obtain a measurement of absolute Φ a reference material of known Φ is required. When made under ambient conditions SKPM measurements are susceptible to surface contamination caused by adsorbed layers (eg. hydrocarbons and water) which can form unstable interface dipole states and subsequently an unstable work function. Therefore, for calibration purposes a chemically inert material is required.

Typical reference materials include Au [141] and highly oriented pyrolytic graphite (HOPG) [142] which have literature Φ values of 5.10 eV and 4.48 eV respectively. As Au was routinely used for back contacting purposes in CdTe solar cell fabrication, calibrating the probe tip using an evaporated layer of Au on glass was initially attempted. To assess the stability of the Au surface in ambient conditions, SKPM measurements were performed approximately 1 day after the Au deposition and then repeated approximately 1 week after deposition. Figure 5.1 (a) and (b) show a 400 × 400 nm AFM image of the Au surface, and the corresponding spatially resolved SP image respectively[1]. These images were simultaneously recorded (using the interleave function described in Chapter 3) approximately 1 day after the deposition of the Au film. A distinctive island-type growth is observed in the

---

[1] z-axis interpretation: the z-axis range is labelled at the top RHS of each image; eg. Figure 5.1 (a) z = 20nm, therefore black = -10 nm and white = +10 nm, where zero lies exactly in the centre of the grayscale.

AFM image and a uniform CPD over the 400 × 400 nm area is observed in the CPD image. This yielded an average CPD of 34.61 mV.

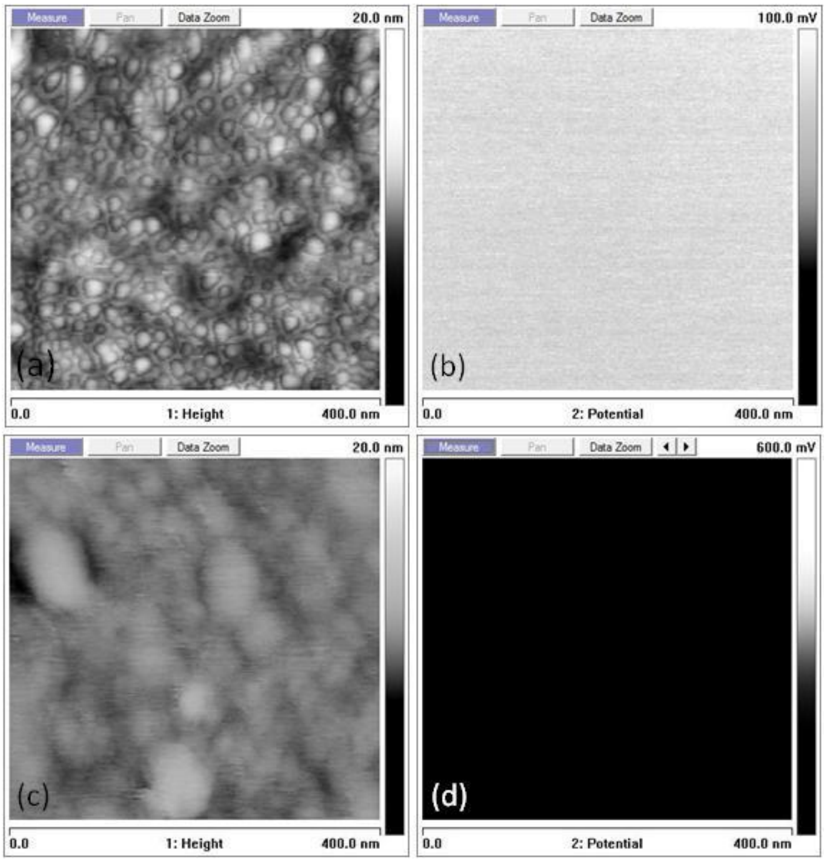

Figure 5.1. (a) AFM image of approximately 1 day old evaporated Au on glass and (b) corresponding contact potential differnce (CPD) image and (c) AFM image of approximately 1 week old evaporated Au on glass and (d) corresponding CPD image.

Figure 5.1 (c) and (d) show AFM and CPD images respectively of the same Au surface approximately 1 week after deposition. A clear difference is observed in both surface morphology and CPD, where the average CPD over the surface is -240.71 mV

The AFM images reveal the stark contrast in surface morphology over the 1 week period, highlighting the susceptibility of Au to surface contaminants when stored in ambient conditions. Figure 5.2 shows the CPD of both samples shown in Figure 5.1 (b) and (d) as a function of the area averaged X axis scan direction, and clearly shows the contrast in CPD between the two samples. The area averaged X axis value represents each X axis data point as the mean of the total Y axis values associated at a single X-axis data point.

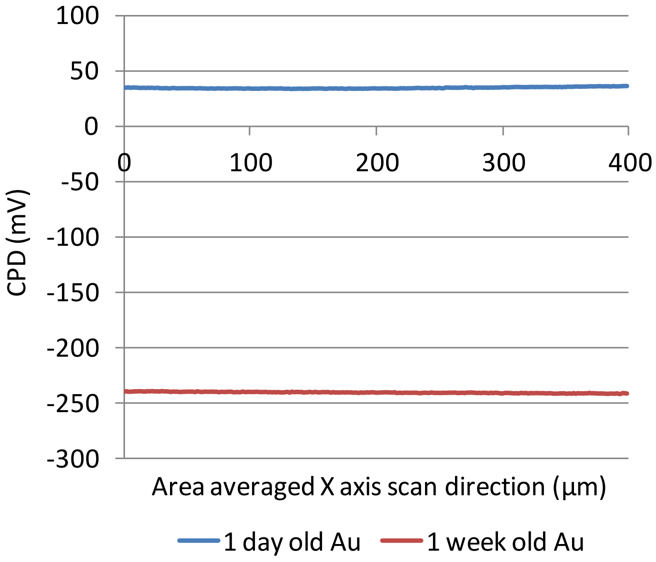

Figure 5.2. Area averaged X axis scan direction vs. CPD of both Au sample shown in Figure 5.1

Au is known to be highly oleophilic, therefore the aggregation of hydrocarbons and formation of aurophilic complexes may be responsible for the time dependent changes in both surface morphology and CPD observed above. This clearly demonstrated that the Au surface was unstable and as such, unsuitable for use as a work function calibration standard for SKPM conducted in ambient conditions.

In light of these results, an alternative reference material; HOPG was examined. Figure 5.3 (a) and (b) respectively show an AFM image and corresponding CPD image of a HOPG reference sample, Figure 5.3 (c) and (d) show analogous AFM and CPD images of the same sample approximately 1 week later. The AFM images reveal the individual graphite sheets, where for HOPG the angular spread is < 1°, this is reflected in the z-axis, where a 50 nm range (ie. ± 25 nm) is observed. Figure 5.3 (b) and (d) reveal a uniform featureless CPD over both 10 × 10 µm areas, and crucially good reproducibility over the stated timeframe.

Figure 5.4 shows the CPD as a function of the area averaged x-axis observed in Figure 5.3 (b) and (d), viewing the result in this format shows a CPD range for the first measurement (HOPG1) between -306.25 and -326.26 mV, with an average value of -317.01 mV and CPD range for the second measurement (HOPG2) between -302.26 and -317.79 mV with an average value of 307.76. Good agreement between these measurements indicated that the HOPG could be successfully used to calculate absolute Φ values for unknown samples.

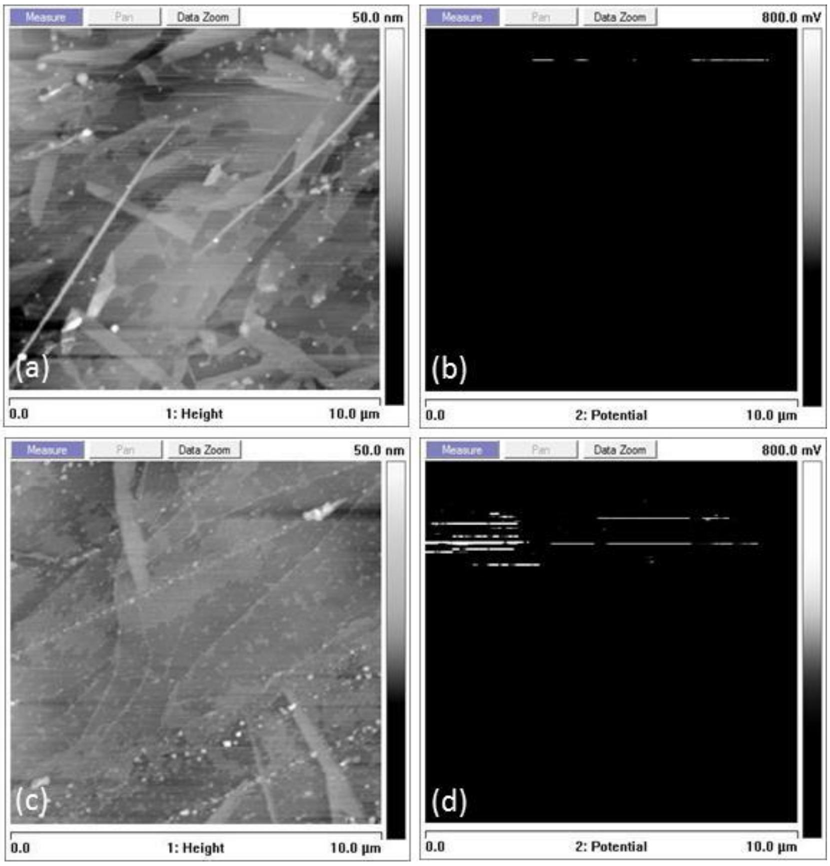

Figure 5.3 (a) AFM image of HOPG surface and (b) corresponding CPD image and (c) AFM image of HOPG surface and (d) corresponding CPD image approximately 1 week after (a) and (b) were measured

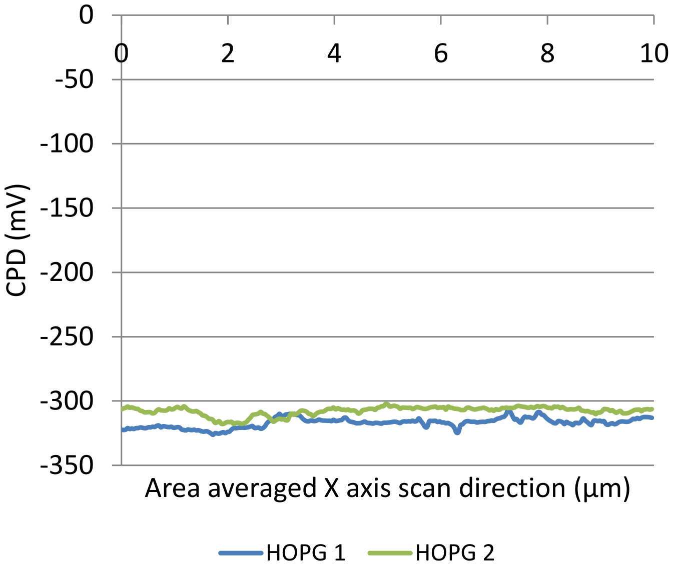

Figure 5.4. Area averaged X axis scan direction vs. CPD of HOPG measurements shown in Figure 5.3.

Equation [5.1] shows the relationship between Φ and CPD, where $e = 1.6 \times 10^{-19}$ C. This shows that a reference Φ value and the measured ΔCPD, can be used to calculate Φ for an unknown sample.

$$\Delta\Phi = e\Delta\text{CPD} \qquad [5.1]$$

The known Φ value of HOPG (4.48 eV) and the measured AFM tip – HOPG CPD (-317.01 mV – HOPG1 value) allowed the Φ of the probe tip to be calculated:

$$\Phi_{\text{tip}} = \Phi_{\text{HOPG}} + \text{CPD} \qquad [5.2]$$

This yielded a Φ_{tip} value of 4.16 eV, and effectively calibrated the AFM tip, allowing for absolute Φ measurements to subsequently be made [143]:

$$\Phi_{\text{sample}} = 4.48 + \text{CPD}_{\text{HOPG}} - \text{CPD}_{\text{sample}} \qquad [5.3]$$

Table 5.1 summarises the CPD values recorded for each of the materials examined.

Reference material	**CPD (mV)**
1 day old Au on glass	34.61
1 week old Au glass	-240.71
HOPG1	-317.01
HOPG2	-307.76

Table 5.1. Summary of calibration values

5.1.2 A summary of p-type doping in CdTe

The incorporation of Arsenic (As) into bulk CdTe thin films for PV solar cells was investigated by Rowlands *et al.* [127]. This study used secondary ion mass spectroscopy (SIMS) depth profiling to determine the As dopant concentration in a series of devices where the As precursor; tris(dimethylamino)arsine (TDMAAs) partial pressure was varied from 3×10^{-9} to 1×10^{-6} atm. The detection limit for As was 1×10^{16} atms cm^{-3}. Table 5.2 summarises five CdS/CdTe np (no p^+) structures where the TDMAAs partial pressure varied between 6 ×

10^{-8} and 1 × 10^{-6} atm, yielding As dopant concentrations between 1 × 10^{17} and 2 × 10^{19} atms cm^{-3} respectively. This study determined that As incorporation into the bulk CdTe absorber layer followed second-order kinetics and that the formation of complex As dimers were the significant rate limiting step.

	Sample				
	1	**2**	**3**	**4**	**5**
TDMAAs PP (atm)	6 × 10^{-8}	1 × 10^{-7}	3 × 10^{-7}	5 × 10^{-7}	1 × 10^{-6}
As conc. (atms/cm^{-3})	1 × 10^{17}	4 × 10^{17}	2 × 10^{18}	6 × 10^{18}	2 × 10^{19}

Table 5.2. Summary of partial pressures (PP) used for series of As-doped CdTe devices and As concentrations determined from SIMS depth profiles.

The following study expands on these results and examines how As doping alters the Fermi level and correspondingly the work function of the CdTe layer.

Equation [5.4] gives the Fermi level energy for a p-type semiconductor, where E_v is the valence band energy level, k is Boltzmann’s constant, T is temperature, N_v is the effective density of states in the valence band, and N_A is the acceptor dopant density (p-type dopant density).

$$E_{fp} = E_v + kTln\frac{N_v}{N_A} \tag{5.4}$$

This shows that as the p-type dopant concentration (N_A) increases, E_f is shifted down in energy towards the valance band. Figure 5.5 expands this concept to show the relationship between p-type doping, work function (Φ) and contact potential difference (CPD) as expected in SKPM studies on p-type doped CdTe.

As the p-type dopant concentration increases, the Fermi level is expected to decrease. This will lead to a corresponding increase in Φ. This theory therefore indicates that, with increasing As doping the CdTe Φ will increase. This is illustrated in Figure 5.5 where p-type doping increases from sample $CdTe^1$ to sample $CdTe^5$.

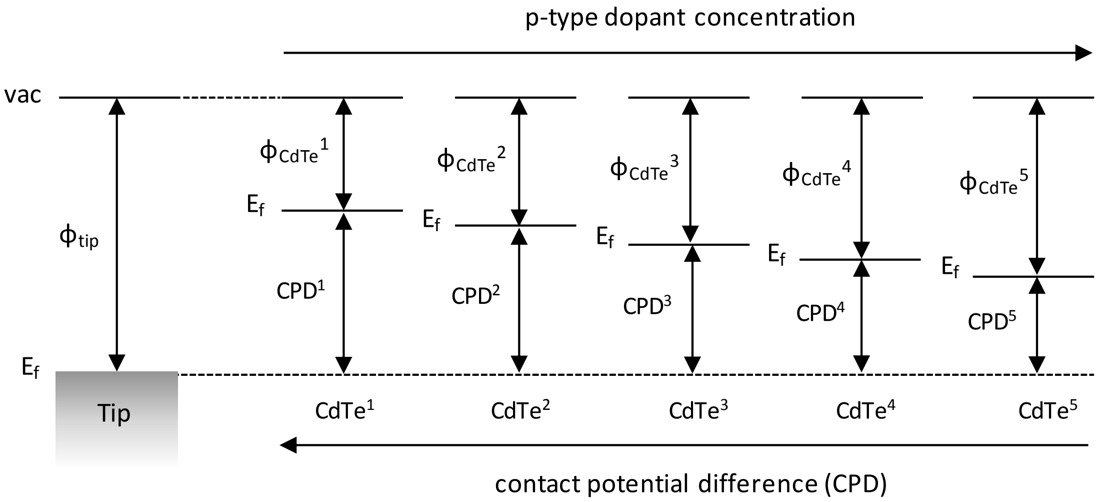

Figure 5.5. Schematic showing the changes in contact potential difference and CdTe work function (Φ) as a function of p-type dopant concentration.

5.1.3 *SKPM on As-doped CdTe*

Figures 5.6 (a) – (e) show AFM images of samples 1 – 5 respectively, where Figure 5.7 (a) – (e) show the corresponding simultaneously recorded CPD images of the same samples at the same location. The topographic images show a typical polycrystalline CdTe surface, where some inter-sample variation in grain size is observed due to differences in the position of the sample with respect to the precursor flow in the deposition chamber. Large grains and a thick CdTe layer are typically observed upstream of the precursor flow and correspondingly, small grains and a thin CdTe layer are observed downstream. Other than this variation the AFM images reveal no observable trend. Conversely, the CPD images show a striking trend, where the CPD is clearly observed to decrease with increasing As concentration. This interpretation is drawn from the increased darkening observed in each CPD image (ie. (a) is lightest and (e) is darkest).

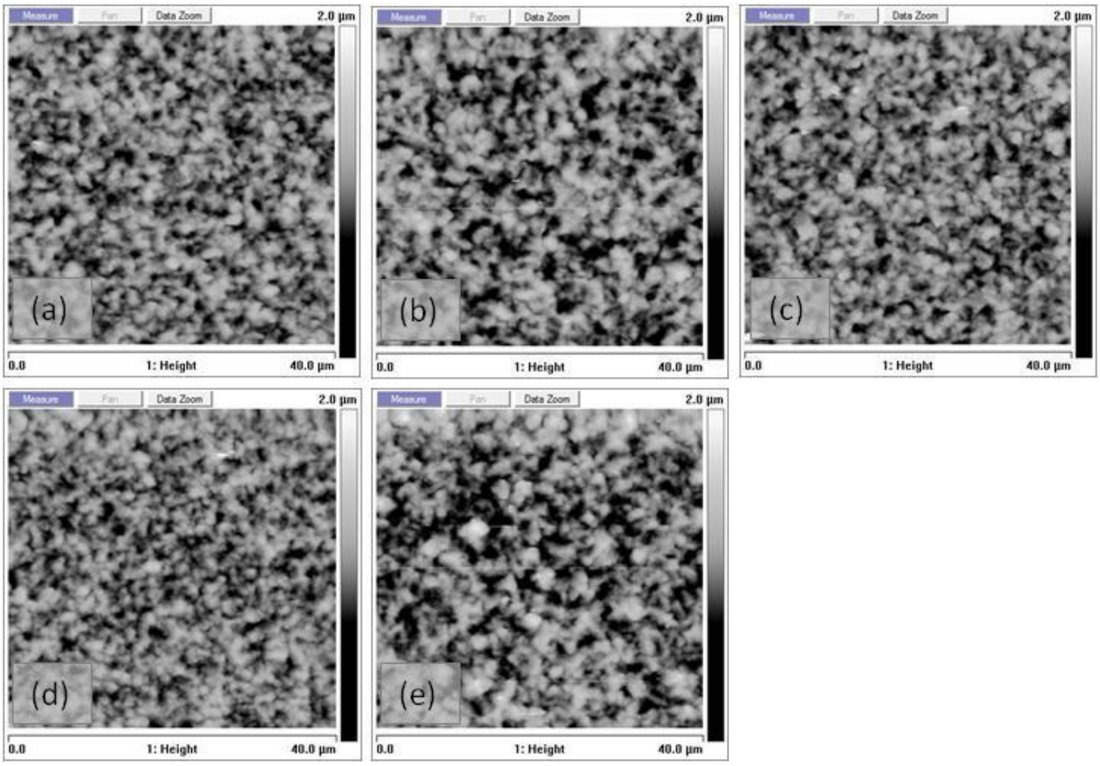

Figures 5.6 (a) - (e) 40 × 40 µm AFM images of samples 1 - 5 respectively.

Each CPD image shows good uniformity over the scanned area, where some lighter regions in, for example, Figure 5.7 (a) indicate localised regions of increased CPD, and lower Φ. If the area averaged x-axis measurement of each CPD image is considered, this provides a clear indication of the CPD change as a function of As concentration. This is shown in Figure 5.8, and shows that, consistent with theoretical predictions, with increasing As concentration, the CPD is observed to decrease, corresponding to a downward E_f shift from sample 1 to sample 5.

These results provide an uncalibrated indication of the relative Φ of these As doped CdTe samples, to this effect, a conclusion can be drawn that the Φ incrementally increases from sample 1 to 5. Further analysis and the application of the calibrated values obtained in section 5.1.1 provide a means to calculate absolute Φ values for each of the As doped CdTe samples, (using Equation [5.3]).

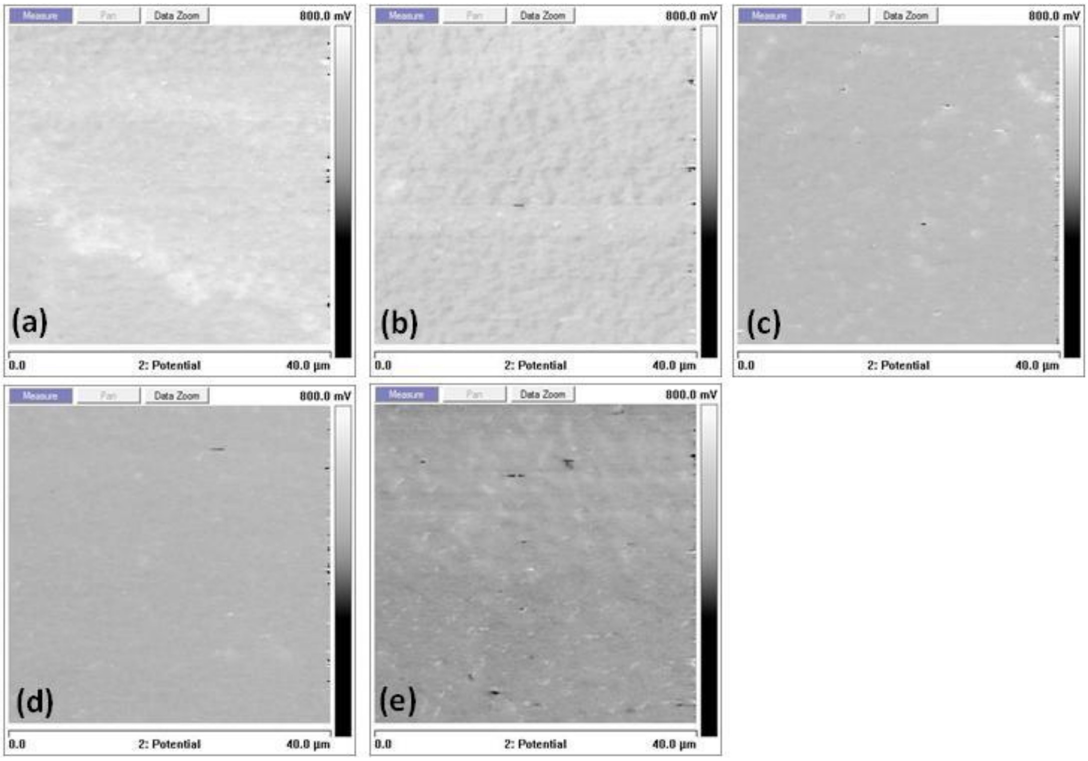

Figure 5.7 (a) - (e) CPD images of samples 1 - 5 respectively

Table 5.3 summarises the As concentrations observed in each of the 5 As doped CdTe samples, also summarised is the measured CPD of each of the 5 samples, calculated from the mean of the area averaged x-scan measurement shown in Figure 5.8. Furthermore, the calculated Φ values based on the tip calibration described above are shown. The calculated Φ values fall between 3.88 and 4.09 eV.

Sample	TDMAAs PP (atm)	As conc. (cm^{-3})	Mean CPD (V)	Mean Φ (eV)
1	6×10^{-8}	1×10^{17}	0.276	3.88
2	1×10^{-7}	4×10^{17}	0.244	3.91
3	3×10^{-7}	2×10^{18}	0.162	4.00
4	5×10^{-7}	6×10^{18}	0.121	4.04
5	1×10^{-6}	2×10^{19}	0.067	4.09

Table 5.3. Summary of As concentrations in CdTe samples, mean CPD calculated from area averaged x-axis values found in Figure 5.8 and calculated Φ values, where $\Phi_{CdTe} = \Phi_{tip} - CPD$ (Φ_{tip} = 4.16 eV).

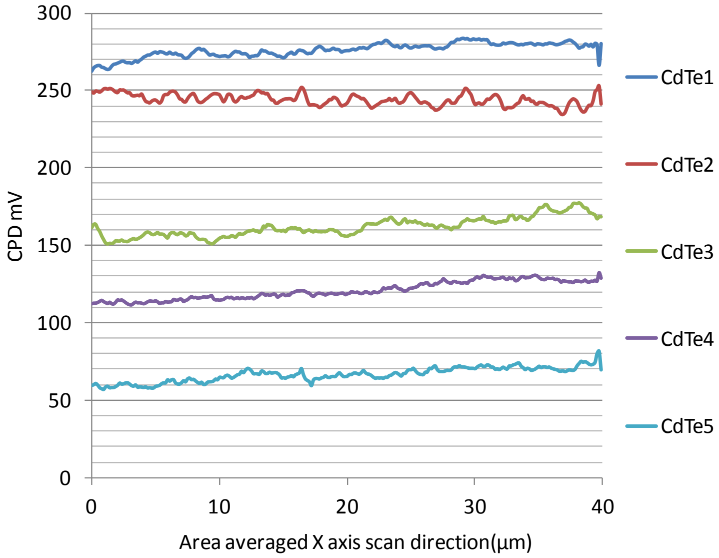

Figure 5.8. Area averaged X axis scan direction vs. CPD of samples 1 -5 as shown in Figure 5.7 (a) – (e).

These results show that over an As doping range covering two orders of magnitude a relatively small change in CPD, from 0.067 to 0.272 V is observed, correlating with absolute Φ values between 4.09 and 3.88 eV respectively. Figure 5.9 and Equation [5.5] show a linear decrease in CPD when plotted against the logarithmic As concentration, [As].

$$CPD = -0.041 \ln[As] + 1.88 \tag{5.5}$$

This follows a corresponding non-linear increase in Φ, where $\Phi_{CdTe} = \Phi_{Tip} - CPD$. Figure 5.10 summarises the calibration information and the five CdTe samples examined in terms of E_f band alignment. This shows how As doping in CdTe shifts the E_f, and correspondingly, the measured CPD and the sample Φ.

Again, these results are consistent with the predicted downward shift in E_f with increased p-type doping. Although, the absolute Φ_{CdTe} values are low when compared to literature values where Φ_{CdTe} is typically quoted between 5.5 and 5.9 eV [74, 144]. This observation highlights the difficulties of accurately determining absolute bulk Φ values using the SKPM technique, where ambient measurement conditions likely lead to the formation of surface states and surface band bending. This is consistent with the assumption that the CdTe surface is susceptible to contamination and/or the formation of surface oxides which would lead to such surface band bending.

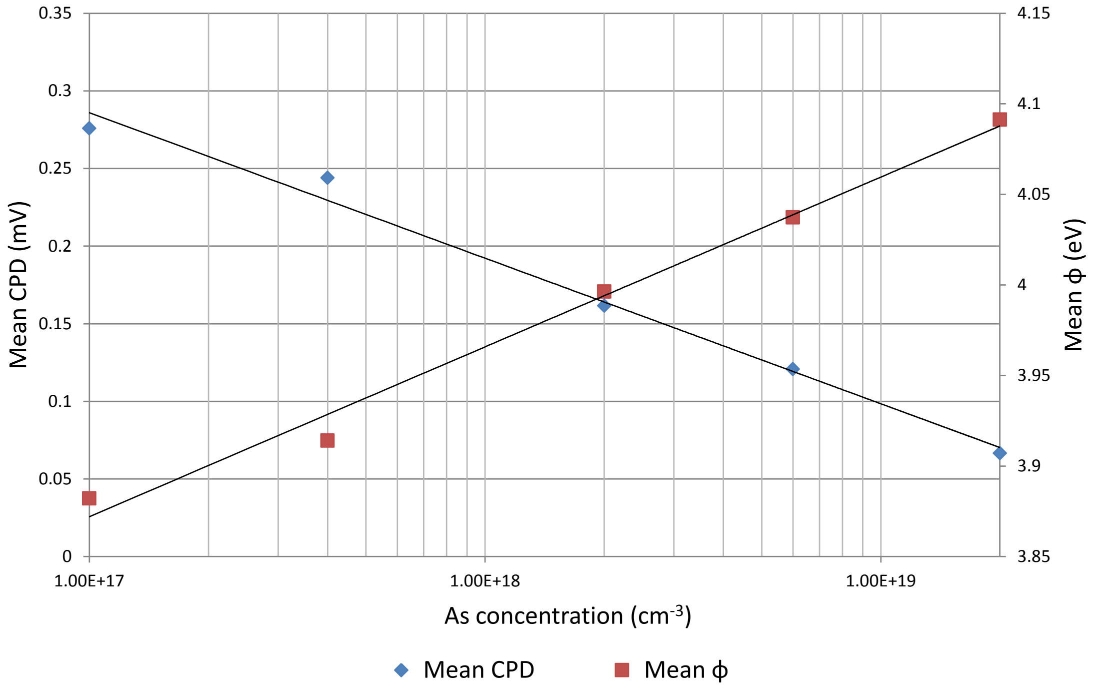

Figure 5.9. Plots of As concentration (cm^{-3}) vs. mean CPD (V) and mean Φ (eV)

This uncertainty may explain the relatively large discrepancy between measured values and literature values. Notwithstanding, the ability to successfully characterise the relative E_f trends among this series of p-type doped materials is clearly demonstrated.

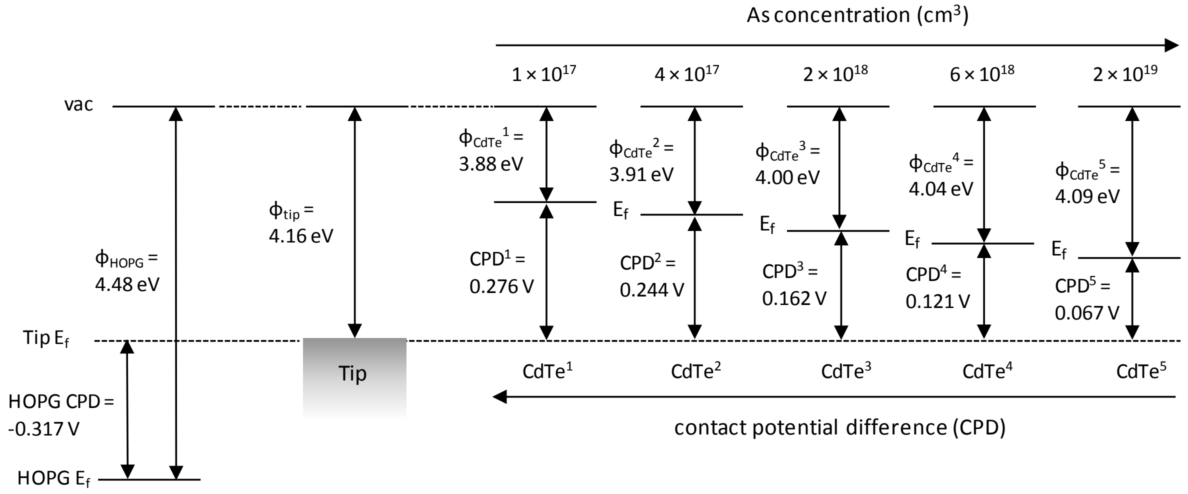

Figure 5.10. Band allignment diagram showing E_f of HOPG and CdTe relative to the AFM tip, and Φ values for each of the 5 CdTe samples, the HOPG reference material and the AFM tip (not to scale).

5.1.4 SKPM on platform MOCVD devices

The previous investigation focused on the As doping levels in bulk CdTe layers in a series of CdS/CdTe np structure PV devices. The following study examines the CdS/CdTe npp$^+$ structure, where in addition to the As doping in the bulk CdTe layer, a 250 nm p$^+$ back contact layer (BCL) is deposited onto the CdTe back surface. This is proposed to enhance back contact conductivity and improve the ohmic behaviour of the CdTe back surface-back contact interface [69]. The npp$^+$ CdS/CdTe structure (sample A) is compared to an np CdS/CdTe structure (sample B) and an undoped CdS/CdTe structure (sample C). All devices were grown onto 120-160 nm thickness 5-15 Ω/□ ITO on 50 × 75 mm boro-aluminosilicate substrates. Table 5.4 summarises the devices used for this study.

Sample	**240 nm CdS**	**2000nm CdTe**	**As doping**	**CdTe p$^+$ BCL**	**CdCl$_2$**
A (npp$^+$)	✓	✓	✓	✓	✓
B (np)	✓	✓	✓		✓
C (undoped)	✓	✓			✓

Table 5.4. Summary of layers for sample A-C

Figure 5.11 (a) – (c) show 10 × 10 μm^2 AFM topographic images of samples A-C respectively, and Figure 5.11 (d) – (f) show the corresponding CPD images for these samples. At increased magnification the detail of the CdTe back surface grain structure is clearly observed, where grain sizes are typically between 0.5 and 1.5 μm in diameter. Two key observations can be made with regard to the CPD images:

(a) As observed in the previous section, the effect of doping on the CPD images is immediately obvious, where sample A, the full npp$^+$ structure appears as the darkest image and conversely sample C, the undoped np structure the lightest. This reflects a relative change in Φ with respect to the AFM probe tip.

(b) The polycrystalline grain structure of each of the samples is causing clear changes to the measured CPD, where the grain boundary (GB) network in sample A is leading to an observable downward shift in localised CPD, this is also seen in sample B and C. Further analysis of this phenomenon will be presented and discussed later in this section.

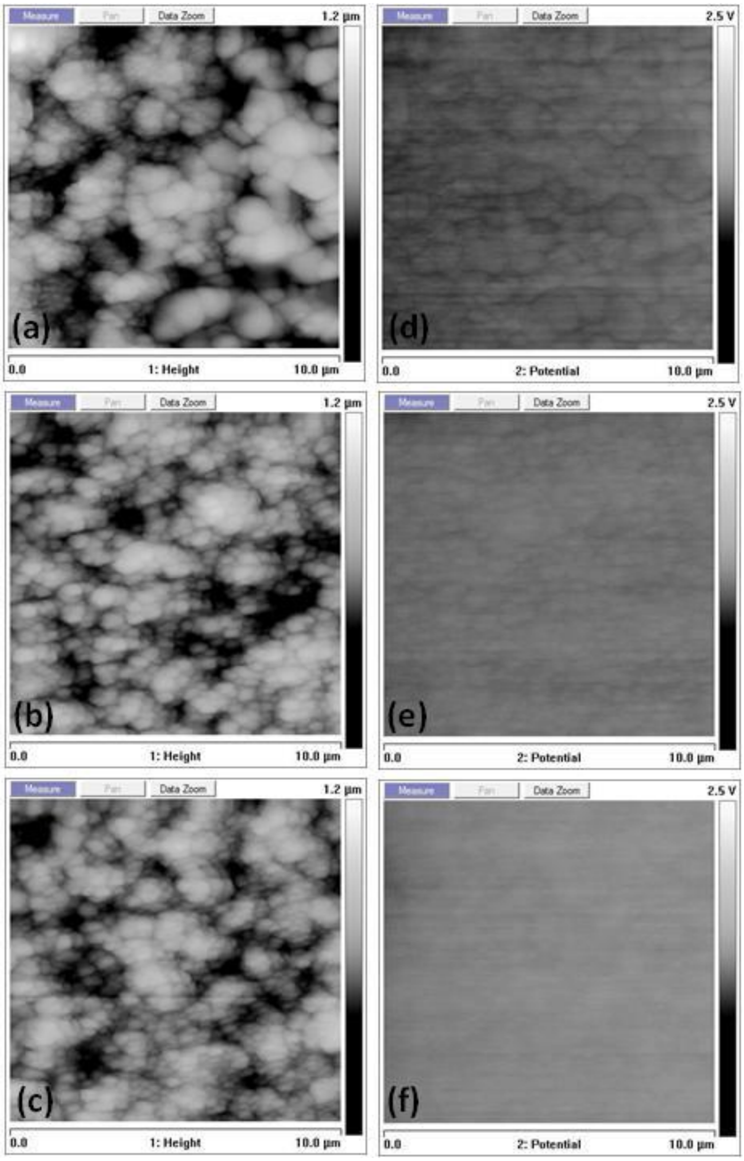

Figure 5.11 (a) - (c) AFM topographic images and (d) – (f) corresponding SP images of samples A-C respectively.

Figure 5.12 shows the area averaged x-axis scan position vs. CPD plotted for samples A-C. A trend is observed where the change in CPD is consistent with the p-type doping in the structures. The npp$^+$ and np structure both reveal negative CPDs, with mean values of – 0.124 and – 0.015 V respectively. The negative CPD indicates the $\Phi_{CdTe} > \Phi_{tip}$. Sample A reveals the largest Φ value among the 3 samples due to the highly doped p$^+$ BCL. Conversely, sample C the undoped sample shows a positive CPD, with a mean value of 0.076 V. This correlates with an increased E_f (higher than the tip E_f) and smaller Φ.

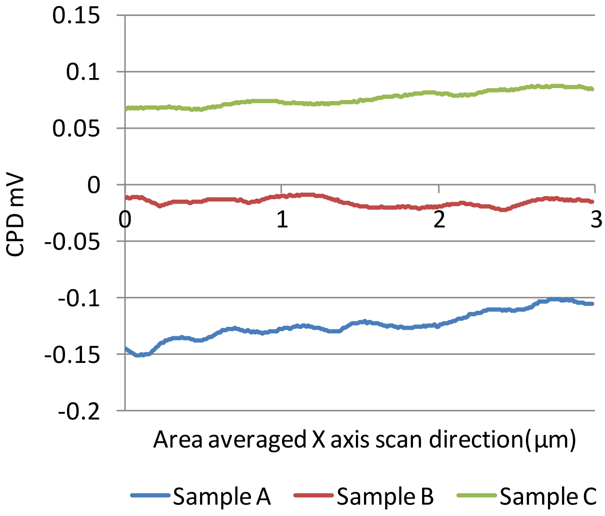

Figure 5.12. Area-averaged x-axis measurement vs. CPD.

Figure 5.13 shows a band alignment diagram highlighting the E_f in each of the samples A-C, where Φ_{CdTe}^{A} and $\Phi_{CdTe}^{B} > \Phi_{Tip}$ and $\Phi_{CdTe}^{C} < \Phi_{Tip}$. These trends are consistent with observations made in section 5.1.3, where increased p-type doping leads to increased Φ. It should be noted that some of the absolute Φ values calculated here should be directly comparable to those presented in section 5.1.3, where, sample A has a similar back surface doping profile as sample 5 (section 5.1.3) and sample B similar to sample 3 (section 5.1.3) although comparison reveals some disparity. This can be considered by the following:

(a) That observable changes in CPD and Φ have been reliably identified, and/or

(b) The difficulties in separating surface and bulk Φ values in ambient conditions (due to surface band bending) have led to the convolution of bulk/surface CPD values.

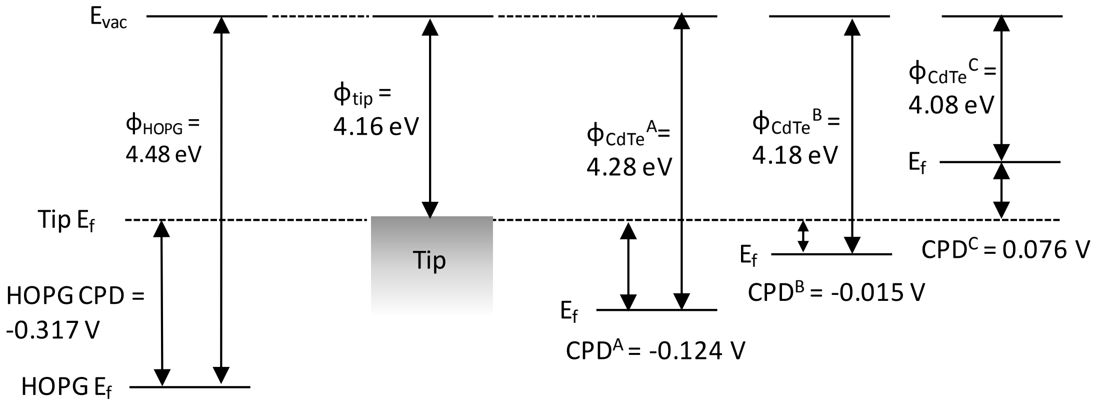

Figure 5.13. Band allignment diagram showing E_f of HOPG and samples A-C with respect to the tip E_f

Option (a) indicates that changes in CPD and Φ among samples 1-5 (section 5.1.3) and samples A-C are real and reflect the age of the two sample sets, where samples 1-5 were approximately 3 years old at the time of measurement and samples A-C were approximately 3 months old. The observed changes may therefore be related to sample age where the formation of a native oxide layer on the CdTe surface could be leading to changes in surface band bending and the measurable CPD. Option (b) highlights the difficulties associated with absolute Φ measurements made under ambient conditions. Nonetheless, these relative trends provide consistent and reliable evidence showing the effect of p-type doping in CdTe PV devices.

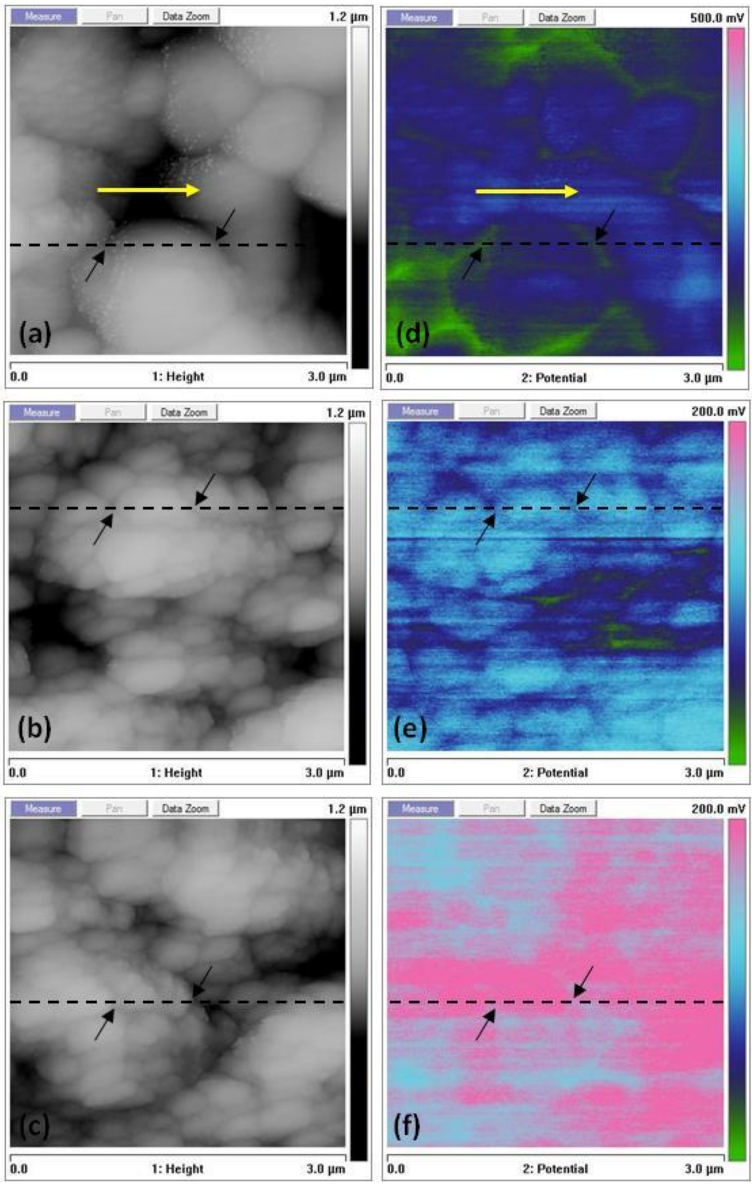

Figure 5.14. (a) – (c) 3 × 3 µm AFM topographic images and (d) – (f) corresponding SP images of samples A-C respectively.

Furthermore, high-resolution studies of samples A-C revealed subtle changes in the CPD at the GB's indicating localised changes in band bending at these locations. Figure 5.14 (a) – (c) show 3 × 3 μm topographical AFM images and (d) – (f) show their corresponding CPD images of samples A – C respectively.

The colour scale and style of each of the CPD images (Figure 5.14 (d) – (f)) has been set to optimise the contrast exhibited in each image. Therefore, it is necessary to note that the CPD scale range shown for sample A (Figure 5.14 (d)) is 500 mV (or – 250 mV to + 250 mV) and for samples B and C (Figure 5.14 (e) and (f) respectively) is 200 mV (or – 100 mV to + 100 mV).

The interleave mode employed by the SKPM system negates the convolution of CPD imaging and topographical related artefacts, to this end a lift height of 80 nm was used throughout this investigation, and any topographic interference with the CPD image is assumed to be negligible. Figure 5.15 supports this assumption showing a line scan taken at the position indicated in Figure 5.14 (a) and (d) (yellow arrow) where the topographic height varies significantly from 0 to – 240 nm (mean = -120.76 nm and σ = 60.19 nm) and the CPD shows only small variation (mean = -85.97 mV and σ = 9.26 mV) and no direct correlation with the observed changes in topographic height. This evidence adds credibility to the following discussion where small changes in localised CPD are considered.

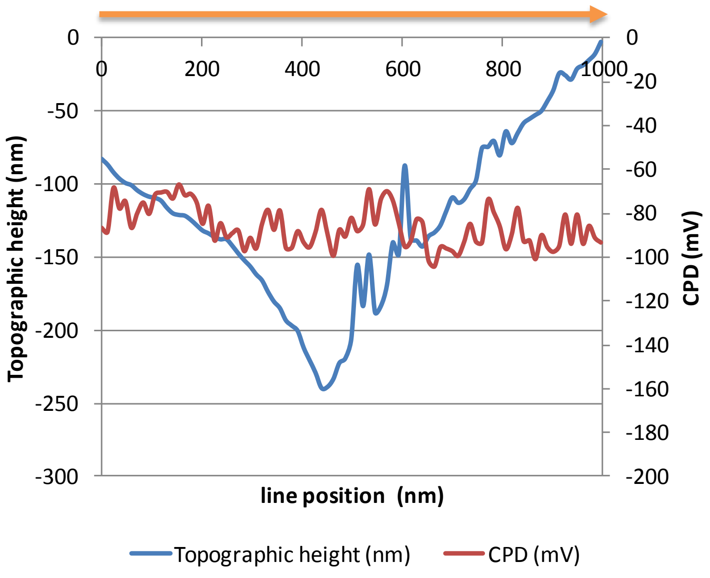

Figure 5.15. Topographic height and CPD vs line position as shown in Figure 5.14 (a) and (d)

Each topographic image clearly shows individual CdTe grains and an extensive grain boundary (GB) network. The corresponding CPD images show some significant correlations with these topographic features, where CPD imaging convolution can be assumed to be negligible as discussed above. Figure 5.16 shows 3 line scans taken at the positions indicated in Figure 5.14 (d) – (e) (dashed horizontal lines). The dashed circles in Figure 5.16 correlate with the positions indicated with black arrows in Figure 5.14 and show a localised shift in CPD at the GB's. Furthermore, the degree of shifting correlates with the p-type character of the sample, ie. sample A (npp$^+$) shows a shift of ~ 42 mV, sample B (np) shows a shift of ~ 30 mV and sample C (undoped) exhibits the smallest of ~ 24 mV. These values are derived from the vertical step height change at the positions indicated in each of the line scans shown in Figure 5.16.

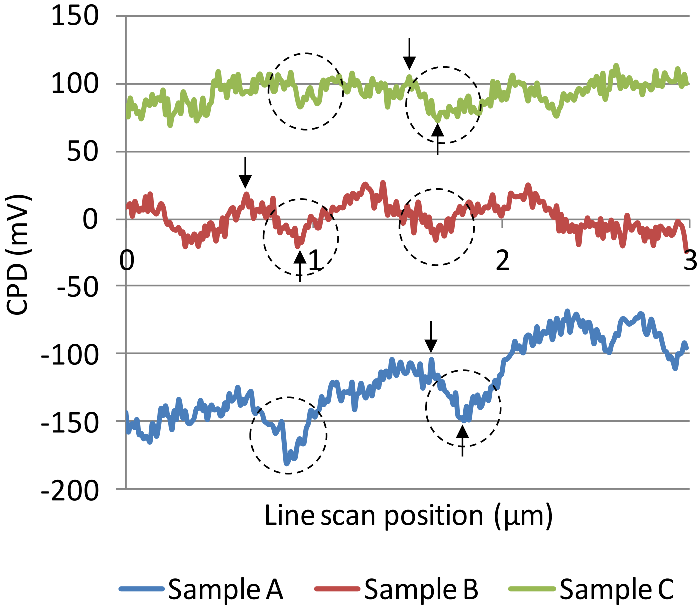

Figure 5.16. CPD line scans taken at positions indicated in Figure 5.14 (d) – (f). The CPD dips correspond to GB's in the topographic AFM image (labelled with arrows)

This indicates that some of the GB's are leading to localised shifts in CPD (NB. this is not always the case, as is seen in the example given in Figure 5.15). This indicates the segregation of As to the GB's, where an increased hole concentration leads to upward shifts in the CB and VB. Figure 5.17 (a) and (b) illustrates this effect where band bending at the GB's is proposed to reduce recombination by channelling minority carriers away from the GB. This suggests that the GB network is actively contributing toward PV cell performance by enhancing carrier separation and reducing carrier recombination.

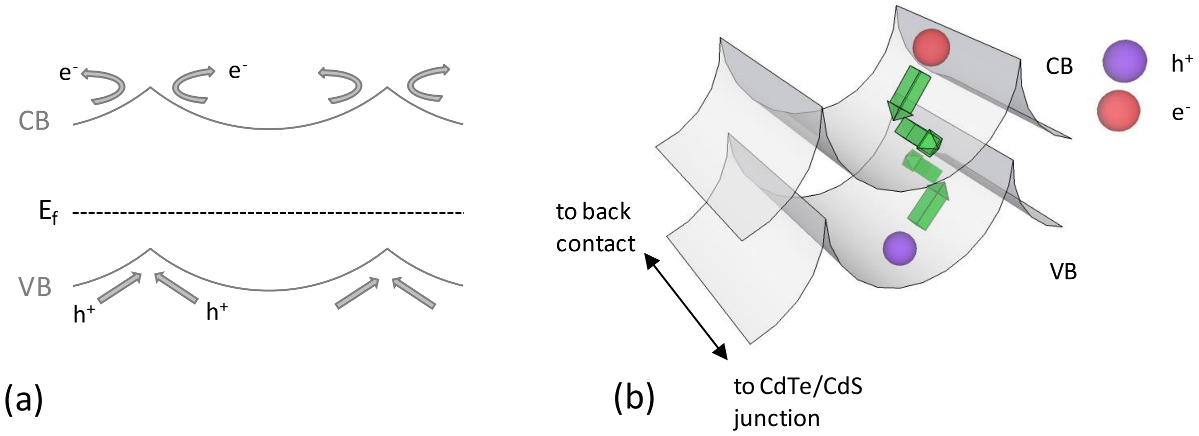

Figure 5.17. (a) Proposed localised band structure showing CB and VB bending at CdTe GBs and (b) Proposed GB conductivity model.

5.2 *Conductive probe atomic force microscopy (CAFM)*

5.2.1 *A CAFM current collection model*

Moutinho *et al.* [121] proposed that CAFM measurements can be considered in terms of a current collection cone extending laterally within the material, as shown in Figure 5.18. The lateral extension and shape of the cone is considered to depend on the resistivity and homogeneity of the sample; the cone diameter increasing with decreasing resistivity. Furthermore, the authors comment on the nature of the electrical contact between the CdTe back surface and the CAFM probe (a doped diamond coated Si tip), concluding that some rectification was observed at this interface. The following results are interpreted using a similar model, also considering the potential convolution of results arising from the tip/surface interface.

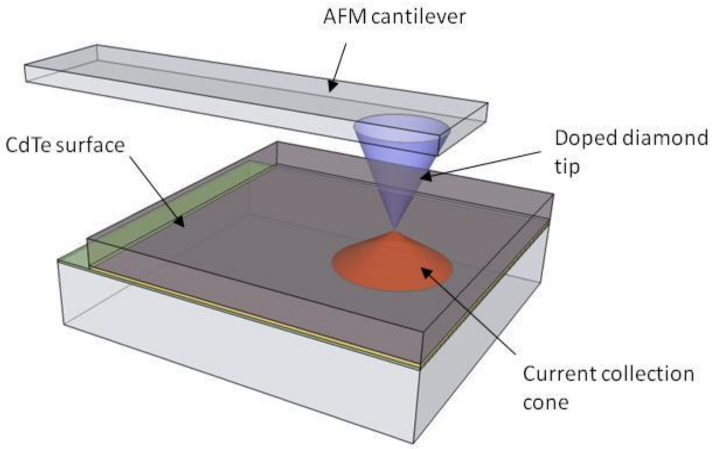

Figure 5.18. Schematic showing current collection cone in CAFM measurement

5.2.2 Current imprinting in CdTe

Figure 5.19 (a) shows a 20 × 20 μm AFM image of a baseline MOCVD CdTe back surface. Indicated at the centre of the image is a 10 × 10 μm area which had previously been examined in CAFM mode. Within this area Figure 5.19 (a) reveals a surface unchanged by the previous measurements and similar to the area outside this demarcation. Conversely, Figure 5.19 (b) shows the simultaneously recorded CAFM image and shows a striking hysteresis effect where the 10 × 10 μm area at the centre of the image shows a significant change in measured current.

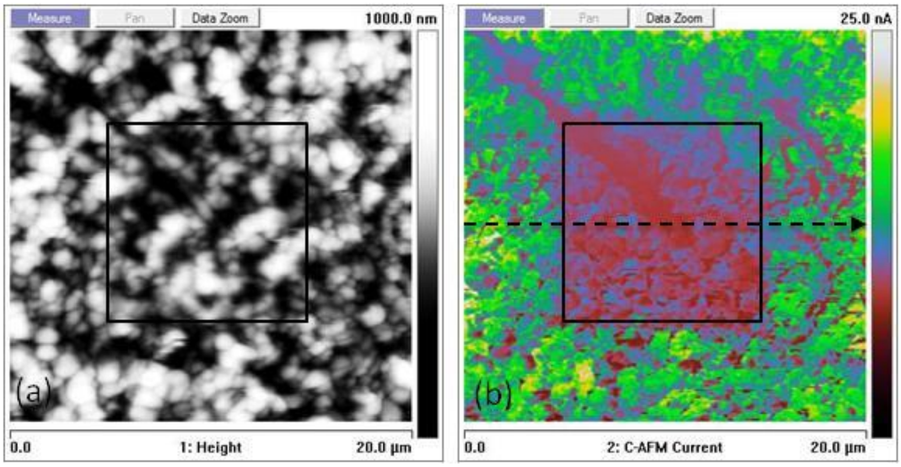

Figure 5.19. (a) 20 × 20 μm topographic AFM image of baseline MOCVD CdTe device and (b) corresponding simultaneously recorded CAFM image.

This is further visualised in the line scan shown in Figure 5.20 taken at the position indicated in Figure 5.19 (b) where a mean current of ~ 2.3 nA is measured between line position 0 – 4 μm and a mean current of ~ -3.0 nA between line position 5 – 13 μm.

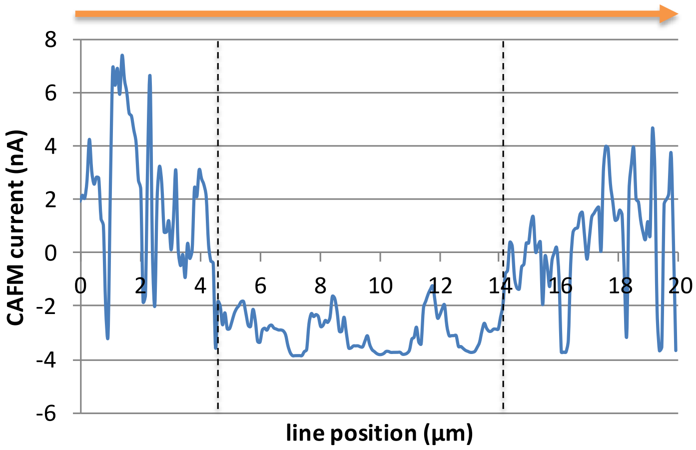

Figure 5.20. Line scan at position indicated in Figure 5.19 (b)

This phenomenon was also observed by Moutinho *et al.* [121] who ascribed this to the formation of an oxide layer, or the modification of an existing oxide layer citing similar observations made in biased AFM measurements of Si and GaAs. Alternatively, this observation may indicate that an applied bias is filling trap levels and a capacitance effect is occurring. This would also suggest that the current collection cone would narrow with increased applied bias and therefore lead to increased feature resolution. This corresponds to the observation that only the magnitude of the measured current changes with increased applied bias, and qualitative features do not; a phenomenon discussed in further detail in the following section.

5.2.3 Bias effects on CAFM imaging

Figure 5.21 (a) shows a 10 × 10 μm topographic AFM image of the area indicated in Figure 5.19 (a). Corresponding CAFM images taken at 1V increments between +1 and +5V biases are shown in Figure 5.21 (b) – (f) respectively.

It should be noted that in reverse bias conditions and when no bias was applied, it was not possible to successfully measure any CAFM current image. The filling of trap levels provides a probable explanation; where in reverse bias, increased recombination at active trap levels leads to an increase in resistance and a decrease in the recoverable current signal. The requirement for a high forward bias also indicates a barrier at the tip/surface interface, where a rectifying electrical junction is formed and a large bias is required to overcome the barrier at this interface. This would be related to the high resistivity of the CdTe and the difficulty in forming a good electrical contact with the doped diamond tip. The use of alternative metallic tips found further difficulties in achieving and maintaining a good electrical contact and consistently yielded poor CAFM image resolution.

Figure 5.21 highlights the increased current image ‘resolution’ that was achievable using increased forward biasing, where only the magnitude of the measured current changes. This indicates that the biasing is simply amplifying the contrasts observed in the images and not contributing to the observable spatial variations in collected current. This is perhaps most clearly exhibited at the GBs where the network appears lighter (in grayscale terms) with increased forward bias; an observation that will be discussed in further detail in section 5.2.4.

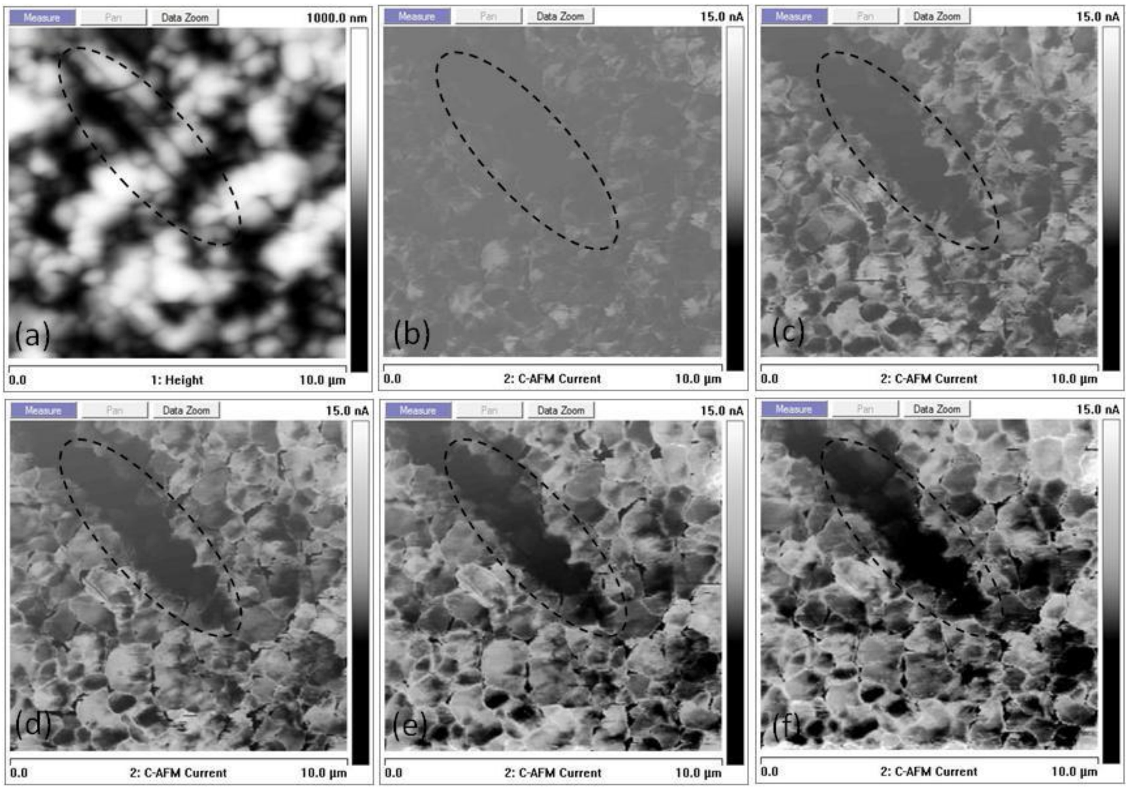

Figure 5.21 (a) 10 × 10 µm topographic AFM image of the region indicated in Figure 5.19 (a) and corresponding CAFM images at (b) +1V (c) +2V (d) +3V (e) +4V and (f) +5V.

Furthermore, the CAFM images in Figure 5.21 reveal an interesting feature, which is only hinted at in the topographic AFM image. As circled in Figure 5.21 (a) a series of GBs form two parallel and continuous lines at an approximately 45° angle. This may indicate a region where growth templating has taken effect; where a scratch on the substrate has led to subsequent growth defects in the deposited layers. The CAFM images reveal this growth anomaly is not electrically benign, and has led to a unique current collection region, in terms of both uniformity and magnitude when compared to the remaining scan area. These spatially different regions are likely related to either:

(a) Lateral variations in the contact between the tip and CdTe surface, and, or
(b) Changes in the electrical properties of the CdTe grains and GBs at the spatially resolved locations indicated.

The reproducibility (albeit at varying biases) of the CAFM images and the identification of the highlighted anomaly in Figure 5.21 (b) – (f) indicates that this is a change in the electrical properties of the CdTe, where an observable topographic feature is consistently leading to a change in measured CAFM current.

5.2.4 Grain boundary effects

Localised conductivity changes are further exhibited at the CdTe GBs. Figure 5.22 (a) and (b) respectively show a 4 × 4 µm AFM image and corresponding CAFM image recorded at the location indicated in Figure 5.22 (c) (CAFM image presented in section 5.2.3 (Figure 5.21 (e))). A modified colour scale highlights the GB network conductivity contrasting from bulk grain conductivity.

The contrast in terms of conductivity, between the GB network and the bulk grains, as well as some intra-grain variations in current collection is clearly illustrated. Figure 5.23 shows a line scan measured at the position indicated in Figure 5.22 (b). This line intersects a series of 5 GBs which are indicated by arrows; as shown in Figure 5.23 these correspond with peaks in current and reflect the full GB network where a similar trend is observed (indicating a genuine electrical property of the GB network). Conversely, the bulk grains exhibit a variety of electrical characteristics.

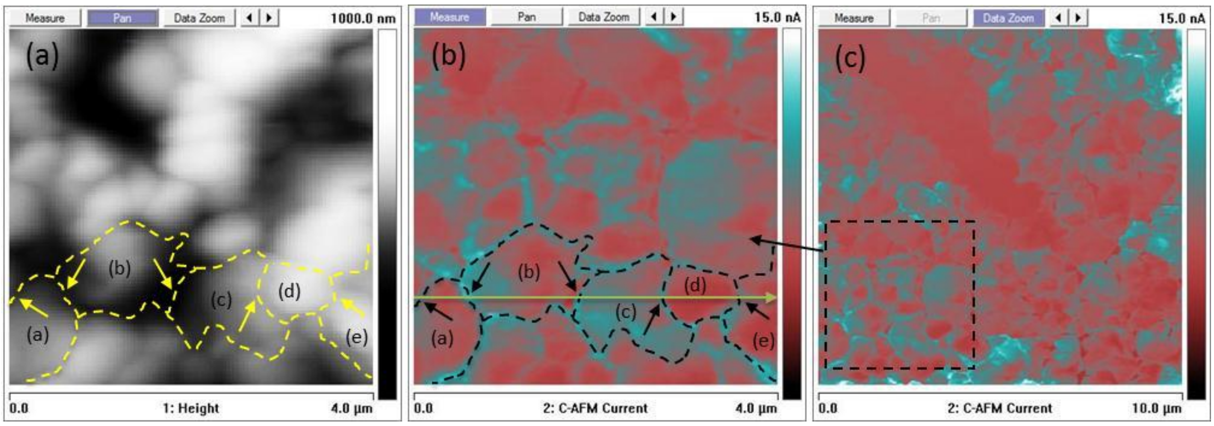

Figure 5.22 (a) 4 × 4 µm AFM image and (b) 4 × 4 µm CAFM image both taken recorded at the position indicated in (c) a 10 × 10 µm CAFM image, measured at +4V. This image is identical to Figure 5.21 (e) with an alternative colour scale to highlight the contrast between grain and GB conductivity.

Figure 5.23 also reveals the conductivity characteristics of several grains, where the GBs have been demarcated with black dashed lines and labelled (a) – (e). Both inter-grain and intra-grain variability is observed, and careful interpretation is required. The differences in current measurement could again either reflect the quality and nature of the tip/surface electrical contact and/or changes in the electrical properties of the grains, and indeed, changes within single grains.

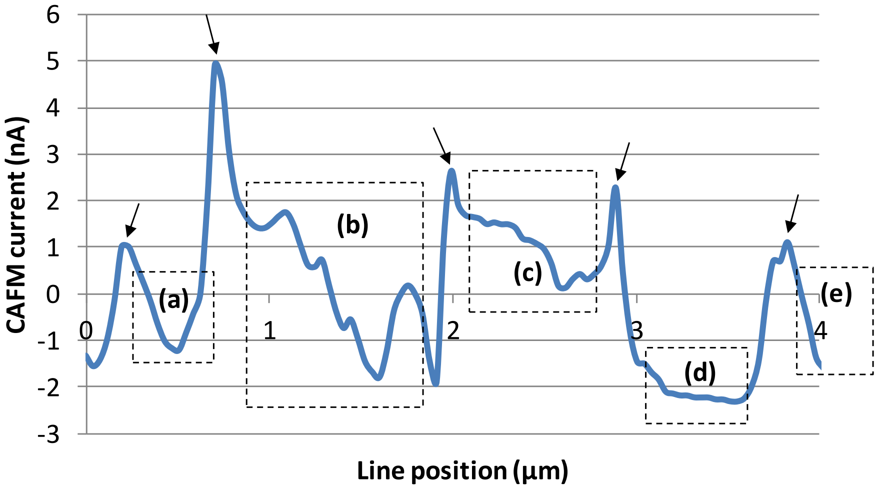

Figure 5.23. Line scan measured at the location indicated in Figure 5.22 (b)

The following interpretation assumes that a combination of both factors is determining the observable changes. This is based primarily by considering the position of the CdTe E_f in relation to the tip E_f and the nature of the barrier formed between the AFM tip and the CdTe surface. This barrier height will be sensitive to the p-type dopant concentration and therefore the CAFM measurement will reflect both this barrier height and the CdTe E_f.

In the bulk grain region labelled (a) in Figure 5.22 the current is observed to change relative to the neighbouring GB. The effect of localised changes in the GB E_f leads to a subtle and gradual conductivity change between the bulk grain and GB indicating this GB conductivity is not entirely limited to the GB, but extends to a limited degree within the grain interior. This corresponds with the cone shaped current collection area where the current image reflects not just the surface but also bulk conductivity.

Grain (b) shows high intra-grain variability, where the measurable current is shown to be laterally variable within the confines of a single CdTe grain. Grain (c) exhibits a current analogous to the GBs, highlighting inter-grain variability, and grains (d) and (e) follow a trend similar to grain (a) where current is observed to change relative to the GBs. Grain (d) as illustrated in Figure 5.23 (box (d)) is found to exhibit relatively small intra-grain variability.

These CAFM results indicate a mechanism where the measurement of bulk grain and GB conductivity is very sensitive to the CdTe E_f. As discussed previously, any localised variations in As concentration will lead to a E_f shift, this will also determine the tip/surface barrier height and the conductivity of the CdTe (as measured using the CAFM technique).

Figure 5.24 (a) and (b) exemplifies the tip/surface barriers encountered at low ($CdTe^1$) and high ($CdTe^2$) p-type regions respectively. Figure 5.24 (a) shows that a lower p-type region leads to a minority carrier barrier, Φ_B^1 at the tip/surface interface. This barrier is eliminated (Φ_B^2) at more p-type regions where the As concentration is higher (GBs), as shown in Figure 5.24 (b).

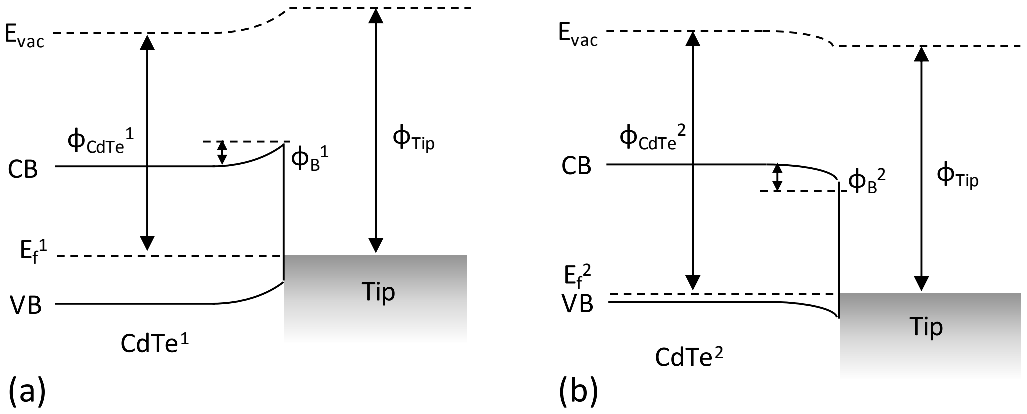

Figure 5.24 Band diagrams showing tip/surface interface and band bending at (a) a low As concentration region and (b) a high As concentration region.

This localised change in the barrier height at GBs associated with the Fermi level of the CdTe corresponds with observations made using the SKPM technique, where band bending at GBs was proposed to reduce carrier recombination by channelling minority carriers away from the GBs.

6 Conclusions and Future Work

This final chapter will summarise the key highlights and experimental findings described in this thesis. Furthermore, recommendations for future work will be discussed. This will include further potential LBIC instrument development and the expansion of the presented studies to gain additional LBIC and SPM derived insights into the behaviour and characteristics of MOCVD deposited CdTe, and indeed other PV materials and devices.

6.1 Conclusions

6.1.1 Laser beam induced current (LBIC) measurements

A triple wavelength LBIC system has been introduced for the primary purpose of producing spatially resolved photocurrent measurements on MOCVD deposited CdTe thin film photovoltaic solar cells. The triple wavelength approach to LBIC measurements has yielded unparalleled spatially resolved information, revealing the intricate inter-dependence of the component thin film layers found in CdTe based PV devices, in terms of incident light transmission, absorption and photogenerated carrier collection.

The development of the LBIC instrument described in chapter 3 provided the basis for these successful measurements where the addition and/or modification of both hardware and software components amounted to substantial improvements in the instruments capability. These included the addition of the following hardware components:

6. PTI IQ-series 405 nm diode laser
   The wavelength of the blue laser relative to the spectral response of $Cd_{1-x}Zn_xS/CdTe$ *thin film solar cell enabled the spatially resolved transmission (and absorption) characteristics of the window layer and its effect on device performance to be successfully captured.*
7. Orlin VTS-1 precision manual z-translation stage
   This provided easy and reliable adjustment of the sample z-height (relative to the microscope objective) ensuring the accurate adjustment of the focal point of the

incident laser beam. This was found to be a critical consideration enabling improved spatial resolution of the LBIC measurement.

8. Custom-built multi-contact device mounting platform

   The incorporation of a flexible and multiple contact sample mounting platform ensured that the instrument could record LBIC measurements on relatively large sample areas (up to 25 × 25 mm^2 per scan area on up to 50 × 75 mm^2 samples) and over multiple contacts simultaneously.

9. Ophir BeamStar FX 33-HD laser beam profiling camera

   The beam profiling camera became a useful ex-situ tool during the positional optimisation of the beam guiding optics, providing a good measurement of the Gaussian characteristics and 1/e^2 beam width of the incident beam during this construction phase.

10. PTB-calibrated Si photodetector

    This component ensured the successful calculation of the incident beam irradiance (W/m^2), photon flux (photons s^{-1} A^{-1} λ^{-1}) and laser wavelength dependent penetration depths ($\delta_p = 1/\alpha$).

Software amendments also included laser control and the full integration and modulation of the laser switching with the translation stage and signal recovery systems ensuring the laser could be switched synchronously with both the LBIC signal recovery and the translation stage step motion.

The LBIC instrument was used to comprehensively characterise non-uniformities in $Cd_{1-x}Zn_xS$ layers incorporated into CdTe based thin film photovoltaic solar cells. This study found that $Cd_{1-x}Zn_xS$ layers with highly non-uniform thickness distributions between 50 and 300 nm when incorporated into CdTe devices produced a characteristic LBIC response. Using the triple wavelength LBIC system, the contributions from individual layers within the structure could be identified and interpreted. It was found that in cell regions which exhibited high blue LBIC response, blue absorption in the window layer was very low; an observation corresponding with localised regions of very thin $Cd_{1-x}Zn_xS$. These regions were also found to correspond with regions of reduced LBIC response at longer wavelengths, where typically (in spatially uniform devices) high CdTe absorption and carrier generation and collection at these wavelengths was consistent with the spectral response of the device. The percentage area covered by these localised regions of poor photoresponse, where high blue and low red and IR LBIC response were observed were found to correlate with the device' open-circuit voltage (V_{oc}). This observation was explained by localized variations in carrier recombination impacting minority carrier lifetime (τ), where a drop in τ leads to an increase in the reverse saturation current (I_s) and a reduced V_{oc}. This conclusion implied that in regions where $Cd_{1-x}Zn_xS$ was thin a more defective depletion region in the CdTe was formed, yielding a region with a higher recombination rate.

Furthermore, the shunt resistance (R_{sh}) loss contribution to overall cell performance was found to be independent of the $Cd_{1-x}Zn_xS$ thickness distribution. This was explained by considering a model where each contact was compartmentalised into a number (n), of photo active regions, or ‘micro-cells’, where n was dependent on the step increment of the LBIC instrument. The model showed that the fill factor (FF) contribution to the cell efficiency loss could be explained by the moderate to high clustering of shunted microcells. This corresponded with the observation in high resolution LBIC measurements that pin-holes (responsible for producing shunted microcells in this model) were prevalent in regions of both thick and thin $Cd_{1-x}Zn_xS$ and CdTe.

Photoresponse losses associated with back surface contamination were also identified using the triple wavelength LBIC measurement, where EDX measurements were used to confirm and identify the origins of the contamination.

The effects of quantum dot luminescent down-shifting (QD-LDS) layers incorporated into $Cd_{1-x}Zn_xS$/CdTe PV devices was also investigated using the triple wavelength LBIC technique. Using the 405 nm laser for the initial LBIC measurements, the isotropic emission of the QDs was observed to increase the overall lateral carrier collection area and produce a net increased LBIC response at this wavelength when compared to LBIC measurements on the same device without the QD-LDS layer. This corresponded with external quantum efficiency (EQE) measurements, where increased EQE spectral response was observed between 300 and 450 nm in the device incorporating the QD-LDS layer compared to the device without the QD-LDS layer. Further scattering at longer wavelengths was observed to marginally increase the observable contact area, but with loss of overall cell performance, as recorded using both LBIC and EQE measurements.

LBIC studies performed on devices grown on substrates having undergone an Ar^+ plasma cleaning process were also reported. These results showed that window layer growth defects were also present in these devices. Although the window layer defects observed in these devices were less detrimental to carrier collection at longer wavelengths when compared to devices grown onto conventionally cleaned substrates, where conversely, the effects of window layer defects were observed to lead to localised reductions in photoresponse at both 658 nm and 810 nm wavelengths

6.1.2 Scanning Kelvin probe microscopy (SKPM)

The SKPM technique was used to investigate Arsenic (As) p-type doping in CdTe PV solar cells. This provided the contact potential difference (CPD) between the As doped CdTe samples and the probe tip. The reported calibration of the tip provided a means of calculating the work function of the respective materials. Calibration of the tip was reported using a HOPG standard. An alternative reference material; Au was also presented, but the stability of the Au surface in ambient conditions was poor, where oleophilic effects and the formation of aurophilic complexes were proposed.

A series of CdTe samples with varying levels of As doping were characterised using SKPM. The topographic measurement revealed no observable differences between the samples. Conversely, the simultaneously recorded CPD images of the samples demonstrated a striking trend, where (as theoretical predictions indicated) increasing As concentrations in the CdTe led to a decrease in CPD, reflecting a downward shift in the CdTe Fermi level and an increase in CdTe work function. Calibrated work function values ranged from 3.88 to 4.09 eV for the CdTe, although comparably low with established CdTe work function values of between 5.5 and 5.9 eV, this focussed discussion on the difficulties in successfully recording absolute work function measurements in ambient conditions and did not detract from the clear relative trends described above.

Further high resolution studies using SKPM measurements on CdTe samples revealed interesting insights into the subtle variations in work function at grain boundaries (GB). It was shown that bulk As doping in CdTe thin films and the application of a p^+ highly doped back contact layer to the CdTe back surface led to localised shifts in the CPD at GBs when compared to an undoped CdTe sample. This indicated that the segregation of As at GB’s was leading to upward shifts in the VB and CB at these localised regions. It was proposed that this band bending reduced carrier recombination by channelling minority carriers away from the GB. This suggested that the GB network was actively contributing toward PV cell performance by enhancing carrier separation and reducing carrier recombination.

6.1.3 Conductive atomic force microscopy (CAFM)

The intricacies and challenges of CAFM measurements were presented and discussed. The phenomenon of 'current imprinting' was reported, where a hysteresis effect was observed to impact measurements depending on previous measurements carried out at the same location. It was proposed that this was caused by the formation of an oxide layer, or the modification of an existing oxide layer on the back surface of the CdTe. The filling of trap levels at high applied bias' was also suggested as an alternative explanation for this observation.

The effects of cell biasing were also identified where it was observed that CAFM measurements were only successful under relatively high forward bias conditions (+1 to +5V). This was attributed to the formation of a rectifying junction at the tip/CdTe surface interface, where a high bias was necessary to overcome this barrier. It was established that the forward biasing did not contribute to the formation of undesirable measurement artefacts, where biasing led only to an increase in 'image resolution' where the contrast of the observable features in each image was improved with increased forward bias.

High resolution CAFM measurements revealed interesting variations in GB and bulk grain conductivity. Subtle variations in inter-grain and intra-grain conductivity were indentified. A mechanism where the measurement of bulk grain and GB conductivity was very sensitive to the CdTe E_f was proposed. This showed that localised changes in the tip/surface barrier height were associated with the localised p-type dopant concentration of the CdTe and the E_f shift associated with this. This corresponded with observations made using the SKPM technique, where band bending at GBs was proposed to enhance carrier separation by channelling minority carriers away from the GBs.

6.2 Future Work

The application of the LBIC instrument for the investigation of photoresponse uniformity in photovoltaic solar cells is limited only by the choice of cell types available. Therefore, future work using this instrument could include the characterisation of an array of different cell types and configurations. This thesis has focussed on CdTe cells in superstrate configuration, future studies could include a variety of alternative thin film technologies, grown using a diverse array of deposition techniques (as briefly outlined in chapter 1). Further studies could also include dye-sensitized and organic solar cells. These may require specific illumination conditions which could be catered for by incorporating alternative lasers into the existing LBIC apparatus. For example, Si cells may require a longer wavelength IR laser to successfully yield high resolution LBIC measurements.

Further improvements to the LBIC instrument could include the incorporation of a software-controlled motorized z-axis translation stage, an addition which would reduce interruption to the apparatus during the setup stages of each experiment. This may also yield improved control over the laser beam focal point determination, leading to improvements in overall measurement resolution. The x – y translation stage used in these studies was limited to a range of 25 × 25 mm^2, a larger stage would provide the option to cover a larger scan area at lower resolution which could be of interest in the study of contacting architectures and optimizing cell geometries.

Further studies on MOCVD grown CdTe solar cells could include the investigation of $CdCl_2$ and anneal treatments on lateral carrier collection characteristics. The LBIC instrument could provide interesting insights into exotic and novel back contacting technologies including screen-printed carbon, silver and copper pastes where lateral variations in layer thickness and compositional uniformity could lead to significant lateral variations in carrier collection uniformity. The study of LDS layers incorporated into CdTe solar cells could also be expanded. This could include the study of the effects LDS layer thickness and QD concentration has on the isotropic emission characteristics of the QD's and their impact on the high energy EQE region of the $Cd_{1-x}Zn_xS$/CdTe spectral response.

Future studies using the SPM derivatives; SKPM and CAFM to examine CdTe thin films and devices could include a variety of novel investigations. The effect of front side illumination during CAFM measurement could be examined; although this was attempted using an *in situ* white light LED no discernible change was observed in CAFM mode (this was attributed to the photon flux being too low and the spectral mismatch between the LED emission and the CdTe spectral response). Alternative high flux illumination sources, such as a laser spectrally matched to the CdTe device' spectral response could provide very high resolution photoresponse characteristics in bulk grains and at grain boundaries.

The issues faced when performing SKPM measurements in ambient conditions to determine absolute work function values have been discussed. It may be possible to overcome these issues by performing similar SKPM measurements on As-doped CdTe samples using a high vacuum SPM instrument. This would have a variety of advantages including the reduction of surface contaminants (after a suitably robust surface cleaning process) and the increased sensitivity of the cantilever to the electric field formed between the sample surface and the SPM tip, due to the minimization of thermal drifts and vibrations.

Further studies on MOCVD grown CdTe devices could also exploit the diverse array of other SPM based derivatives including scanning capacitance microscopy (SCM) which could reveal further information on localised doping profiles by detecting variations in the majority carrier concentration across the sample surface. Scanning spreading resistance microscopy (SSRM) could yield spatially resolved local resistance measurements on CdTe where measurements are calibrated to an internal reference standard. Finally, scanning thermal microscopy (SThM) could enable the mapping of 2-dimensional temperature variations across a sample; a useful diagnostic tool for device failure analysis and compositional homogeneity analysis.

7 References

[1] B. Hunt, Isard, P., Laxton, D., The Macroeconomic Effects of Higher Oil Prices, International Monetary Fund Working Paper, 2001.
[2] J. Leggett, Half Gone, Portobello Books Ltd, 2006.
[3] J.M. Pearce, Renewable Energy 33 (2008) 1101.
[4] J.A. Turner, Science 285 (1999) 687.
[5] J. Burgermeister, renewableenergyworld.com, 8th April 2008.
[6] E. Becquerel, Comptes Rendues 9 (1839) 561.
[7] W.G. Adams, Day, R.E., Proceedings of the Royal Society of London 25 (1876) 113.
[8] D.M. Chapin, Fuller, C.S., Pearson, G.L., Journal of Applied Physics 25 (1954) 676.
[9] J. Perlin, The Silicon Solar Cell turns 50, NREL, 2004.
[10] M.A. Green, Emery, K., Hishikawa, Y., Warta, W., Progress in Photovoltaics: Research and Applications 19 (2011) 84.
[11] T. Jenkins, Physics Education 40/5 (2004) 430.
[12] W. Shockley, Queisser, H.J., Journal of Applied Physics 32/3 (1961) 510.
[13] A. Bosio, Romeo, N., Podesta, A., Mazzamuto, S., Canevari, V., Crystal Research and Technology 40/10-11 (2005) 1048.
[14] M.A. Green, K. Emery, Y. Hishikawa, W. Warta, E.D. Dunlop, Progress in Photovoltaics: Research and Applications 20/1 (2011) 12.
[15] A.V. Shah, Schade, H., Vanecek, M., Meier, J., Vallat-Sauvain, E., Wyrsch, N., Kroll, U., Droz, C., Bailat, J., Progress in Photovoltaics: Research and Applications 12 (2004) 113.
[16] I. Gordon, Van Gestel, D., Carnel, L., Beaucarne, G., Poortmans, J., 22nd European Photovoltaic Solar Energy Conference (2007) 1890.
[17] D. Bonnet, Rabenhorst, H., 9th Photovoltaic Specialists Conference, 1972, p. 129.
[18] D. Bonnet, Thin Solid Films 361-362 (2000) 547.
[19] K.L. Chopra, Paulson, P.D., Dutta, V., Progress in Photovoltaics: Research and Applications 12 (2004) 69.
[20] A.I. Oliva, Castro-Rodriguez, R., Ceh, R., Bartola-Perez, P., Caballero-Briones, F., Sosa, V., Applied Surface Science 148 (1999) 42.
[21] Unknown, First Solar Sets World Record for CdTe Solar PV Efficiency, 2012.
[22] A. Morales-Acevedo, Solar Energy Materials & Solar Cells 90 (2006) 2213.
[23] B. O'Regan, Grätzel, M., Nature 353 (1991) 737.
[24] R.D. McConnell, Renewable and Sustainable Energy Reviews 6 (2002) 273.
[25] N.S. Sariciftci, Smilowitz, L., Heeger, A. J., Wudl, F., Science 258 (1992) 1474
[26] M. Yamaguchi, Solar Energy Materials & Solar Cells 75/261-269 (2003).
[27] A.J. Nozik, Physica E 14/1-2 (2002) 115.
[28] A. Luque, Marti, A. , Advanced Materials 22/2 (2009) 160.
[29] N.P. Harder, Green, M.A., Semiconductor Science and Technology 18 (2003) 270.
[30] E. Klampaftis, Ross, D., McIntosh, K. R., Richards, B. S., Solar Energy Materials & Solar Cells 93/8 (2009) 1182.
[31] IBM, (May 2008).
[32] SolarSystems, (2008).
[33] D.A. Jenny, Bube, R.H., Physical Review 96/5 (1954) 1190.
[34] B. Goldstein, Physical Review 109/2 (1958) 602.
[35] D.A. Cusano, Solid-State Electronics 6/3 (1963) 217.

[36] J.A. Aranovitch, Golmayo, D., Fahrenbruch, A.L., Bube, R.H., Journal of Applied Physics 51/8 (1980) 4260.

[37] K.W. Mitchell, Fahrenbruch, A.L., Bube, R.H., Journal of Applied Physics 48/10 (1977) 4365.

[38] W. Yuan-Sheng Tyan, N.Y. Patent 1978.

[39] C. Ferekides, Britt, J., Ma, Y., Killian, L, Photovoltaics Specialists Conference, 1993., Conference Record of the Twenty Third IEEE, 1993.

[40] X. Wu, Solar Energy 77 (2004) 803.

[41] G.P. Hernandez, Matthew, X., Enriquez, J.P., Matthews, N.R., Sebastian, P.J., Solar Energy Materials & Solar Cells 70/3 (2001) 269.

[42] C. Lepiller, Cowache, P., Guillesmoles, J.F., Gibson, N., Ozsan, E., Lincot, D., Thin Solid Films 361-362 (2000) 118.

[43] J. Britt, Ferekides, C., Applied Physics Letters 62/22 (1993) 2851.

[44] J. Zhou, Wu, X., Teeter, G., To, B., Yan, Y., Dhere, R.G., Gessert, T.A., Physica Status Solidi (B) 241/3 (2004) 775.

[45] Z. Zhou, Zhao, K., Huang, F., Materials Research Bulletin 45 (2010) 1537.

[46] Y. Yan, Albin, D.S., Al-Jassim, M.M., NCPV Program Review Meeting, Lakewood, Colorado, 2001.

[47] M.A. Hernandez-Fenollosa, Halliday, D.P., Durose, K., Campo, M.D., Beier, J., Thin Solid Films 431-432 (2003) 176.

[48] J.D. Major, Durose, K., Thin Solid Films 517 (2008) 2419.

[49] S.J.C. Irvine, Barrioz, V., Lamb, D., Jones, E.W., Rowlands-Jones, R.L., Journal of Crystal Growth 310/23 (2008) 5198

[50] A. Gupta, Parikh, V., Compaan, A.D., Solar Energy Materials & Solar Cells 90 (2006) 2263.

[51] A.D. Compaan, Gupta, A., Lee, S., Wang, S., Drayton, J., Solar Energy 77 (2004) 815.

[52] A. Gupta, Compaan, A.D, Applied Physics Letters 85/4 (2004) 684.

[53] R.E. Treharne, Seymour-Pierce, A., Durose, K., Hutchings, K., Roncallo, S., Lane, D., Condensed Matter and Materials Physics Conference, vol. 286, Journal of Physics: Conference Series 2011, p. 012038.

[54] A.N. Tiwari, Romeo, A., Baetzner, D., Zogg, H., Progress in Photovoltaics: Research and Applications 9 (2001) 211.

[55] X. Matthew, Thompson, G.W., Singh, V.P., McClure, J.C., Velumani, S., Mathews, N.R., Sebastian, P.J., Solar Energy Materials & Solar Cells 76 (2003) 293.

[56] J.P. Enriquez, Mathew.X., Hernandez, G.P., Pal, U., Magana, C., Acosta, D.R., Guardian, R., Toledo, J.A., Puente, G.C., Carvaya, J.A.C., Solar Energy Materials & Solar Cells 82 (2004) 307.

[57] X. Matthew, Enriquez, J.P., Romeo, A., Tiwari, A.N., Solar Energy 77 (2004) 831.

[58] S. Smith, Zhang, P., Gessert, T., Mascarenhas, A., Applied Physics Letters 85/17 (2004) 3854.

[59] I. Visoly-Fisher, Cohen, S.R., Ruzin, A., Cahen, D., Advanced Materials 16/11 (2004) 879.

[60] J. Fritsche, Schulmeyer, T., Thißen, A., Klein, A., Jaegermann, W., Thin Solid Films 431-432 (2003) 267.

[61] K.V. Krishna, Dutta, V., Thin Solid Films 450 (2004) 255.

[62] V. Barrioz, Irvine, S.J.C., Jones, E.W., Rowlands, R.L., Lamb, D.A., Thin Solid Films 515 (2007) 5808.

[63] R.B. Bergmann, Applied Physics A: Materials Science and Processing 69/2 (1999) 187.

[64] M.A. Green, Emery, K., Hishikawa, Y., Warta, W., Progress in Photovoltaics: Research and Applications 16 (2008) 635.

[65] D. Azulay, Millo, O., Balberg, I., Schock, H-W., Visoly-Fisher, I., Cahen, D., Solar Energy Materials & Solar Cells 91 (2007) 85.

[66] I. Visoly-Fisher, Cohen, S.R., Gartsman, K., Ruzin, A., Cahen, D., Advanced Functional Materials 16 (2006) 649.

[67] L.M. Woods, Levi, D.H., Kaydanov, V., Robinson, G.Y., Ahrenkiel, R.K., NCPV Photovoltaics Program Review (1999).

[68] P.V.A. Meyers, S.P., Progress in Photovoltaics: Research and Applications 8/1 (2000) 161.

[69] V. Barrioz, Proskuryakov, Y.Y., Jones, E.W., Major, J., Irvine, S.J.C., Durose, K., Lamb, D.A., Mat. Res.Soc Symp. Proc 1012 (2007) Y12.

[70] J. Sarland, Ritala, M., Leskela, M., Siponmaa, E., Zilliacus, R., Solar Energy Materials & Solar Cells 44/177-190 (1996).

[71] I.M. Kotina, Tuknkonen, L.M., Patsekina, G.V., Shchukarev, A.V., Gusinskii, G.M., Semiconductor Science and Technology 13 (1998) 890.

[72] T.A. Gessert, Sheldon, P., Li, X., Dunlavy, D., Niles, D., Sasala, R., Albright, S., Zadler, B., 26th IEEE Photovoltaic Specialists Conference, Anaheim, California, 1997.

[73] A.E. Abken, Solar Energy Materials & Solar Cells 73/4 (2002) 391.

[74] B. Ghosh, Miles, R.W., Carter, M.J., Electronics Letters 32/10 (1996) 932.

[75] F.S. Goucher, Pearson, G.L., Sparks, M., Teal, G.K., Shockley, W., Physical Review 81 (1951).

[76] C.V. Hari Rao, Bates, H.E., Ravi, K.V., Journal of Applied Physics 47 (1976) 2614.

[77] T. Fuyuki, Matsunami, H., Tanaka, T., Journal of Physics D: Applied Physics 13/6 (1980) 1093.

[78] J.D. Zook, Applied Physics Letters 42 (1983) 602.

[79] J. Marek, Journal of Applied Physics 55 (1983) 318.

[80] C. Donolato, Journal of Applied Physics 54/3 (1982) 1314.

[81] D. Redfield, Applied Physics Letters 40/2 (1981) 163.

[82] R.T. Young, Lu, M.C., Westbrook, R.D., Jellision, Jr. G.E., Applied Physics Letters 38/8 (1981) 628.

[83] W.D. Sawyer, Journal of Applied Physics 59 (1986) 2361.

[84] C.H. Seager, Journal of Applied Physics 53/8 (1982) 5968.

[85] M. De Vittorio, Cingolani, R., Review of Scientific Instruments 70/8 (1999) 3429.

[86] E.P. Visser, Giling, L.J., Review of Scientific Instruments 61/5 (1990) 1490.

[87] M. Alietti, Berluti, L., Canali, C., Castaldini, A., Cavallini, A., Cetronio, A., D'Auria, S., del Papa, C., Lanzieri, C., Nava, F., Proia, M., Rinaldi, P., Zichichi, A., Nuclear Instruments and Methods in Physics Research A 355 (1995) 420.

[88] N.M. Shmidt, Soltenovich, O.A., Usikov, A.S., Yakimov, E.B., Zavarin, E.E, Journal of Physics: Condensed Matter 14 (2002) 13285.

[89] G. Brown, Faifer, V., Pudov, A., Anikeev, S., Bykov, E., Contreras, M., Wu, J., Applied Physics Letters 96/2 (2010) 022104.

[90] S.A. Galloway, Brinkman, A.W., Durose, K., Wilshaw, P.R., Holland, A.J., Applied Physics Letters 68/26 (1996) 3725.

[91] S.A. Galloway, Edwards, P.R., Durose, K., Solar Energy Materials & Solar Cells 57/1 (1999) 61.

[92] P.R. Edwards, Galloway, S.A., Durose, K., Thin Solid Films 361-362 (2000) 364.

[93] N. Baier, Brambilla, A., Feuillet, G., Lohstroh, A., Renet, S., Sellin, P., Nuclear Instruments and Methods in Physics Research A 576 (2007) 5.

[94] S. Smith, Dhere, R., Gessert, T., Stradins, P., Wang, T., Mascarenhas, A. , DOE Solar Cell Technologies, Denver, Colorado, 2005.

[95] A.A. McDaniel, Hsu, J.W.P., Applied Physics Letters 70/26 (1997) 3555.

[96] J.F. Hiltner, Sites, J.R., 16th European Photovoltaic Solar Energy Conference, Glasgow, 2000.

[97] J.F. Hiltner, Investigation of Spatial Variations in Collection Efficiency of Solar Cells, Colorado State University, 2001.

[98] J.R. Sites, Nagle, T.J., 31st IEEE PVSC, 2005, p. 199.

[99] M. Nonnenmacher, O'Boyle, M.P., Wickramasinghe, H.K. , Applied Physics Letters 58/25 (1991) 2921.

[100] B. Bhushan, Goldade, A.V. , Applied Surface Science 157 (2000) 373.

[101] A. Breymesser, Schlosser, V., Piero, D., Voz, C., Bertomeu, J., Andreu, J., Summhammer J. , Solar Energy Materials & Solar Cells 66 (2001) 171.

[102] S. Sadewasser, Glatzel, Th., Rusu, M., Jager-Waldau, A., Lux-Steiner, M. Ch. , Applied Physics Letters 80/16 (2002) 2979.

[103] I. Visoly-Fisher, Cohen, S.R., Cahen, D., Applied Physics Letters 83/24 (2003) 4924.

[104] S. Chevtchenko, Ni, X., Fan. Q., Baski, A.A., Morkoc, H. , Applied Physics Letters 88/12 (2006).

[105] B.S. Simpkins, Schaadt, D.M., Yu, E.T. , Journal of Applied Physics 91/12 (2002) 9924.

[106] B.S. Simpkins, Yu, E.T. , Journal of Applied Physics 94/3 (2003) 1448.

[107] S.A. Chevtchenko, Moore, J.C., Ozgur, U., Gu, X., Baski, A.A., Morkoc, H., Applied Physics Letters 89/18 (2006) 2111.

[108] C.-S. Jiang, Moutinho, H.R., Romero, M.J., Al-Jassim, M.M., Xu, Y.Q., Wang, Q., Thin Solid Films 472 (2005) 203.

[109] S. Sadewasser, Glatzel, Th., Schuler, S., Nishiwaki, S., Kaigawa, R., Lux-Steiner, M.Ch., Thin Solid Films 431-432 (2003) 257.

[110] C.-S. Jiang, Noufi, R., Ramanathan, K., AbuShama, J.A., Moutinho, H.R., Al-Jassim, M.M. , DOE Solar Energy Technologies, Denver, Colorado, 2004.

[111] B.E. McCandless, Rykov, S., Photovoltaic Specialists Conference, 2008. PVSC '08. 33rd IEEE, 2008, p. 1.

[112] I. Visoly-Fisher, Cohen, S.R., Cahen, D., Applied Physics Letters 82/4 (2003) 556.

[113] H.R. Moutinho, Dhere, R.G., Jiang, C-S., Al-Jassim, M.M., Materials Research Society Spring Meeting San Franciscom California, 2011.

[114] A. Dominget, Farkas, J., Szunerits, S. , Applied Surface Science 252 (2006) 7760.

[115] M. Troyon, Smaali, K., Nanotechnology 19 (2008) 255709.

[116] T. Mates, Bronsveld, P.C.P., Fejfar, A., Rezek, B., Kocka, J., Rath, J.K., Schropp, R.E.I Journal of Non-Crystalline Solids 352 (2006) 1011.

[117] D.C. Coffey, Reid, O.G., Rodovsky, D.B., Bartholomew, G.P., Ginger, D.S., Nano Letters 7/3 (2007) 738.

[118] L.S.C. Pingree, Reid, O.G., Ginger, D.S., Advanced Materials 21 (2009) 19.

[119] A. Alexeev, Loos, J., Organic Electronics 9/1 (2008) 149.

[120] H.R. Moutinho, Dhere, R.G., Jiang, C.-S, Gessert, T., Duda, A., Young, M., Metzger, W.K., Li, X., Al-Jassim, M.M., 2006 IEEE 4th World Conference on Photovoltiac Energy Conversion Waikoloa, Hawaii, 2006.

[121] H.R. Moutinho, Dhere, R.G., Jiang, C.-S., Al-Jassim, M.M., Kazmerski, L.L., Thin Solid Films 514 (2006) 150.

[122] H.R. Moutinho, Dhere, R.G., Jiang, C.-S., Gessert, T., Duda, A., Young, M., Metzger, W.K., Al-Jassim, M.M. , Journal of Vacuum Science and Technology B25/2 (2007) 361.

[123] T.L. Chu, Chu, S.S., Ferekides, C., Britt, J., Wu, C.Q., Journal of Applied Physics 71/8 (1992) 3870.

[124] R.A. Berrigan, Maung, N., Irvine, S.J.C., Cole-Hamilton, D.J., Ellis, D., Journal of Crystal Growth 195 (1998) 718.

[125] S.J.C. Irvine, Hartley, A., Stafford, A., Journal of Crystal Growth 221 (2000) 117.

[126] A. Hartley, Irvine, S.C.J., Halliday, D.P., Potter, M.D.G., Thin Solid Films 387 (2001) 89.

[127] R.L. Rowlands, Irvine, S.J.C., Barrioz, V., Jones. E.W., Lamb, D.A., Semiconductor Science and Technology 23 (2008) 015017.

[128] R.L. Rowlands, Barrioz, V., Jones. E.W., Irvine, S.J.C., Lamb, D.A., Journal of materials science: materials in electronics 19/7 (2008) 639.

[129] S.J.C. Irvine, Lamb, D.A., Barrioz, V., Clayton, A.J., Brooks, W.S.M., Rugen-Hankey, S., Kartopu, G., Thin film Solids 520/4 (2011) 1167.

[130] S.J.C. Irvine, Barrioz, V., Stafford, A., Durose, K., Thin film Solids 480-481 (2004) 76.

[131] E.W. Jones, Barrioz, V., Irvine, S.J.C., Lamb, D., Thin film Solids 517/7 (2009) 2226.

[132] R.L. Rowlands-Jones., School of Chemistry, University of Wales, Bangor, Bangor 2008.

[133] E.D. Palik, Handbook of Optical Constants of Solids, 1985.

[134] C. Ballif, Moutinho, H.R., Hasoon, F.S., Dhere, R.G., Al-Jassim, M.M., Ultramicroscopy 85 (2000) 61.

[135] W.S.M. Brooks, Irvine, S. J. C., Barrioz, V., Solar Energy Materials & Solar Cells 101 (2012) 26.

[136] W.S.M. Brooks, Irvine, S. J. C., Barrioz, V., Energy Procedia 10 (2011) 232.

[137] G.T. Koishiyev, Sites, J.R., Mat. Res.Soc Symp. Proc 1165 (2009) M05.

[138] G.T. Koishiyev, Sites, J.R., Solar Energy Materials & Solar Cells 93/3 (2009) 350.

[139] C.S. Ferekides, Mamazza, R., Balasubramanian, U., Morel, D.L., Thin Solid Films 480-481 (2005) 224.

[140] S.D. Hodgson, Brooks, W.S.M., Clayton, A.J., Kartopu, G., Barrioz, V., Irvine, S.J.C., Nano Energy submitted (2012).

[141] J.S. Kim, Lagel, B., Moons, E., Johansson, N., Baikie, I.D., Salaneck, W.R., Friend, R.H., Cacialli, F., Synthetic Metals 111-112 (2000) 311.

[142] W.N. Hansen, Hansen, G.J., Surface Science 481/1-3 (2001) 172.

[143] W. Melitz, Shen, J., Lee., S., Sung Lee, J., Kummel, A.C., Droopad,R., Yu, E.T., Journal of Applied Physics 108/023711 (2010).

[144] A. Alnajjar, S.A. Jawad, N. Yusuf, Renewable Energy 27/3 (2002) 417.

8 Appendices

8.1 Publications

8.1.1 Laser Beam Induced Current Measurements on $Cd_{1-x}Zn_xS$/CdTe Solar Cells

8.1.2 High resolution Laser Beam Induced Current Measurements on $Cd_{1-x}Zn_xS$/CdTe Solar Cells